Geophysical Observations of Nonlinear Internal Solitary-like Waves in the Strait of Georgia

by

Caixia Wang

B.Sc., The Ocean University of China, 1993
M.Sc., The Ocean University of China, 1996
M.Sc., The Joint Program of Massachusetts Institute of Technology and Woods Hole Oceanographic Institution, 1999

A THESIS SUBMITTED IN PARTIAL FULFILLMENT OF
THE REQUIREMENTS FOR THE DEGREE OF

Doctor of Philosophy

in

The Faculty of Graduate Studies

(Oceanography)

The University Of British Columbia

(Vancouver)

December 2009

Abstract

A novel observational method for studying internal features in the coastal ocean is developed and tested in a study of large nonlinear internal solitary-like waves. Observations were carried out in the southern Strait of Georgia in the summers of 2001 and 2002. By quantitatively combining photogrammetrically rectified oblique photo images from a circling aircraft with water column data we track a number of internal wave packets for periods of up to one hour and obtain a more complete view of internal waves, including propagation, oblique interaction, and generation. First, the applicability of various weakly nonlinear theories in modeling propagation of these large waves is tested. Both two-layer and continuous linear, KdV (Korteweg-de Vries), and BO (Benjamin-Ono) models are applied with and without background shear currents. After background shear currents are included, it is found that a continuously stratified BO equation can be used to model propagation speeds within observational error, and that this is not true for other theories. Second, four observed oblique wave-wave interactions including two Mach interactions, one interaction which varied from known interaction patterns, and one very shallow angle regular interaction are analyzed. An existing small-amplitude theory is applied but is found to overestimate the likelihood of Mach interaction at large amplitude. Finally, large-scale aerial surveys are mapped. Using speeds typical of observed waves, their time and place of origin are predicted. It is found that the observed waves are generated at the passes to the south of the Strait of Georgia and are released into the Strait after ebb tides.

Contents

List of Tables

List of Figures

Glossary

Symbols

- t: time
- k: wave number
- D: water depth
- N: buoyancy frequency
- h_1: upper layer depth
- h_2: lower layer depth
- h_{eff}: effective layer depth
- ρ: density
- ρ_1: mean density in the upper layer
- ρ_2: mean density in the lower layer
- $\Delta\rho$: the density difference ρ_2-ρ_1
- U: background current
- U_1: mean background current in the upper layer

- U_2: mean background current in the lower layer
- ΔU: the shear strength U_1-U_2
- u_1: horizontal velocities induced by soliton in the upper layer
- u_2: horizontal velocities induced by soliton in the lower layer
- η: wave amplitude
- η_0: maximum wave amplitude
- η_m: maximal wave amplitude
- L: soliton half width
- λ: wave length/soliton scale length
- θ: wave phase
- ϕ: mode shape
- c_0: linear phase speed
- c: wave phase speed
- c_{obs}: observed wave phase speed
- c_{shear}: wave phase speed with shear effect included
- ψ: interaction angle
- η_1: wave amplitude of one interacting wave/incident wave
- η_2: wave amplitude of the second interacting wave/image of the incident wave
- η_i': nondimensionalized wave amplitude of an interacting wave (i=1, 2)

- ψ_i: incident angle
- ψ_r: reflection angle
- ψ_c: critical angle
- η_i: wave amplitude of the incident wave
- η_r: wave amplitude of the reflected wave
- $\overrightarrow{v}_{tide}$: tidal currents

Abbreviations

- ADCP Acoustic Doppler Current Profiler
- CTD Conductivity-Temperature-Depth Probe
- CCD Charge Coupled Device
- T-chain thermistor string
- KdV Korteweg-de Vries
- eKdV extended Korteweg-de Vries
- ILW Intermediate Long Wave
- BO Benjamin-Ono
- GPS Global Positioning System
- PDT Pacific Daylight Time

Acknowledgments

I thank Rich Pawlowicz for always being a supportive and considerate supervisor. I also gratefully acknowledge my thesis committee members including Rich Pawlowicz, Susan Allen, Greg Lawrence, and William Hsieh for continuous scientific support.

Chapter 1

Introduction

1.1 Definition and Importance of Internal Solitary Waves

In oceans and lakes, water is separated from air by a free surface and the undulations of this free surface are the most commonly known waves, i.e. the surface waves. However, this is not the only type of water wave. Within the water column differences in temperature and salinity can give rise to situations in which lighter water lies above heavier. At such interfaces waves can also occur, and these are called internal waves. As density differences between such internal layers are much smaller than between air and water the gravitational restoring force is much weaker. These internal waves can easily have dimensions greatly exceeding those of surface waves, while their time evolution and propagation is much slower.

Internal waves are a widespread geophysical phenomena. They exist in coastal seas, straits, fjords, continental shelves, lakes, and the atmospheric boundary layer. Their existence does not necessarily require strong sharp stratification. They can be found in any kind of continuous density stratification, especially near abrupt topographic features such as strait sills, continental slopes or sand banks (e.g., Apel et al., 1995).

Internal waves are important in oceanographic, acoustic, optical, geological, and biological disciplines. Long nonlinear internal waves generated by the interaction of barotropic tidal flow with bathymetry are thought to exert a significant contribution to the dissipation

of the rotational energy of the earth-moon system and to the mixing of different water masses in the ocean (Apel et al. 1995; Munk and Wunsch 1998). One of the many examples of their biological impact is the evidence that internal tidal bores can transport larvae (Pineda, 1991; Leichter et al., 1998). Another example is that the enhanced mixing associated with internal wave packets has been postulated (Sandstrom et al., 1989) as a mechanism for enhanced nutrient supply and coincident higher biological productivity on continental shelves. The impact of internal waves on ocean-acoustic signal transmission also received attention from oceanographers and ocean acousticians (King et al. 1994; the SWARM Group 1997). The existence of natural variations in the acoustic characteristics of the ocean, associated with the presence of internal waves, clearly complicates submarine detection. Though not as destructive as "tsunamis", the larger oceanic internal waves carry a considerable amount of energy and the associated current flows can be strong enough to be an important factor in the design of coastal oil platforms and similar sea structures. Internal waves are often observed to be of a large enough amplitude that nonlinear dynamics are important in their evaluation.

Solitary waves are a particular class of waves. The definition of solitary wave or soliton should be clarified, although it is not easy to give a comprehensive and precise definition. Drazin and Johnson (1988) associated the term of soliton with any solution of a nonlinear equation (or system) which represents a wave of permanent form. It is localized (i.e. decays at infinity), and can interact strongly with other solitons and retain its identity. It is this particle-like behavior that characterizes these solitary waves as solitons. A more recent definition of solitary wave was given by Grimshaw (2002) : "solitary waves are finite-amplitude waves of permanent form which owe their existence to a balance between nonlinear wave-steepening processes and linear wave dispersion. Typically, they consist of

Figure 1.1: An image of internal wave slicks near Active Pass looking south on June 26, 2002. The hovercraft "SIYAY" providing water column data is the red object at center right.

a single isolated wave, whose speed is an increasing function of the amplitude." The name solitary wave is more general. Internal solitary waves or solitons are those solitary waves or solitons which could appear on isopycnals below the water's surface.

In geophysical situations packets of internal waves are often observed (Figure 1.1). The distances between individual waves are often much greater than the length scale of the waves, which have a shape similar to true solitary waves. Within the packet the shape and characteristics of the waves change only very slowly and these waves are often rank ordered, with largest waves near the front. Although these are unlikely to represent truly permanent

forms they may be similar to solitons and are correctly classified as "solitary-like" waves. The mathematical theory of solitons may then be useful as a guide to their behavior.

The wave amplitude is an important measurement of the size of an internal wave. The amplitude of an internal wave is defined as the maximum displacement from the undisturbed interface (Helfrich and Melville, 2006). Several terms in this thesis related to wave amplitude are now defined. "Small-amplitude" (and finite) internal waves are waves with amplitudes small compared to the depth of the thinner layer either above or below the interface in two-layer systems. Internal solitary waves with small-amplitude are weakly nonlinear, and their mathematical theory is based on asymptotic expansions involving amplitude divided by layer depth (the layer where waves reside). In the Strait of Georgia, the observed internal waves have amplitudes comparable to the thinner upper layer and these waves are called "large-amplitude" waves, i.e. with "strong nonlinearity". Strictly speaking their behavior is beyond the applicability of weakly nonlinear theories but in general no analytic theory is available. This thesis will show how well small-amplitude theories can work in this situation.

1.2 Theory and Observations

A great deal of research has been carried out on internal waves, far more than can be comprehensively summarized here. Numerical, analytical, and laboratory studies of small-amplitude wave propagation are largely in agreement. However, precise comparisons with geophysical phenomena, which are often not strictly in compliance with the limitations of small-amplitude theory, are limited due to observational difficulties. The lack of observations has also limited progress in certain aspects of their behavior (such as oblique interactions). In this thesis an observational technique is developed and used to address

some of these open questions. Results relevant to this thesis are now briefly described.

1.2.1 Internal Solitary Wave Models

One of the most frequently used models of small-amplitude wave propagation is the Korteweg-de Vries (KdV) equation. It is well-established that nonlinear evolution equations of the KdV type form at least a first-order basis for qualitative modeling and prediction (Grimshaw, 1997). Internal solitons in a layered medium have been described by the KdV equation (see, e.g., Benney 1966) since 1876, but the KdV equation applies only to the shallow water ($kD \ll 1$), weakly nonlinear (small but finite amplitude, $\eta_0/D \ll 1$), and weak dispersion ($(D/\lambda)^2 \ll 1$) cases with nonlinearity balancing dispersion. Here η_0 is a measure of the wave amplitude, D is a measure of water column depth, λ is a measure of the wave length in the direction of wave propagation, and $k = 2\pi/\lambda$. If λ is only long compared to the water depth below or above the interface, but not to the whole water depth ($kD > 1$), implying that one of the layers is much thinner than the other, then the waves are called "deep-water" waves. For a deep-water wave, small amplitude (weakly nonlinear) internal waves are described by the Benjamin-Ono (BO) equation (Benjamin 1966; Ono 1975) for which soliton solutions can be found. The weakly nonlinear intermediate-depth case is described by the Intermediate Long Wave equation (ILW) which has been investigated by Joseph (1977) and Kubota et al. (1978). The ILW model equation solitons are a family of solutions of one parameter and can reduce to KdV or BO solutions in the appropriate limit. The detailed KdV, ILW, and BO equations for layered flows as well as their extension to continuous stratification can be found in Chapter 3 of this thesis.

Unfortunately, the weak nonlinearity (small-amplitude) assumption presumed by KdV, BO, and ILW models does not always seem adequate for the experimental and observa-

tional data that has been collected by researchers. The small-amplitude limitation of the above classical models led to the development of different extended models such as eKdV containing higher-order nonlinearities for either two-layer or continuously stratified models (Benney and Ko 1978; Miles 1979, 1981; Koop and Butler 1981; Grimshaw et al. 1997; Ostrovsky and Stepanyants 2005). The "eKdV" is the short form for extended Korteweg-de Vries equation and is also known as Gardner equation (Ostrovsky and Stepanyants 2005). The eKdV equation has both quadratic and cubic nonlinearities. The detailed eKdV equations for layered flows can be found in Chapter 3 of this thesis. An alternative to small-amplitude theories has been numerical solutions of either the fully nonlinear fluid equations or approximations thereof (e.g. Long 1953; Davis and Acrivos 1967; Green and Naghdi 1977; Lamb and Yan 1996; Choi and Camassa 1999; Vlasenko et al. 2000). The fully nonlinear models are usually restricted to steady state, otherwise, the calculation of time-dependent solutions can be computationally expensive (Helfrich and Melville, 2006). However, among all the models or equations, the KdV model seems to have the widest application in successful prediction of experimental or observational solitons, even for large amplitude solitary-like waves which are outside of the strict assumption of the KdV theory, while BO or ILW theory appears not to do so (Grue et al. 1999; Koop and Butler 1981; Michallet and Barthelemy 1998; Segur and Hammack 1982; Small et al. 1999). "The question of why this solution is suitable for waves of such large amplitude remains open" (Small et al., 1999). Some laboratory results (Ostrovsky and Stepanyants 2005; Koop and Butler 1981; Segur and Hammack 1982) suggest that the KdV model matches observations better in deep water than the BO theory which was specifically designed for such cases. A copy of a figure from Koop and Butler (1981) as in the review by Ostrovsky and Stepanyants (2005) is included here for reference (Figure 1.2). The figure shows a better match in a

laboratory situation for wavelengths in deep-water with KdV models. Some observational research has also shown that the KdV equation is quite reasonable in deep water (e.g., Osborne and Burch, 1980), but a definitive comparison has not yet been carried out. During a measurement program in the Andaman Sea, Osborne and Burch (1980) observed water waves ($2\pi D/L \approx \pi$) by making water column measurements including wave amplitudes (obtained from temperature contours) and particle velocities and then compared with KdV theory and found that the observations are predicted by the KdV equation. They did not measure wave speeds or wave propagation directions.

1.2.2 Internal Solitary Waves in Background Shear

Shear is often ignored in studies of nonlinear waves. However, Holloway et al. (1997) used a generalized KdV equation to investigate the effect of shear and obtained numerical solutions. They found that for the cases they considered, the phase speed could be affected by shear by as much as 15% to 30%. Grimshaw (1998) and Tung et al. (1981) also studied the effect of shear on nonlinear internal waves and pointed out that a horizontal background shear modified the wave parameters including wave phase speed and wave half width. Stastna and Lamb (2002) studied the effect of background shear on large fully nonlinear internal solitary waves under continuous stratification and claimed that the presence of a background current could also affect the maximal wave amplitude by modifying the wave breaking onset condition. Choi (2006) considered a two-layer system with uniform shear and obtained an analytical solution of his strongly nonlinear model with a Boussinesq assumption. He found, when compared with the irrotational (no shear) case, that positive vorticity slowed down the propagation and increased the width of a wave of depression propagating in the positive x direction while it sped up the propagation and decreased the wave width if the depression

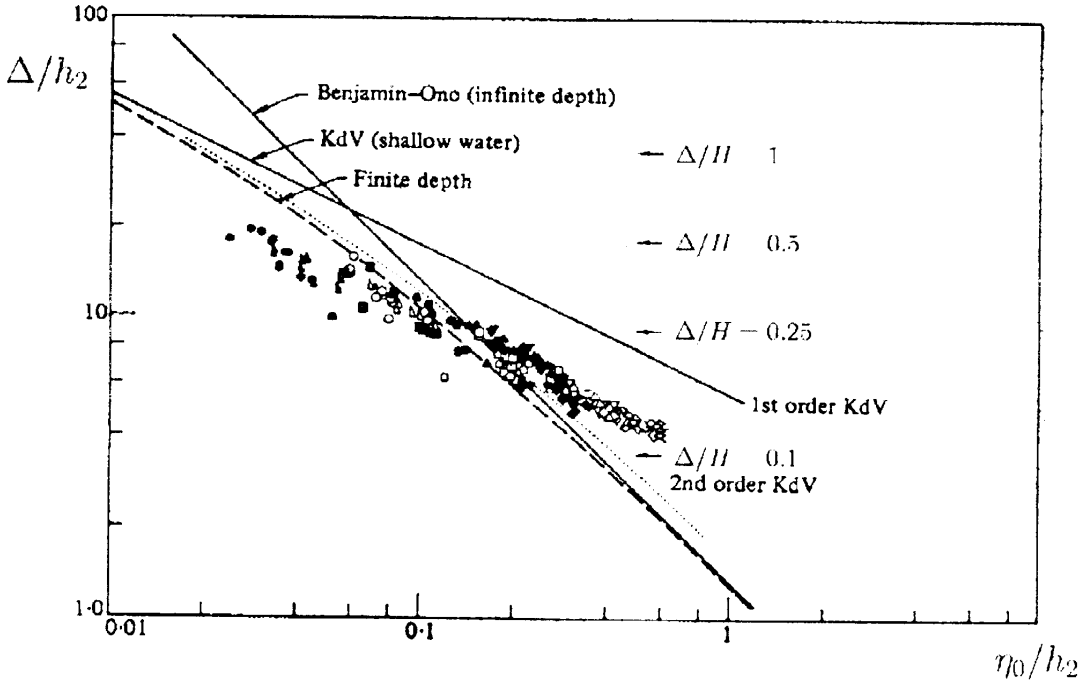

Figure 1.2: Dependence of normalized soliton characteristic wavelength Δ/h_2 on normalized amplitude η_0/h_2 as predicted by different theories (lines) and measured in deep-water laboratory experiments (discrete markers). The ratio of the upper and lower layer depth is $h_1/h_2 = 35$. The solid line denoted "first order" corresponds to the usual KdV equation; the dotted line denoted "second order" corresponds to the generalized KdV equation with second-order nonlinear and dispersive corrections; the dashed line denoted "finite depth" corresponds to the JKKD (Joseph-Kubota-Ko-Dobbs) equation; and another solid line denoted "infinite depth" corresponds to the BO equation. From Koop and Butler (1981).

was propagating in the negative x direction. The existing literature suggests that if there is discrepancy between observation and model prediction, an important factor which deserves attention is the effect of the background shear current. Unfortunately this is usually the least-well observed parameter in geophysical situations.

Extending weakly nonlinear theories to include shear effects can be done in a straightforward manner because if a wave of fixed amplitude satisfies the KdV (or other related) equations in the absence of shear, it will also do this in the presence of shear, with only the equation coefficients being modified (Grimshaw, 1998). Other papers that discuss the shear effect on continuously stratified internal waves include Tung et al. (1981) and Maslowe and Redekopp (1980).

1.2.3 Oblique Interactions of Internal Solitary Waves

The previous discussion has focused on propagation with one horizontal dimension almost universally assumed. However, geophysical situations often show waves propagating in different directions (in two horizontal dimensions) and interacting with each other. Such interactions are not well studied. A general work was that of Miles (1977 a, b) who investigated small-amplitude shallow-water interactions between KdV solitons. More recently such interactions are studied as a model for rogue waves (Soomere and Engelbretcht, 2006). Relevant parameters are then the amplitudes η_1 and η_2 of the two solitons, as well as the angle ψ between the two wave normals. When the wave amplitudes are similar then the interaction can be treated as a reflection problem (i.e. with the waves obliquely propagating into a wall). The parameter space admits a number of different behaviors in which the solitons can be shifted both forwards, both backwards, and one forward and one backward. In addition, there is a region of parameter space when ψ is less than a critical value

in which no steady solution exists. In this region, the interaction results in growth of a third wave, called the Mach stem (or Mach reflection in reflection situations). Mach reflection is so-called due to its geometrical similarity to shock-wave reflection in gas dynamics (Whitham, 1974). Not only does the Mach stem grow with time but the interaction changes the amplitude and propagation direction of the original waves. An overview of the practical application of certain properties of phase shifts, and the resulting high wave hump during Mach reflection and nonlinear interaction of solitons can be found in Soomere (2007).

After Miles' work, there followed laboratory and numerical investigations to test his theoretical results. Melville (1980) performed laboratory experiments. He supported Miles in predictions of critical angle, but the measured amplitude of the Mach stem at the wall is considerably lower than Miles. Funakoshi (1980, 1981) supported Miles with numerical results. He stated that the discrepancy between Miles and Melville in the amplitude of the Mach stem was due to the insufficient interaction time in Melville's measurements. Tanaka (1993) looked at large amplitude wave interactions numerically and compared with the analytic results of Miles. He concluded that Miles' results only apply to weakly nonlinear i.e. small amplitude wave cases with $\eta_{1,2}^{'} \ll 1$ (η_1' and η_2' are wave amplitudes nondimensionalized by water depth for surface waves). For large amplitude waves, the effect of the large amplitude tends to prevent Mach reflection from occurring. If Mach reflection does take place for large amplitude waves, it will differ from small amplitude cases. The interaction will be "contaminated" by regular reflection with the amplitude of the reflected wave close to that of the incident wave. Johnson (1982) analyzed oblique interaction between a large and a small wave using a perturbation method. When the incident angle was within a restricted range, Mach reflection occurs. When Mach reflection occurs, Johnson's results agree much better with Tanaka than Miles. Miles results are apparently useful if the wave

amplitudes are sufficiently small.

Although the above analysis was carried out for surface waves, the equations used were of the KdV type and hence the results should be applicable to shallow-water internal waves as well. One of the features of internal waves which distinguish them from surface waves is that there is an infinite set of modes and the interaction between different modes makes the interaction of internal waves more complicated than that of surface waves. However, according to Liu et al. (1998), almost all of the nonlinear internal waves observed in nature are Mode - 1 depression waves. It is plausible that the interaction of internal solitary waves of the same mode can be treated like the surface solitary waves interactions (Grimshaw and Zhu, 1994). The dependence of phase shift on the interaction angle and wave amplitudes is generally similar for both surface and internal waves, although slight differences have been found in numerical studies (Lynett and Liu, 1998).

Deep-water solitons have novel characteristics compared to those in shallow water systems. For example, the BO solitons have a profile expressed in terms of algebraic functions (Equation 3.27), while KdV solutions are expressed by hyperbolic functions. The differing functions suggest that the oblique interactions of shallow water waves and deep-water waves may differ fundamentally. However, according to Grimshaw and Zhu (1994), in either a shallow water (KdV) interaction or a deep water (ILW as in Grimshaw and Zhu, 1994) interaction, the only effect of interaction on the two interacting waves is a phase shift. For head-on collisions of two BO solitons, it was shown analytically by Matsuno (1998) that the amplitudes of solitary waves did not change after interaction while both of the two waves were shifted backwards in phase. Also, at an interaction angle of 120°, both interacting waves in shallow water and deep water systems do not experience any phase shift. Therefore, the interactions between deep-water solitary waves and between shallow water

solitary waves have some resemblance.

Oikawa (1984) studied the weak oblique interactions of two internal waves in a deep two-layer fluid system. His first order solution showed that the phase shifts of the solitary waves in an interaction were constant and were not affected by their wave amplitudes. Grimshaw and Zhu (1994) studied weak and strong interactions for both KdV and BO waves. For the similar deep water problem as Oikawa (1984), their first order solution reproduced Oikawa's results. Matsuno (1998) used a systematic perturbation method to investigate the oblique interaction of interfacial solitary waves in a system of finite lower layer depths and shallow, finite upper layer depth. He developed a second order analysis of weak oblique wave interactions in this deep water system. To first order, Matsuno confirmed Oikawa and Grimshaw & Zhu's results, but to the second order, the phase shifts depend on the amplitudes of the interacting waves in a complicated way.

Tsuji and Oikawa (2001) numerically studied the oblique interactions of internal solitary waves in a deep two-layer fluid. Their wave amplitudes (non-dimensionalized by the shallow layer depth) are as high as $\eta_i' = 2$. They found that Mach interaction did occur for small interaction angles ($\psi < 118°$). For interaction angles near $\psi = 106°$, maximum Mach stem amplitudes were generated. The critical angle is much smaller than that predicted using Miles' theory (at this large amplitude). The maximum Mach stem amplitude exceeds the values for predicted shallow-water waves.

Overall, most of research on wave-wave interactions is theoretical and has seldom been applied to, or validated by, geophysical observations. The closest I found is Small et al. (1998) on a web page which has not been published. Small et al. (1998) studied non-linear interactions of internal solitons observed in SAR imagery using a three-dimensional CFD (Computational Fluid Dynamics) code and compared to previous analytical results.

Oblique interaction of internal solitary waves is also observed in the Gulf of Carpentaria in northern Australia (the Morning Glory) (Christie and White, 1995), but these observations have not been analyzed yet.

1.2.4 Generation Mechanisms

Numerous researchers have studied internal wave generation mechanisms. Many references can be found in Helfrich and Melville (2006) and Baines (1995). One of the most studied mechanisms involves interaction of barotropic tidal flow and topography, such as continental shelves (eg. Hibiya, 2004), submarine mountains (eg. Artale et al., 1984; Baines 2007), or sills. The literature contains theoretical investigations (Rattray 1960; Cox and Sandstrom 1962; Rattray et al. 1969; Baines 1973, 1974, 1982; Prinsenberg et al. 1974; Prinsenberg and Rattray 1975; Stigebrandt 1980) and observations (Halpern 1971; Gargett 1976; Haury et al. 1979; Farmer and Smith 1980; Osborne and Burch 1980; Chereskin 1983; La Violette and Arnone 1988; Sandstrom and Elliott 1984; Farmer and Armi 1999; Cummins et al. 2003).

Several different mechanisms are at work even in topographic interactions. Internal waves appear to be produced at different stages of barotropic tides and at different locations (upstream, on top of, or downstream) relative to the topography. One of the early studies of internal wave generation is Lee and Beardsley (1974). They studied the upstream generation of long nonlinear internal waves from a front due to partial blocking of the stratified flow over Stellwagen Bank. They used an inhomogeneous model forced by barotropic tide over topography and compared with Halpern's (1971) measurements, finding that the generation of an internal wave packet includes three components: formation of a front upstream, steepening of the front, and finally a wave packet generated by the balance of nonlinearity

and dispersion. Hibiya (1986, 1990) suggested a continual generation mechanism over a sill. He analytically studied internal wave generation mechanisms through interaction between tide and a sill (Hibiya, 1986) and by a vertically sheared tidal flow over a sill (Hibiya, 1990). An internal wave which propagates upstream is gradually formed over the sill through the interference among infinitesimal amplitude internal waves emanated from the sill at each instant of time. Farmer and Smith (1980) discussed at least two kinds of internal wave generation mechanisms observed in the Knight Inlet, including the escape of lee waves over the sill and waves following the relaxation of an hydraulic jump.

Laboratory work was done by Maxworthy (1979) to study internal waves produced by tidal flow over a three-dimensional ridge. With the ebbing tidal flow flowing over an obstacle, a downstream depression was formed. When the tidal flow slackened and turned to flood, the depression propagated upstream over the topography and evolved into a train of internal waves. La Violette and Arnone (1988) presented measurements of internal waves in the Strait of Gibraltar, together with simultaneous visual observations from aircraft and the space shuttle and found that the internal waves were generated by the tidal flow over Camarinal Sill at the western end of the Strait. While the tidal flow over the sill is ebbing (westward), an internal lee wave or a hydraulic jump is formed on the downstream side of the sill. As the ebb tide relaxes and reverses to flood, the lee wave disturbance evolves into a train of nonlinear internal waves propagating into the Strait. Additional mechanisms involving release of waves originally formed above or slightly upstream of a sill crest were also suggested by Farmer and Armi (1999), Xing and Davies (2006), Davies and Xing (2006), Stashchuk and Vlasenko (2007), La Violette and Arnone (1988). In Farmer and Armi (1999), observations of tidal flow over a sill show that upstream solitary wave generation occurred in conjunction with the downstream movement of a streamline

bifurcation over the obstacle crest. Solitary waves appeared upstream of the bifurcation. Shear flow instabilities on the plunging interface were evident and may contribute to wave generation through subharmonic interaction. Nonlinear waves generated downstream of an internal control became trapped in the supercritical flow. Xing and Davies (2006) and Davies and Xing (2006) used a non-hydrostatic model in cross sectional form with idealized topography representing a sill, forced by a barotropic tidal flow. Calculations using smooth topography show that unsteady lee waves are generated on the sill slope during flood tide. These waves propagate towards the sill when the tide reverses. Stashchuk and Vlasenko (2007) reported on a series of numerical experiments of stratified tidal flow in Knight Inlet with a fully nonlinear nonhydrodynamic model. Accelerating tidal flux forms a baroclinic hydraulic jump just above the top of the sill whereas the bifurcation and zones of shear instabilities are formed downstream of the sill. The first baroclinic mode having the largest velocity escapes from the generating area and propagates upstream, disintegrating into a packet of solitary waves.

Cummins et al. (2003) studied generation and propagation of internal waves near a sill in Knight Inlet during ebb tide. Observations showed that stationary and strongly nonlinear internal waves were formed on a bore upstream of the sill and were not released until the ebbing tidal flow relaxed. Trains of internal solitary waves then propagated upstream of the sill.

All studies seem to show that waves can be generated even in the presence of substantial mixing and turbulence. Thus it is not unexpected that the complicated Boundary Pass region, south of our study location, in the Strait of Georgia can act as a generation area. Determining the location of the initial depression and phase of tides when waves leave their generation area might help to differentiate generation mechanisms.

1.2.5 Geophysical Observations

Internal waves have been observed in many different parts of the world. For example, Ziegenbein (1969) and Lacombe and Richez (1982) measured eastward propagating internal waves in the Strait of Gibraltar. La Violette and Arnone (1988) presented further measurements of internal waves in the Strait, together with simultaneous visual observations from aircraft and the space shuttle. Gargett (1976) studied internal waves observed in the Strait of Georgia, British Columbia. Farmer and Smith (1980) measured trains of large amplitude, nonlinear internal waves in Knight Inlet, a long and narrow fjord in British Columbia. Osborne and Burch (1980) recorded the observation of internal waves in the Andaman Sea, offshore of Thailand. Most of the previous observations used in situ methods including CTDs (Pinkel et al. 1991; Klymak and Gregg 2001; Klymak and Gregg 2004; Moum et al. 2003), thermistor strings (Marmorino 1987; van Haren 2005), ADCPs (Moum et al. 2003; Umlauf and Lemmin 2005; Dewey et al. 2005; Colosi et al. 2001; Klymak and Gregg 2001; Klymak and Gregg 2004), echo sounders (Farmer and Armi 1999; Cummins et al. 2003; Moum et al. 2003), Doppler sonars (Pinkel 1983), acoustic transceivers (Dushaw et al., 1995), and bathythermographs (Wijffels and Meyers, 2004).

The conventional methods used to measure internal wave properties are important but localized, and it can be difficult to track individual waves. However, internal waves have long been known to affect the roughness of water surface. Until the 1970s, the prevailing explanation for this phenomenon was that of Ewing (1950), who stressed the importance of a surface film due to organic matter, but failed to explain the equally important presence of co-propagating rough bands. More recently, it was recognized that the interaction between surface waves and a spatially varying current induced by the internal wave could account for the presence of both smooth and rough bands (Gargett and Hughes, 1972). The effect

is both a positive and negative one. Bands of surface waves in the vicinity of internal waves can appear both smoother (in slicks) and rougher than the ambient roughness. For instance, in an internal wave of depression in a water system where the upper layer is much thinner than the lower layer, the upper layer water at the leading edge of the wave is much rougher due to convergence and downwelling and the water surface will appear darker. On the other hand, at the trailing edge, the upper layer water is upwelling and diverging, and the water surface appears smoother and lighter. The leading edge and the trailing edge of an internal wave can be identified from photo images (Figure 2.6). In images like Figure 2.6, the wave-wave spacing is the distance between dark edges in the direction of wave propagation.

These banding features of the water surface can be captured by remote sensing equipment such as synthetic aperture radar, or as in this thesis, with a digital camera. Figure 1.1 is an oblique aerial photograph of the internal waves in the Strait of Georgia. Note the sequence of apparently rank-ordered slicks. Remote observations of internal wave surface features are now a common way to study long nonlinear internal waves. Satellite images of internal waves have been obtained routinely since the 1970s by photography and by Synthetic Aperture Radar (SAR) (Apel et al., 1975). For instance, Apel et al. (1975), Osborne and Burch (1980), and Liu et al. (1998) have observed internal solitary waves in the New York Bight, the Andaman Sea, the East and South China Seas from images gathered by SAR. Space-based remote sensing techniques provide wide area data but have the disadvantage that it is almost impossible to keep observing the same wave packet over time or to track the evolution of the same wave-wave interaction. Thus SAR imaging is less useful for research requiring small space and time scales. Oblique photo images have been used to study internal waves at these smaller scales. Shand (1953) observed internal

wave packets from photographs in the Strait of Georgia. Farmer and Armi (1999) took aerial photographs of internal waves in Knight Inlet. Pawlowicz (2003) observed internal wave packets in Haro Strait by taking oblique images of the water surface from a hill on the coast. Moum et al. (2003) studied the structure and generation of turbulence at interfaces strained by internal solitary waves and carried out observations of internal solitary waves propagating shoreward over Oregon's continental shelf. In their study, photographs of the surface signature of internal solitary waves were taken with X-band radar and digital camera. Cummins et al. (2003) studied upstream influence and generation of nonlinear internal waves in Knight Inlet by taking photo images of the sea surface from both a fixed mountainside location and a helicopter. Recently, some researchers (Holland et al. 1997; Pawlowicz 2003; Bourgault 2007) have developed a remote sensing method to obtain quantitative visualization of the sea surface using commercially available digital cameras. Digital images allow for the straightforward application of digital processing.

Finally, internal waves are also observed in the laboratory. Experiments on internal waves have been conducted by Kao et al. (1985) and Boegman et al. (2005). The experiments of Kao et al. (1985) were conducted on the pycnocline of a continuously stratified fluid and a KdV equation for the "interfacial" displacement was developed. Boegman et al. (2005) studied internal waves in a tank similar to a lake with sloping topography.

1.3 Thesis Objectives

Although ship and mooring-based observations can and have provided much detailed information about the structure of solitary-like waves their data sets are often unsatisfactory for making precise measurements of propagation speed because they can only sample a small part of the wave. It is not clear, for example, if repeated transects resample the same part

of a wavefront, or if they are shifted laterally and so we are actually observing along-crest changes. Quantitative photogrammetry has the potential of clarifying such observations. Shore-based quantitative photogrammetry has been used by Pawlowicz (2003) and Bourgault (2007) for internal waves, and by Holland et al. (1997) for surf-zone studies. Aerial photographs have been used in a qualitative way by, for example, Farmer and Armi (1999) and Cummins et al. (2003). In this thesis our first objective is to develop and test a quantitative technique for using aerial photographs. Although the techniques of photogrammetry are well established, adapting it to use on a rapidly moving platform introduces a number of difficulties. For example, if images are taken from an airplane, vertical motions and sharp turns cause the view point to change rapidly. Optical measurements are often quite sensitive to these variations. Shore-based photogrammetry such as in Pawlowicz (2003) has only a limited view and relies on topographical features that may not provide a view of the internal wave features of interest. This thesis research also expands the imaging technique by coordinating sampling from both an airplane and a surface vessel. This allows us to track individual waves and wave-wave interactions and measure the propagation of waves precisely. With this novel observation method, datasets of surface expressions and water column characteristics of internal waves are obtained, and unique observations of wave-wave interactions are obtained. Although wave-wave interactions are often observed by remote sensing techniques such as SAR images in South China Sea, Gibraltar, and Andamn Sea, the data thus obtained often lack this extra information needed for detailed studies.

In the study of nonlinear internal waves, people often use their field or lab observations to compare with classic small amplitude theories which include KdV and BO equations. The KdV model has been claimed to have wider range of application than its assumptions of shallow water and weak nonlinearity suggest (section 1.2.1) and has been found to match

observations of strongly nonlinear and deep water cases, while the BO equation has not found application in real fluids. In addition, KdV and BO models have very strict assumptions which are very often unsatisfied by actual ocean waves. The second objective is then to determine whether classic models can be extended to describe observed waves in the Strait of Georgia.

In the course of field work a number of observations were made in which internal wave packets were colliding at oblique angles. As discussed in section 1.4, the prevailing available theory of wave-wave interaction is Miles' (1977 a, b) shallow water weakly nonlinear theory. The numerical work of Tanaka (1993) showed that Miles' (1977 a, b) theory is quantitatively wrong for large amplitude waves. The third objective of this thesis is then to study our observed wave-wave interactions using Miles' theory and to determine whether this theory can be extended outside of its weakly nonlinear limitations. As already stated, wave-wave interaction studies have mostly been numerical and theoretical, seldom geophysical. The relatively complete dataset of wave-wave interactions is therefore a new contribution to wave-wave interaction studies.

Finally, internal waves are observed in many places and identifying generation time and location is important for many scientific reasons. With the dataset we obtained in the Strait of Georgia, the fourth objective of this thesis is to study the generation mechanisms of the observed internal waves by attempting to locate the time and position of generation. A relatively simple ray propagation method is used. Fully three dimensional models are complicated and it is important to find out how well simple methods work in these situations. Even with fully nonlinear models surface current is still a problem, the fourth objective is to see if this simple approach is adequate in identifying generation location and time.

In general, the data obtained are sufficient for us to fulfill the above aims. Both the

water column data and the photo images are synchronized in time, allowing us to identify and track a particular wave or set of interacting waves. The water column data allows us to measure the amplitudes and vertical structures of internal waves and the background density and shear. Sequences of photogrammetrically mapped photo images allow us to estimate the propagation directions and speeds of internal waves, and their horizontal scales.

Chapter 2 provides descriptions of our survey region of the Strait of Georgia, the details of field work, and of data processing. Chapter 3 mainly discusses the fits to a variety of classical model equations to describe the observed internal waves. Sixteen case studies are examined, at first without and then with background shear currents. The data are fitted to two-layer and continuously stratified model equations. Chapter 4 is a study of wave-wave interaction. With the available data, theories are applied and our observed wave-wave interactions are classified into three general types: Mach interaction, interaction which varies from known small amplitude interaction patterns, and shallow angle interaction. In Chapter 5, wave generation is studied for six cases and a similar generation mechanism is proposed for all of the six cases.

Finally, Chapter 6 provides a summary and discussion of the thesis work and discussion and suggestions of related research work in the future.

Chapter 2

Field Studies in the Strait of Georgia and Data Processing

2.1 Strait of Georgia

The Strait of Georgia is a large marine waterway on the west coast of North America. As shown in Figure 2.1, it is partially enclosed by islands with Vancouver Island forming the western boundary. The Strait of Georgia, which extends southeast-northwest from a latitude of 48.83°N to 50°N, is about 220 km long and 33 km wide. It has an average depth of 150 m with a small fraction of the total area exceeding 350 m. The tide has a maximum range exceeding 4 m in the Strait. The Fraser River discharges near the main entrance of the Strait of Georgia and its plume dominates the southern strait especially in late spring and early summer. Naturally occurring internal waves are often observed at the 2 to 4 m deep interface between the surface brackish water and deep salty sea water and, because these waves appear close to the surface, result in features visible to the naked eye (Shand 1953; Turner 1973; Leblond and Mysak 1978).

The first observations, using aerial photographs, date back to 1950. These photo images were examined by Shand (1953) and Tabata (1972) and internal wave packets of significant size were recognized. Internal waves in this strait have also been observed by synthetic

aperture radar (SAR) (e.g. Hughes and Gower 1983; Hughes and Gasparovic 1988; Hughes and Dawson 1988). Previous studies of internal waves in the Strait of Georgia also include Gargett (1976). One difference between the Strait of Georgia and other ocean regions is that the summer weather of the Strait of Georgia is often calm and sunny, which facilitates photo imaging. Internal waves are generated at numerous locations and this thesis shows that propagation and interactions can be observed. Thus, the Strait of Georgia forms a useful natural geophysical laboratory.

Most field work supporting this thesis was carried out in the summer of 2002. However, some preliminary work was carried out the previous summer in order to test the feasibility of the observational methods. This preliminary work included cross-strait surveys to locate internal waves, coordination exercises between aircraft and surface craft, and some data gathering. The modest number of images and water column measurements obtained enabled us to identify several single waves and determine their speed.

2.2 2002 Observations

Our analysis combines geo-located airborne oblique sea surface photo images with time-synchronized in-water CTD (Conductivity-Temperature-Depth probe), ADCP (Acoustic Doppler Current Profiler), echo sounder, and thermistor string (T-chain) measurements. Preliminary reconnaissances suggested that internal waves could reliably be found between Active Pass and Point Roberts beginning at low slack water. Both spring and neap tides in relatively calm conditions were sampled.

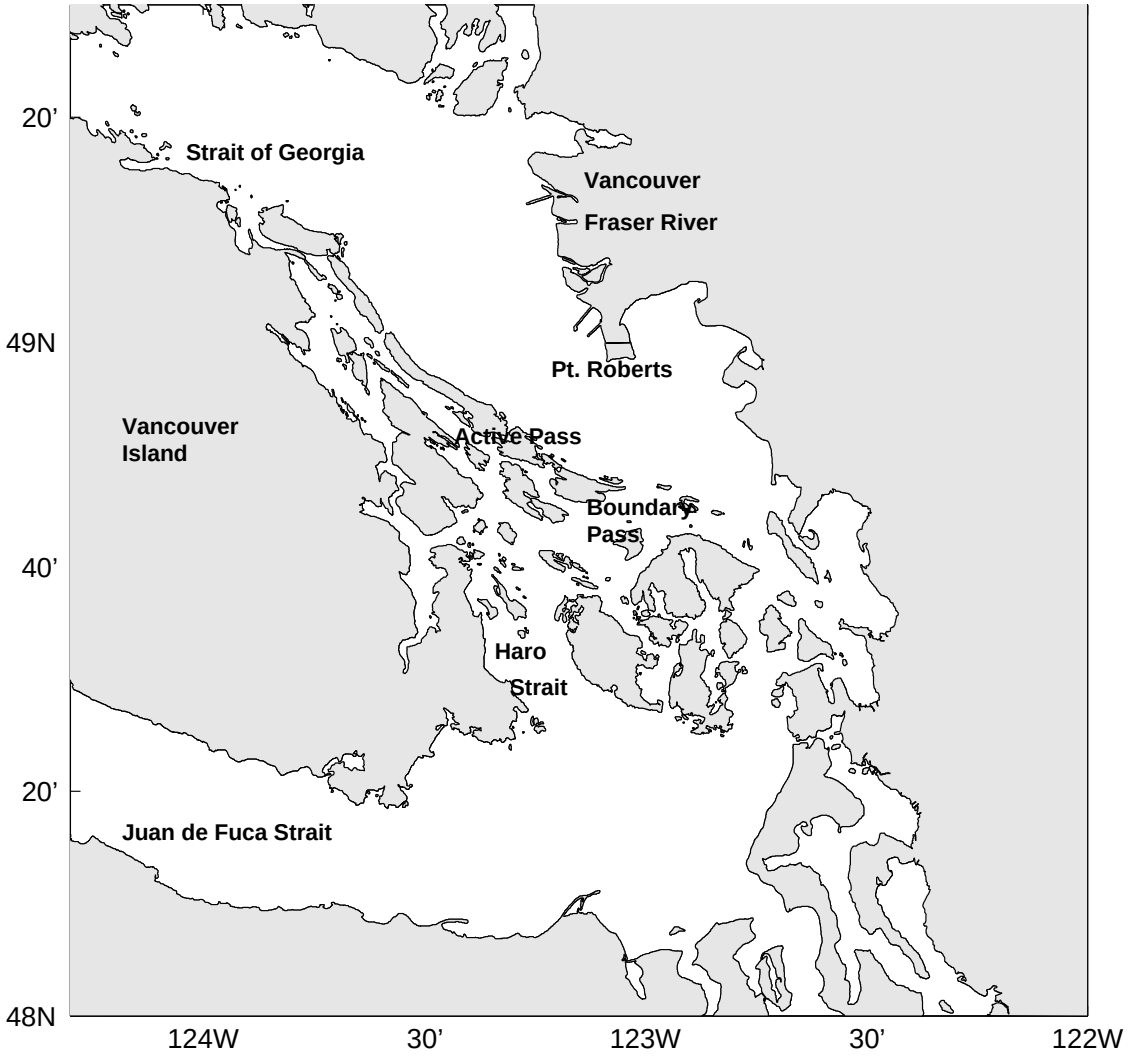

Figure 2.1: Map of the southern Strait of Georgia. The intensive field work for this thesis research is carried out mostly in the region between Active Pass and Point Roberts.

2.2.1 Water Column Data

The in-water data acquisition of this study was performed on the hovercraft "SIYAY" (an air cushion vehicle) belonging to the Canadian Coast Guard, stationed at Sea Island in Richmond, British Columbia. The instruments used are listed below:

1. A 300 kHz RD Instruments Workhorse "Sentinel" Acoustic Doppler Current Profiler (ADCP), employed to take both traditional sonar backscatter and current measurements. The velocity resolution of this device is 1 mm s^{-1} and the accuracy is ± 1 cm s^{-1}. The ADCP was mounted to a steel post and the transducer was lowered below the water surface using a hydraulic crane at the bow of the hovercraft.

2. A Seabird Electronics SBE25 CTD, which measures salinity and temperature profiles, deployed from a hydraulic winch.

3. A transducer co-mounted with the ADCP, connected to a 100 kHz echo sounder to collect high resolution backscatter data.

4. A chain of thermistors deployed over the side of the hovercraft. Temperature was measured at nominal depths of 2, 3, 4, 5, 6, 8, 10, 12, 16, and 20 meters using RBR TR-1000 loggers with a response time of less than 1 second. An XL-200 unit with a pressure sensor was placed at 21 m to monitor the position of the bottom of the chain.

5. A Global Positioning System (GPS) receiver continuously monitored the hovercraft's position throughout the study.

The hovercraft was a useful platform because it could travel at high speed (40 knots) to an internal wave packet located by the aircraft. However, once at a station with instruments deployed, it was no longer able to ride on its air cushion and its speed through the water in "boating" mode was no more than 2 knots.

2.2.2 Aerial Data

Oblique photo images were taken from a four passenger chartered "Beaver" float-plane using digital cameras. The cameras used were Kodak models DC265 and DC290. These cameras have an internal programming capability which was used to automate some of the setup parameters. In addition they were programmed to output a serial string when a photo was taken and this was logged with GPS data. The DC265 has a CCD (Charge Coupled Device) resolution of 1548 x 1032 pixels and the lens focal length is 38 mm to 115 mm equivalent. The DC290, a newer version of the DC265, has a CCD resolution of 1901 x 1212 pixels and the lens focal length is 38 mm to 115 mm equivalent. A GPS recorded the track and the altitude of the aircraft. A tilt-meter was attached to the base of the camera to measure camera's clockwise tilt, dip below horizon, and azimuthal rotation from magnetic north with an accuracy of a few degrees in the absence of acceleration. Tilt-meter, GPS and the photo time stamp information were stored continuously onto a laptop on board.

Ideal weather conditions for photo imaging are sunny and calm without many cloud shadows or rough surface waves. During a strait-wide survey, the altitude of the aircraft was as high as 1000 m to obtain a larger field of view, but during coordinated sampling with the hovercraft, the aircraft flew at an altitude of about 400 m and followed a square track several kilometers across, centered on the target area (Figure 2.2). This provides images at a dip angle of 5 – 10° (optimal for seeing surface reflectance variations). To aid accurate rectification, the photo images were taken to include both the wave feature of interest and either the coastline horizon and/or hovercraft to provide a known reference.

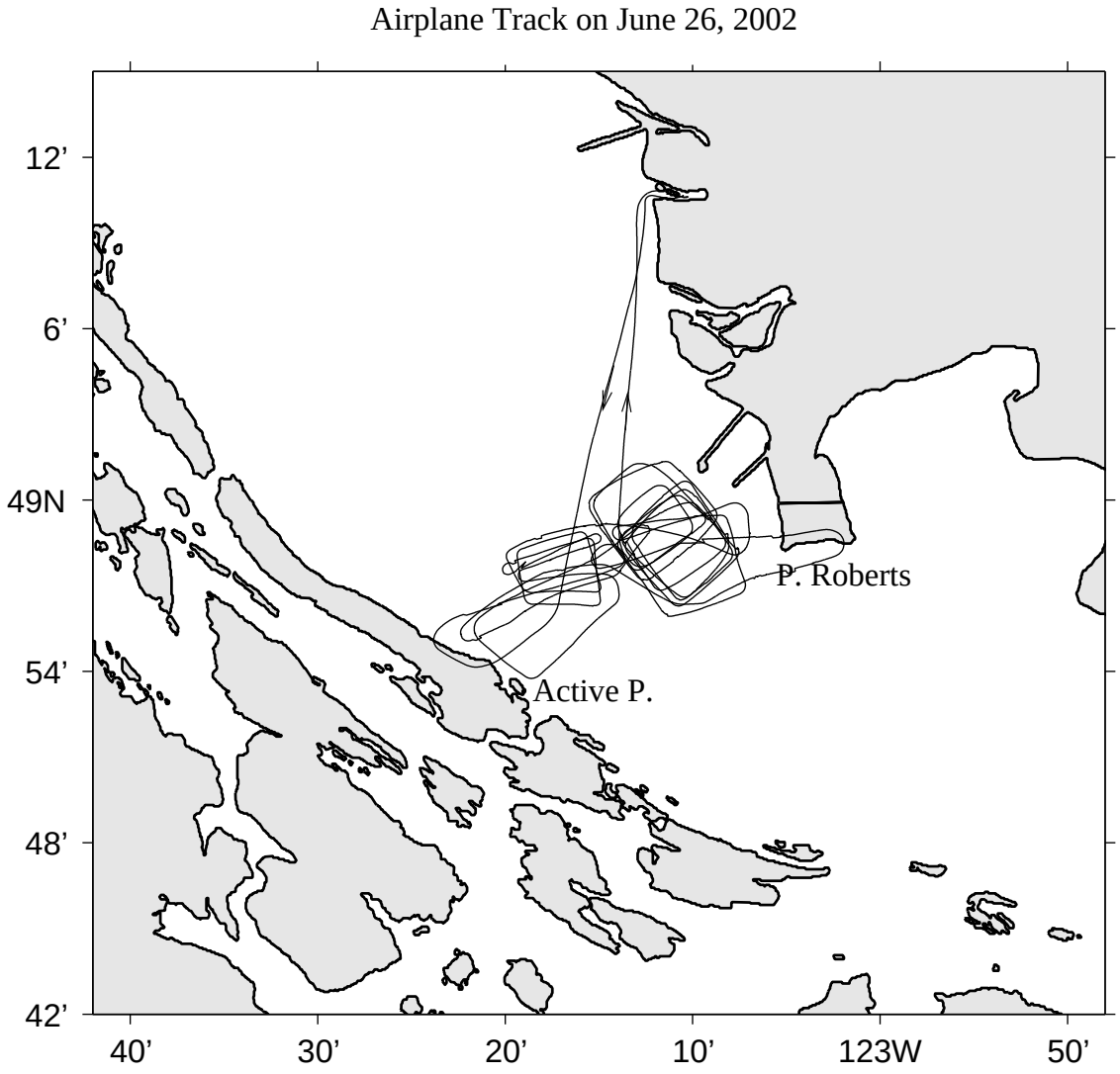

Figure 2.2: The track of the airplane on June 26, 2002. Typically, after leaving the airbase, the float airplane would fly to the Active Pass area. A cross-strait survey between Active Pass and Point Roberts was carried out to locate suitable internal wave packets. Once the hovercraft was directed to the chosen location, the aircraft would fly in a square pattern. Intensive surveys were carried out for two packets during this survey.

2.2.3 Cruise Summary

In the summer of 2002 from mid-May to mid-July eight sampling days were completed (see Table 2.1). During the first trip on May 15, only the aircraft was deployed. The purpose of this trip was to test the photographic equipment and to carry out a complete strait survey during a spring tide. A similar survey during a neap tide was carried out on June 3. In five of the trips, a survey was done either along the west side of the strait or across the strait from Active Pass to Point Roberts. Large internal wave packets were found stretching from Active Pass to Point Roberts. Oblique internal wave-wave interactions were identified at either Active Pass or off Roberts Banks.

During the remainder of the surveys, the aircraft would locate internal waves of interest and direct the hovercraft there by radio. While the hovercraft was present, a CTD profile was gathered immediately ahead of one of the large wave packets and other instruments deployed. The hovercraft would then travel perpendicularly at a low speed (about 2 knots) in boating mode through several crests of the wave packet. During the last two trips in July 2002, a more complex survey was attempted. A CTD station was made in front of the first crest of one packet and then a transect was made through the undisturbed waves of that packet. After three or four crests, the hovercraft then turned into the interaction area towards the other packet. Due to the relatively slow speed of the hovercraft and the relatively fast propagation of the wave packet, the equipment was then retrieved and the hovercraft repositioned ahead of the front of the second packet to again acquire data.

Survey Date	Tide	A/C time (PDT)	Survey Route	Large IW Location	W-W interaction Location	No. of Photo images Taken	H/C Deployment
5/17/2001	Spring	N/A	N/A	N/A	N/A	N/A	Yes
5/30/2001	Spring	N/A	N/A	Sturgeon Bank	N/A	N/A	Yes
6/7/2001	Neap	16:00–17:00	Sea I. – Active P.	Active P.	N/A	83	No
7/4/2001	Spring	12:00-15:00		Active P.	Active P.	90	Yes
5/15/2002	Spring	12:40–14:55	Pt. Atkinson – Boundary P.	Active P.	N/A	64	No
5/24/2002	Spring	11:00–14:00	N. Galiano Is.– Boundary P.	Active P.	Active P.	247	Yes
6/3/2002	Neap	13:10–14:10	N. Galiano Is.– Boundary P.– Pt. Roberts	Pt. Roberts	N/A	111	No
6/7/2002	Neap	10:30–12:30	Active P.–Pt. Roberts	Active P.		111	Yes
6/10/2002	Spring	13:00–15:00	Active P.–Pt. Roberts	Active P.	Active P.	292	Yes
6/25/2002	Spring	13:15–15:40	Active P.–Pt. Roberts	Active P. and Pt. Roberts	Pt. Roberts	161	Yes
6/26/2002	Spring	13:30–16:30	Active P.–Pt. Roberts	Active P. and Pt. Roberts	Pt. Roberts	338	Yes
7/15/2002	Spring	14:00–17:00	Active P.–Pt. Roberts	Active P. and Pt. Roberts	Pt. Roberts	69	Yes

A/C: Aircraft; H/C: Hovercraft; IW: Internal Wave; W-W interaction: Wave-Wave Interaction.

Table 2.1: Cruise summary.

2.3 Data Processing

2.3.1 Water Column Observations

The water column data allow us to observe wave amplitudes, density profiles, barotropic tidal currents, and background shear currents. Water depth in the study area varies, but was generally greater than 120 m. Observable structure associated with internal waves was limited to the upper 20 – 30 m.

Wave Amplitude

As solitary-like waves pass a point isotherms are displaced vertically and then return to their original depth. Our measured internal wave amplitude was therefore found by examining isotherm displacements in T-chain data. However, the T-chain did not hang vertically but was generally advected by the sheared currents, especially inside internal waves. A pressure sensor was placed on the bottom of the chain and data was linearly depth-corrected using this pressure data. In a particular wave, isopycnals near the surface and at depth have small displacements and an isopycnal at some intermediate depth has the largest displacement. This maximum displacement was taken to be the wave amplitude. Data sometimes showed that the isopycnal depth after the wave passed was slightly different from that in front of the wave. This could occur either because the depth correction was not completely accurate or due to asymmetries in the actual wave forms. In these cases, the average of the downward and upward displacements will be taken as the wave amplitude and the associated error bar (usually about 10 %) is the difference between the average and the two values. The undisturbed depth of the isopycnal with the maximum displacement is roughly where the layer interface is located in two-layer approximations. A further issue with the data is that the transect speed was relatively slow compared to the wave speed and the hovercraft could

sometimes get "trapped" in a particular wave. Data (especially T-chain data) could be affected by this, appearing more irregular than is probably the case.

Density Profile

Density profiles are generally provided by CTD data taken near a particular wave. Technical difficulties resulted in no CTD measurements on June 25 and June 26. However, CTD profiles from June 5 and July 10 in the same area are available from another research program and they were used to estimate the actual profile. Here June 26 is taken as one example. It is assumed that June 26 has the same $\sigma - T$ relation as June 5 and July 10 ((Figure 2.3). In Figure 2.3, the gray solid curves are from CTD stations on July 10 and the gray dashed curves are from June 5. The thick solid line is the fit to gray curves considering that July 10 is closer to June 26 and therefore is assumed to resemble the situation on June 26 better. Therefore, with the temperature data on June 26 provided by T-chain data and the $\sigma - T$ relation derived from the CTD profiles of June 5 and July 10, the density profile on June 26 can be estimated (Figure 2.4). The top 20 m of the profile is derived from the $\sigma - T$ relation. The bottom part from 20 m to 120 m was borrowed directly from the CTD data of July 10, 2002, as the water stratification below 20 m in the Strait of Georgia did not change greatly. The density profile of June 25 was estimated in the same manner.

Background Currents

The effects of water currents on internal wave propagation can be separated into those due to the barotropic or depth averaged current and those due to the baroclinic or vertical shear current. Waves are simply advected by the barotropic tide, whose effects are estimated by taking the depth average current. This advection is a translation with no dynamic

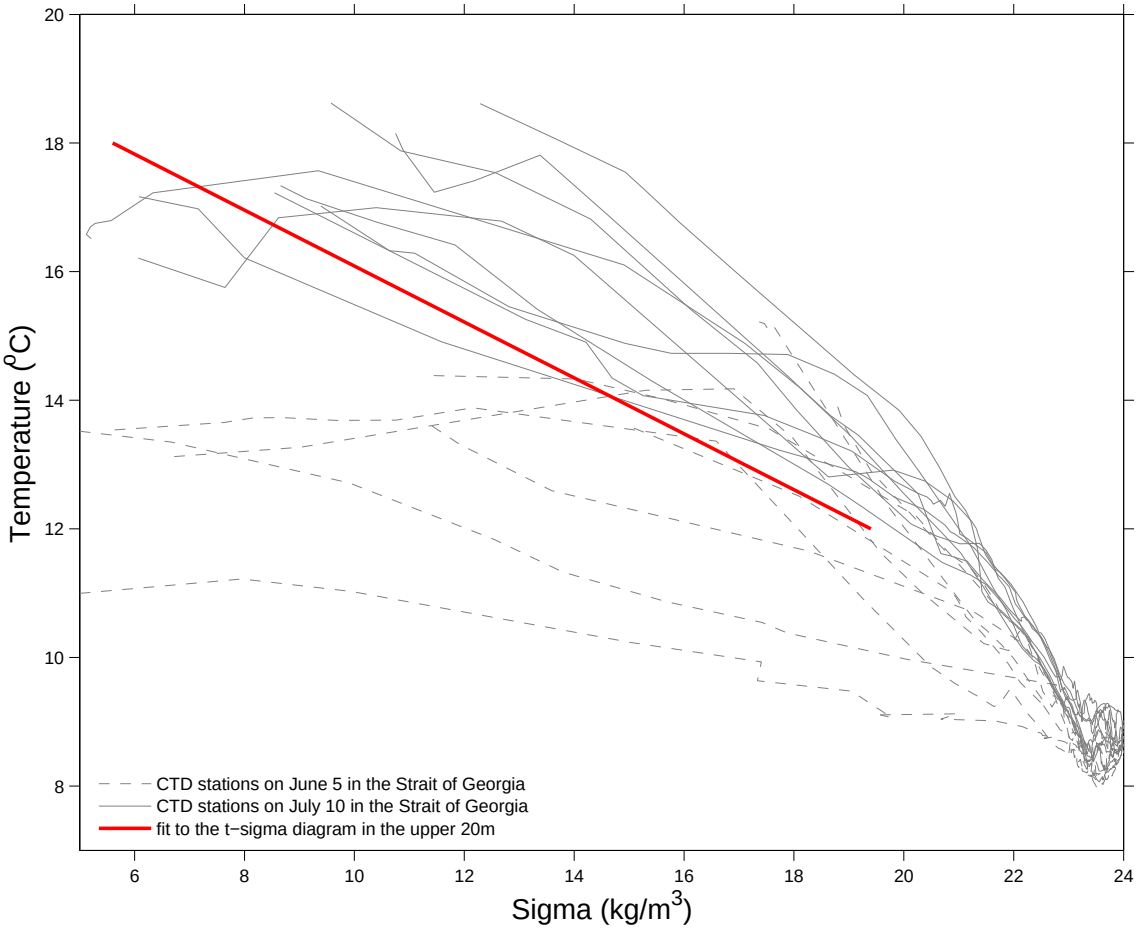

Figure 2.3: $\sigma - T$ data from CTDs on June 5 and July 10, as well as the estimated relation used to generate density profiles from T-chain temperature profiles on June 26. The gray solid curves are from CTD stations on July 10 in the Strait of Georgia. The gray dashed lines are CTD stations on June 5. The thick straight line is the fit to the gray curves.

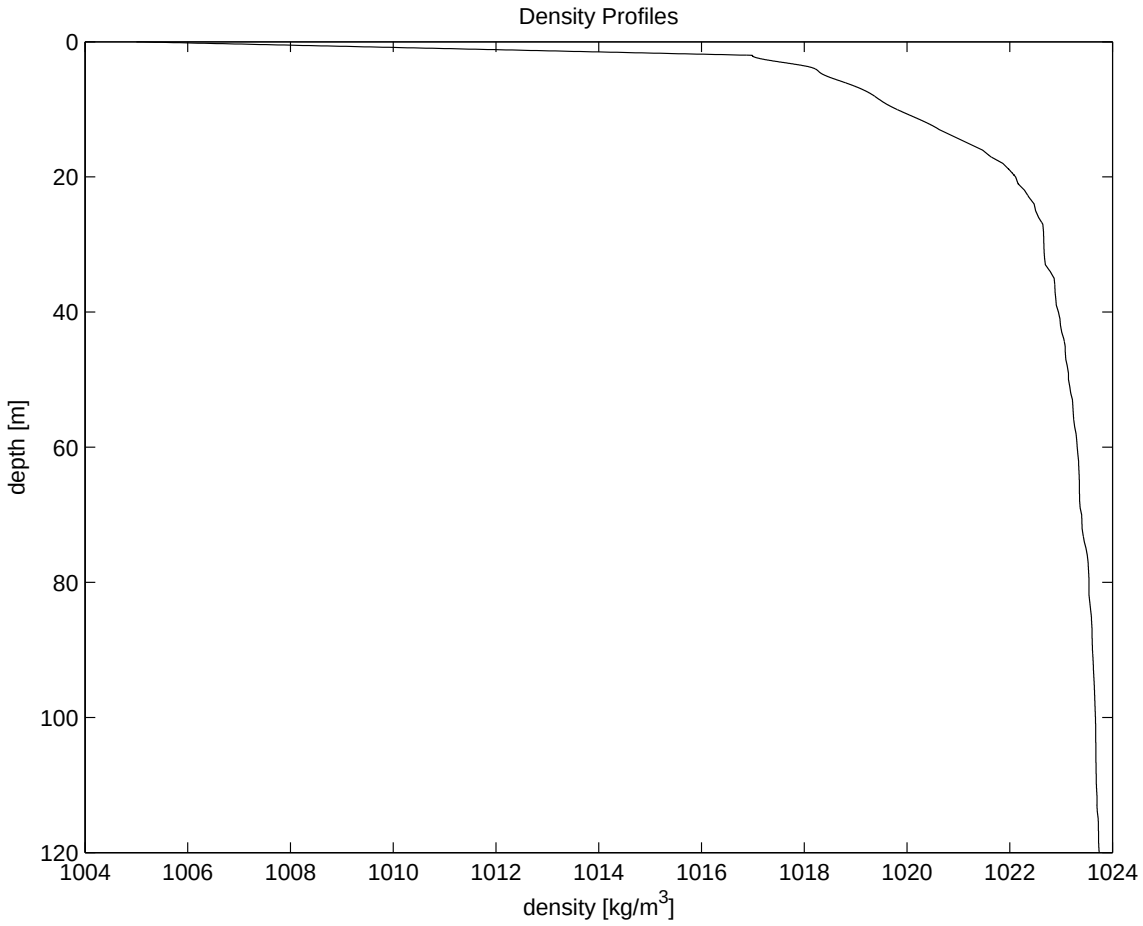

Figure 2.4: The density profile for June 26, 2002. The rapid density variations are confined to a shallow layer (about 30 m deep) near the water surface. Below this layer, the density does not vary much.

relevance. However, shear currents in the water column can change the wave shape and speed. In both cases, the current is projected on the wave normal and only that component is used in modeling. Both the barotropic and shear currents were obtained from segments of the data that did not include waves - either before the leading wave or between waves.

ADCP velocity profiles are contaminated by noise. In computing the effect of shear this raw data was used, but it was found that wave characteristics computed with vertically smoothed profiles only differed by $\approx 3\%$, which is smaller than other uncertainties (Figure 2.5), so smoothed ones are used. The downward-facing ADCP does not measure currents in the upper 1.5 m. The data are extrapolated by assuming currents were the same as the topmost measured value.

2.3.2 Aerial Imaging

Raw photo images (e.g. Figure 1.1) have to be rectified, photogrammetrically mapped to ground coordinates, and then processed using a series of filters and image processing tools before they become actually useful (i.e., in the form shown in Figure 2.6). This process is detailed in Pawlowicz (2003) but is summarized here. First, the pixel location is transformed into camera coordinates, identified as a view vector pointing from the center of the camera. Second, this vector is described in earth coordinates. Third, the relative intersection of this view vector with the ground plane is found and the curvature of the earth is accounted for. Finally, the coordinates of the ground point relative to the camera are converted to true ground coordinates. In order to carry out this transformation, the latitude, longitude, and altitude of the camera/aircraft, three orientation angles (rotation, dip below horizon, and tilt around view axis), and camera parameters such as field of view are required. Other image processing was also applied to remove trees (when seen) and

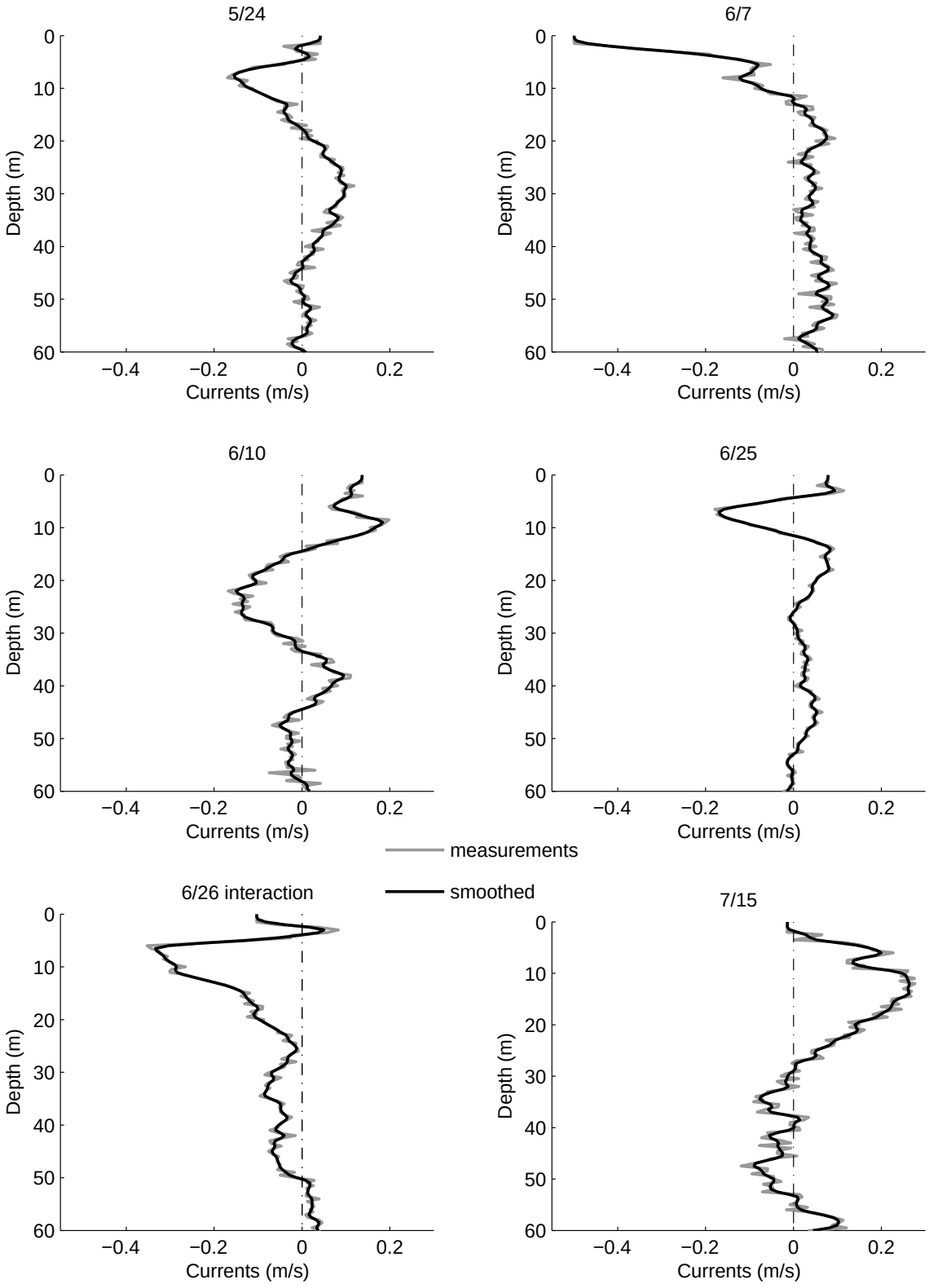

Figure 2.5: Smoothed baroclinic currents ahead of the waves in the top 60 m. Below this depth, the baroclinic currents are very small. These currents are obtained by subtracting the barotropic tide from the ADCP currents and then projecting onto the wave propagation direction. Original (gray) and smoothed (black) data is shown. Analyses with the smoothed or the actual unsmoothed data are not significantly different.

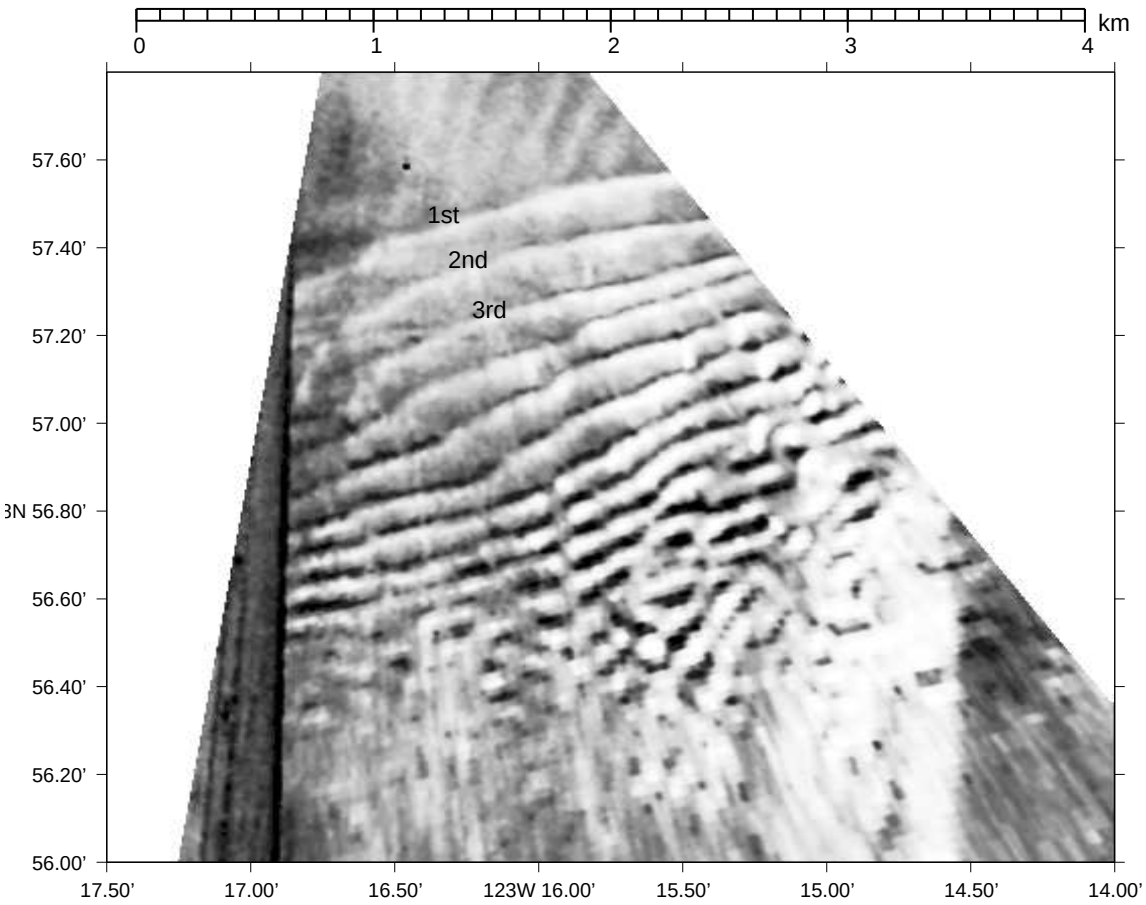

Figure 2.6: The wave packet observed around Active Pass on June 26, 2002. Original image can be found in Figure 1.1. Note that the leading six or so waves are not interacting with each other. However, the wave pattern is quite complex at the trailing end of the packet. The dark area at left is a wing of the airplane. Hovercraft "SIYAY" is the dot about 300 m ahead of the first wave.

speckle, and to get rid of the dark edges that arise from lens properties (vignetting) by subtracting a fitted function of the camera focal length.

Some uncertainties were involved in photo image mapping. Although the GPS measurements of the aircraft latitude and longitude are reasonably accurate, the orientation angles are sometimes not as precise as required, especially when the plane is changing altitude or making sharp turns, because the tilt meter is sensitive to accelerations. The measured altitude is also somewhat prone to large jumps when the aircraft orientation is changing,

and this requires some manual corrections. The relative orientation of camera and tilt meter varied from cruise to cruise due to mechanical variations in the attachment. Therefore, the recorded camera angles of tilt, rotation, and dip and the camera altitude had to be altered slightly by matching known locations and directions such as the coastlines and the position of the hovercraft before the photo images were successfully mapped. The average corrections of the three angles of tilt, rotation, and dip are 5°, 10°, and 3°, respectively. The tilt angles vary between -10° and 10°. The rotation angles range from 0° to 360°. The dip angles are around 6°. The corrections to the altitudes (when made) are about 50 m while the average altitudes during intensive photo imaging are around 400 m. The errors induced by all of the above result in an uncertainty in wave position, and are estimated as part of the error bars in derived characteristics.

Note that the same wave often appears differently in different photo images. This is because that the appearance of the water is a mixture of the specularly reflected sky light and the light returned after being scattered within the water column (Pawlowicz, 2003). Therefore, in photo images taken from different directions the wave slicks have varying brightness and thickness. Brighter or wider slicks on the photo images are not necessarily bigger than those appear darker or narrower. The leading edge and the trailing edge of an internal wave can be identified from photo images Figure 2.6). In images like Figure 2.6, the wave-wave spacing is the distance between dark edges in the wave propagation direction.

One of the most significant benefits of photo imaging is that it allows us to track a particular wave and calculate its propagation velocity. The phase speeds are taken to be the slope of the least square fit to wave positions, in the direction perpendicular to wave crests, with barotropic tides subtracted.

Chapter 3

Model Fitting and the Effects of Shear

Our dataset allows us to measure the propagation speed and other characteristics of individual internal waves. A very basic issue is the degree to which waves in the Strait of Georgia are adequately described by existing analytical models, which make various assumptions about the balance of different parameters as well as being strictly applicable only in very small but finite amplitude cases, i.e. with $\eta/h \ll 1$, where η is the amplitude and h the layer depth.

The internal waves in the Strait of Georgia typically have wave-wave spacing around 200 m. With the water depth of over 120 m, if we take $\lambda \approx 200$ m then $\tanh(kD) \approx 1$ (wave number $k = 2\pi/\lambda$), suggesting that deep-water dynamics are appropriate. It seems that deep-water models (ILW and BO equations) should be more applicable than shallow water models (KdV and eKdV).

However, according to our data, the waves observed in the Strait of Georgia have an amplitude η of 2 – 7 m, with an upper layer depth h_1 of less than 10 m. Therefore, the internal waves studied in this thesis work have amplitudes comparable to the upper layer depth, so a ratio of amplitude η to the upper layer depth $\eta/h_1 \approx 1$. These are not small-amplitude waves. On the other hand, their amplitudes are not maximal, either. A maximal

wave amplitude was found by Choi and Camassa (1999) to be:

$$\eta_m = \frac{-h_1 + h_2\sqrt{\rho_1/\rho_2}}{1 + \sqrt{\rho_1/\rho_2}}, \tag{3.1}$$

so that

$$\eta_m \longrightarrow \frac{h_2 - h_1}{2}, \tag{3.2}$$

when

$$\rho_1 \approx \rho_2, \tag{3.3}$$

where h_1 (h_2) is the upper (lower) layer depth, ρ_1 (ρ_2) is the density in the upper (lower) layer (Figure 3.1). Beyond this maximal amplitude, no solitary wave exists. The wave becomes a frontal-like internal bore wave. A solitary wave becomes a frontal wave when it is close to the maximal amplitude (Choi and Camassa, 1999).

Using values typical for the Strait of Georgia it is found that $\eta_m > 50$ m, which is about ten times the observed wave amplitudes. Apparently, the waves we are studying are quite far from being maximal waves. Therefore, our waves are neither small, weakly nonlinear, nor maximal.

Finally, as shown in Figure 1.1 and Figure 2.6, the internal waves in the Strait of Georgia often occur in packets, roughly rank-ordered. Thus they are not solitons. However, they typically have a wave-wave spacing around 200 m, far enough that at least the first few waves in the packet can be treated as "solitary-like".

Sixteen single waves were chosen for analysis. Waves were either from the same wave packet, or from different wave packets on the same day but at different locations, or from different wave packets on different days. Most of the cases were clearly propagating (e.g. like those shown in Figure 2.6) but several were near wave intersections and although the data

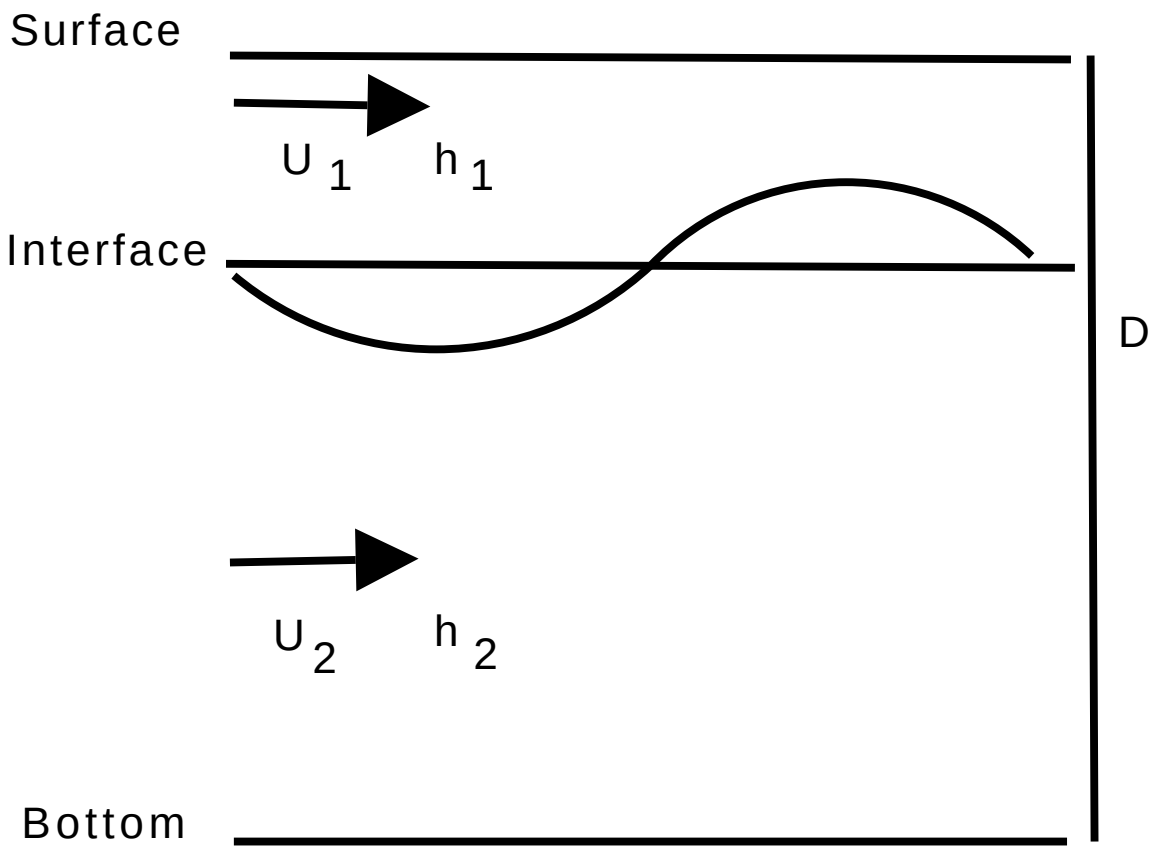

Figure 3.1: Definition sketch for the notation for two-layer sheared flows. The water depth is D, the upper layer depth is h_1, and the lower layer depth is h_2. The shear currents in the upper layer and the lower layer are U_1 and U_2, respectively.

Cases Studied	Active Pass Tide	Time with respective to Active P. Tide	Location	Observed Wave Phase Speed (m s^{-1})	Tidal Speed in Wave Direction (m s^{-1})	Wave Amplitude (m)	Interaction
5/24 Second wave	Spring	Peak Flood	Active P.	1± 0.08	0.3	6.2±0.4	No
5/24 Third wave	Spring	Peak Flood	Active P.	1.05± 0.09	0.3	7.3±0.5	No
6/7 First wave	Neap	Peak Flood	Active P.	0.75± 0.08	-0.1	2.2±0.2	No
6/7 Second wave	Neap	Peak Flood	Active P.	0.75± 0.08	-0.1	2.4±0.2	No
6/10 First wave	Spring	Beginning of Peak Flood	Active P.	1.05±0.04	0.55	3.0±0.4	**Yes**
6/10 Second wave	Spring	Beginning of Peak Flood	Active P.	1.1± 0.04	0.55	2.9±0.4	**Yes**
6/10 Third wave	Spring	Peak Flood	Active P.	1.1± 0.16	0.6	4±0.4	No
6/25 First wave	Spring	Peak Flood	Active P.	0.87± 0.11	0.32	6.1±0.5	No
6/25 Second wave	Spring	Peak Flood	Active P.	0.91± 0.12	0.32	6.4±0.6	No
6/26 wave 3	Spring	Peak Flood	Pt. Roberts	0.52± 0.08	0.2	2.3± 0.1	**Yes**
6/26 wave 4	Spring	Peak Flood	Pt. Roberts	0.76± 0.05	0.53	3.3± 0.3	**Yes**
6/26 First wave	Spring	Beginning of Peak Flood	Active P.	0.9± 0.09	0.26	2.8±0.3	No
6/26 Second wave	Spring	Beginning of Peak Flood	Active P.	0.86± 0.08	0.26	2.8±0.2	No
6/26 Third wave	Spring	Beginning of Peak Flood	Active P.	0.88± 0.08	0.26	2.6±0.2	No
7/15 First wave	Spring	Beginning of Peak Flood	Pt. Roberts	0.6± 0.03	0.16	3.8±0.4	**Yes**
7/15 Second wave	Spring	Beginning of Peak Flood	Pt. Roberts	0.57± 0.03	0.16	3.7±0.3	**Yes**

Table 3.1: The wave cases studied in model equation fitting. The observed phase speeds (with error) are calculated by digitizing photo images with the barotropic tide subtracted. The regular cases are single internal waves with no interaction nearby and the bold cases are waves that are in or close to a wave intersection.

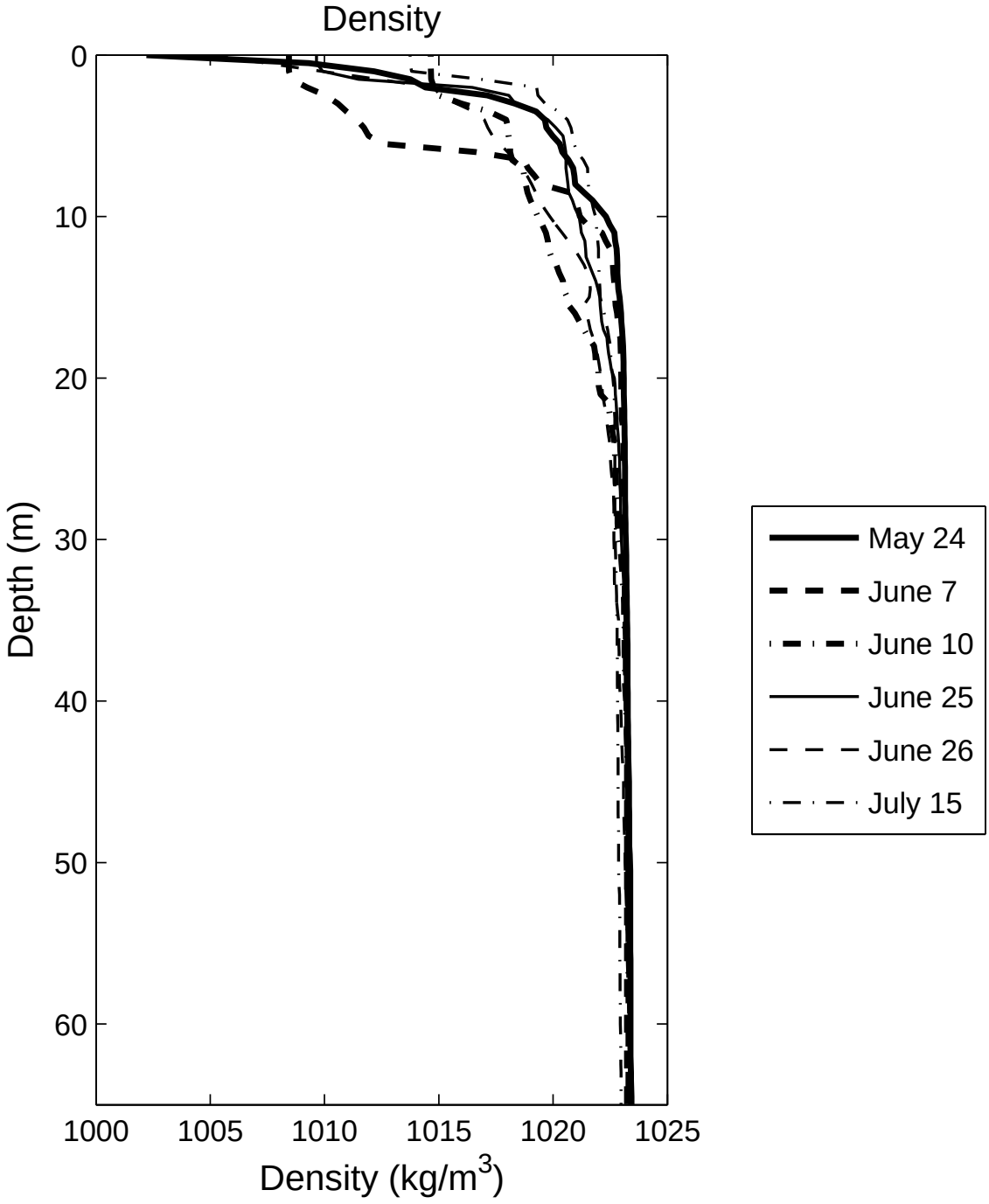

Figure 3.2: Density profiles for the studied cases. Only the top 70 m are shown. For all the six studied, densities remain almost uniform below 30 m. Variations of densities are confined in a shallow top layer (20 to 30 m deep). The rapid density variations are less than 10 m deep.

initially seemed useful, ultimately their propagation could not be explained satisfactorily, perhaps for this reason. The sixteen waves are listed in Table 3.1 and the stratification for each day is as shown in Figure 3.2. Largest density changes are confined to the upper 20 m. Densities decrease rapidly in the upper 5 m or so. Densities below 20 m remain almost uniform. Measured wave amplitudes range from 2.2 to 7.3 m, with phase speeds from 0.52 to 1.05 m s^{-1} superimposed on tidal currents of less than 0.6 m s^{-1}.

Although the stratification of the Strait of Georgia is far from being two-layered, we begin model fitting with two-layer models, first is to take the advantage of the simplicity of two-layer models, especially of the fact that the fully nonlinear equation has analytical solutions only under the two-layer situation. This allows us to compare the weakly nonlinear theories with fully nonlinear models without entering the complexity of pursuing numerical solutions. Second, the fitting to two-layer equations helps us to understand the effect of background shear currents to waves of different wave lengths. Third, it helps us to better understand the importance of the details of continuous stratification.

We will first fit our data to classic model equations with two-layer and continuous stratification without background shear currents, then fit to the same equations with two-layer and continuous stratification but with background shear currents. This approach is taken because density information is relatively easy to observe in many situations and it is of interest to see how well we can match the data when ignoring shear, although analysis in this chapter will eventually show that only the most complicated models (among those studied in this thesis) with continuous stratification and shear currents describe the observed internal waves in the Strait of Georgia.

As shown in the following section, the ILW solutions are a family of solutions of one parameter β. For the water system in the Strait of Georgia, the upper layer is very shallow

(< 10 m) compared to the lower layer (> 120 m), and after β is determined, the ILW solution is almost identical to the BO solution.

3.1 Two-layer Model Equations without Shear Currents

To take advantage of the simplicity of two-layer model equations, we first start with two-layer stratification. There are five possible analytical models in this case, including four weakly nonlinear equations (KdV, ILW, BO, and eKdV) and a strongly nonlinear equation.

The KdV equation for shallow water internal solitary waves in a two-layer fluid (Figure 3.1) is given by Osborne and Burch (1980) as

$$\eta_t + c_0\eta_x + \alpha\eta\eta_x + \gamma\eta_{xxx} = 0, \tag{3.4}$$

$$c_0 = [g(\Delta\rho/\rho)h_{eff}]^{1/2}, \tag{3.5}$$

$$\alpha = -(3c_0/2)\frac{h_2 - h_1}{h_1 h_2}, \tag{3.6}$$

$$\gamma = c_0 h_1 h_2/6, \tag{3.7}$$

where $\eta(x,t)$ is the amplitude of the solitary wave and satisfies $(\eta/h_{eff}) \ll 1$, h_1 is the upper layer water depth, h_2 is the lower layer water depth, and $h_{eff} = h_1h_2/(h_1 + h_2)$ is defined as the effective depth. For the KdV equation, layers are assumed to be of roughly similar depths, i.e. $h_2/h_1 = O(1)$. The soliton scale length must satisfy $\lambda/(h_1 + h_2) \gg 1$ with $\lambda = 2L$ and L is the half soliton width. Definitions of wave length and half soliton width are very similar to those of surface solitary waves defined by Osborne and Burch (1980) (Figure 3.3). Although L is called the half soliton width, to be exact, it is where the amplitude is reduced by $\mathrm{sech}(1) = 0.65$. Here c_0 is the phase speed of a linear internal

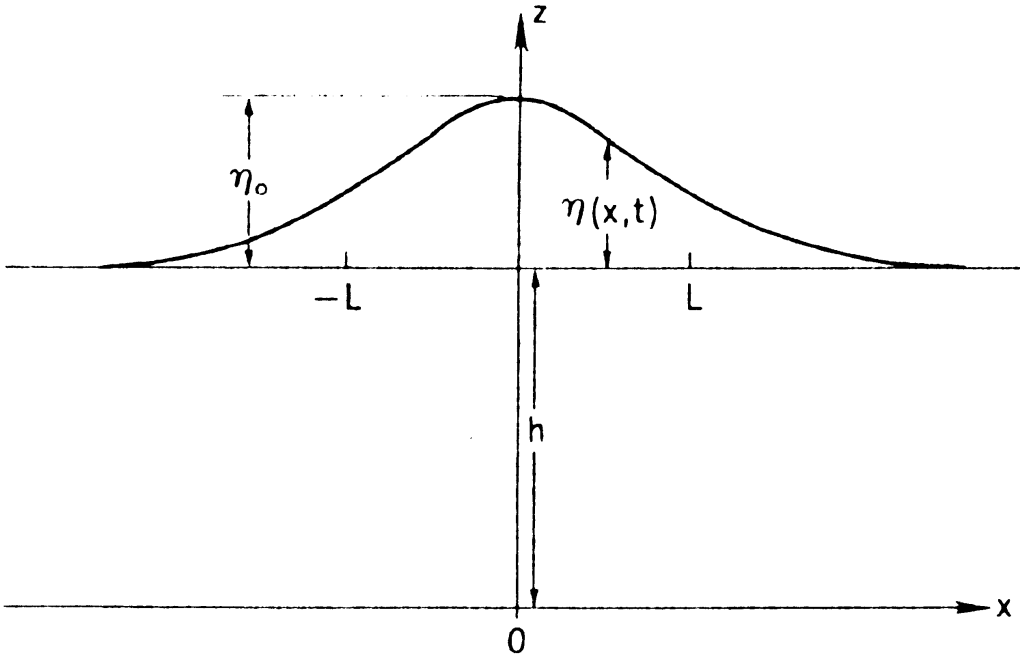

Figure 3.3: Surface solitary waves with amplitude η_0 in water of depth h. The solitary wave half width is L (Osborne and Burch, 1980).

wave in this system with density assumed as $\rho \approx \rho_1 \approx \rho_2$, $\Delta\rho = \rho_2 - \rho_1$. The vertical gravitational acceleration is g. When $h_1 < h_2$ ($h_1 > h_2$), only solitons of depression (elevation) are possible.

Assuming the upper layer is thinner than the lower layer, the internal solitary wave solution to the above equation is

$$\eta(x,t) = -\eta_0 \mathrm{sech}^2[(x - ct)/L], \tag{3.8}$$

with phase speed

$$c = c_0 - \alpha\eta_0/3, \tag{3.9}$$

and a soliton half width of

$$L = (-12\gamma/\eta_0\alpha)^{1/2}, \tag{3.10}$$

and $\theta = (x - ct)/L$ is the wave phase.

The horizontal velocities induced by the soliton (in the direction of the soliton propagation) in the upper layer are

$$u_1(x,t) = -\frac{c_0}{h_1}\eta(x,t), \tag{3.11}$$

and in the lower layer they are given by

$$u_2(x,t) = \frac{c_0}{h_2}\eta(x,t). \tag{3.12}$$

When the water depth becomes a little greater (water depth and wave length are of the same order), the dynamics are modified slightly and the ILW equation applies. The ILW equation is given by Choi and Camassa (1999) as

$$\eta_t + c_0\eta_x + \alpha\eta\eta_x + \gamma\Gamma_c[\eta_{xx}] = 0, \tag{3.13}$$

where

$$c_0 = [g(\Delta\rho/\rho)h_1]^{1/2}, \tag{3.14}$$

$$\alpha = -\frac{3c_0}{2h_1}, \tag{3.15}$$

$$\gamma = \frac{c_0 \rho_2 h_1}{2\rho_1}, \tag{3.16}$$

with the operator Γ_c defined by

$$\Gamma_c[f] = \frac{1}{2h_2} \int_{-\infty}^{+\infty} f(x^{'}) \coth \frac{\pi}{2h_2}(x^{'} - x) dx^{'}. \tag{3.17}$$

The solution of the ILW equation is a one parameter (β) family of solitary wave solutions

$$\eta_{ILW}(x,t) = \frac{-\eta_0 \cos^2\beta}{\cos^2\beta + \sinh^2((x-ct)/L_{ILW})}, \tag{3.18}$$

where

$$\eta_0 = \frac{4\gamma}{h_2 \alpha} \beta \tan\beta, \tag{3.19}$$

$$L_{ILW} = h_2/\beta, \tag{3.20}$$

$$c = c_0 - \frac{2\gamma}{h_2} \beta \cot(2\beta), \tag{3.21}$$

$$0 \leq \beta < \frac{1}{2}\pi, \tag{3.22}$$

and the parameters are assumed to satisfy $(\eta/h_{eff}) \ll 1$, and $h_2/h_1 \gg 1$.

In the limit as the depth of the lower layer becomes infinite, the BO equation applies. The BO equation is

$$\eta_t + c_0 \eta_x + \alpha \eta \eta_x + \gamma \frac{\partial^2}{\partial x^2} \mathcal{H}[\eta] = 0, \tag{3.23}$$

where

$$c_0 = [g(\Delta\rho/\rho)h_1]^{1/2}, \tag{3.24}$$

$$\alpha = -\frac{3c_0}{2h_1}, \tag{3.25}$$

$$\gamma = \frac{c_0\rho_2 h_1}{2\rho_1}, \tag{3.26}$$

where the Hilbert operator $\mathcal{H}$ is defined as

$$\mathcal{H}[f] = \frac{1}{\pi}\int_{-\infty}^{+\infty} \frac{f(x^{'})}{x^{'} - x} dx^{'}. \tag{3.27}$$

As $h_2 \to \infty$ and $\beta \to \frac{1}{2}\pi$, the above ILW solution reduces to the BO solitary wave solution:

$$\eta_{BO}(x,t) = \frac{-\eta_0}{1 + ((x - ct)/L_{BO})^2}, \tag{3.28}$$

where

$$L_{BO} = \frac{4\gamma}{\eta_0 \alpha}, \tag{3.29}$$

$$c = c_0 - \alpha\eta_0/4, \tag{3.30}$$

The parameters c_0 (3.24), α (3.25), and γ (3.26) are the same as (3.14) – (3.16) for the ILW equation. The BO equation assumes that $(\eta/h_{eff}) \ll 1$, $h_2/h_1 \to \infty$. However, the final terms in (3.4), (3.13), and (3.23) differ.

In the Strait of Georgia, the values of parameters $\Delta\rho$, α, and γ are shown in Figure 3.4. These values depend on the assumed upper layer depth, whose range will be discussed later. However, if the upper layer depth h_1 is less than 10 m, the values of $\Delta\rho$ lie in between 5 and 20 kg m^{-3}, the parameter α is negative but greater than -1 s^{-1}, the parameter γ for KdV model is in the range of [0 200] m^3 s^{-1}, while for ILW and BO models it is less

than 5 $m^3\ s^{-1}$. From the above equation 3.19, using the typical values of η_0, h_2, α, and γ in the Strait of Georgia, the value of β is approximated to be within 4% of $\frac{1}{2}\pi$ and the ILW equation is effectively reduced to the BO equation. Therefore, ILW equation and BO equation can be treated as equivalent in the Strait of Georgia.

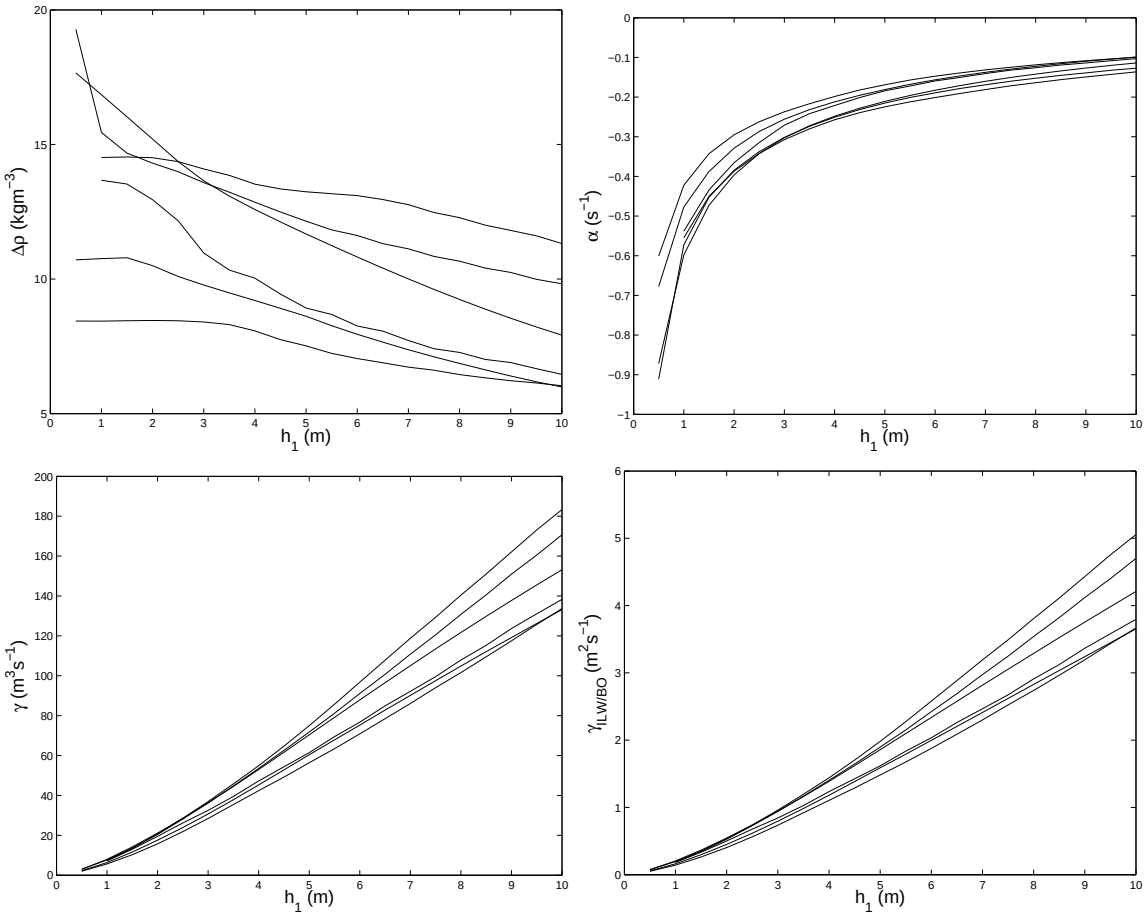

Figure 3.4: The typical parameter values in the Strait of Georgia are shown as functions of the assumed upper layer depth h_1. $\Delta\rho = \rho_2 - \rho_1$ is the difference between the mean density values in the upper (ρ_1) and the lower layer (ρ_2). The parameter α is the same for the KdV, ILW, and BO models. The parameter γ is for the KdV model and γ_{ILW} is for the ILW and BO models. The six lines in each panel represent the six studied days of May 24, June 7, June 10, June 25, June 26, and July 15.

If higher-order nonlinearities are important, then a relevant equation is the so-called eKdV equation. The eKdV equation is a variant of the KdV equation and it has the same

range of applicability as the KdV equation, i.e., it is applicable to small amplitude, shallow water waves, and the two layers have similar depths. The eKdV equation is (Ostrovsky and Stepanyants, 2005)

$$\eta_t + c_0\eta_x + \alpha\eta\eta_x + \alpha_1\eta^2\eta_x + \gamma\eta_{xxx} = 0, \tag{3.31}$$

$$c_0 = [g(\Delta\rho/\rho)h_{eff}]^{1/2}, \tag{3.32}$$

$$\alpha = -(3c_0/2)\frac{h_2 - h_1}{h_1 h_2}, \tag{3.33}$$

$$\alpha_1 = \frac{3c_0}{{h_1}^2{h_2}^2}[\frac{7}{8}(\frac{\rho_2{h_1}^2 - \rho_1{h_2}^2}{\rho_2 h_1 - \rho_1 h_2})^2 - \frac{\rho_2{h_1}^3 + \rho_1{h_2}^3}{\rho_2 h_1 - \rho_1 h_2}], \tag{3.34}$$

For close densities,

$$\alpha_1 \approx -\frac{3}{8}c_0\frac{(h_1 + h_2)^2 + 4h_1h_2}{{h_1}^2{h_2}^2}, \tag{3.35}$$

where $\eta(x,t)$ is the amplitude of the solitary wave, h_1 is the upper layer water depth, h_2 is the lower layer water depth, and $h_{eff} = h_1h_2/(h_1 + h_2)$ is defined as the effective depth. Here c_0 is the phase speed of a linear internal wave in this water system with density assumed as $\rho \approx \rho_1 \approx \rho_2$, $\Delta\rho = \rho_2 - \rho_1$. The vertical gravitational acceleration is g. As follows from equation 3.35, for two-layer system, the coefficient α_1 is always negative.

In the case of negative α_1, the soliton solution is

$$\eta(x,t) = -\frac{\alpha}{\alpha_1}\frac{\nu}{2}\left[\tanh(\frac{x - ct}{\Delta} + s) - \tanh(\frac{x - ct}{\Delta} - s)\right] \tag{3.36}$$

where ν is a free parameter and satisfies $0 < \nu < 1$. The remaining parameters are

$$s(\nu) = \frac{1}{4}\ln(\frac{1 + \nu}{1 - \nu}), \tag{3.37}$$

$$\Delta = \sqrt{\frac{-24\alpha_1\gamma}{\alpha^2\nu^2}}, \tag{3.38}$$

$$c = c_0 - \frac{\alpha^2\nu^2}{6\alpha_1}, \tag{3.39}$$

and the amplitude of the soliton is

$$\eta_0 = |\frac{\alpha}{\alpha_1}\nu \mathrm{tanh}s|. \tag{3.40}$$

Finally, according to Choi and Camassa (1999), the strongly nonlinear solitary depression wave solution for waves in a two-layer water system with two layer depths being similar has speed

$$c_{NL} = c_0\sqrt{\frac{(h_1+\eta_0)(h_2-\eta_0)}{h_1h_2 + ({c_0}^2/g)\eta_0}}. \tag{3.41}$$

For this strongly nonlinear wave solution, there is no limitation of small wave amplitude.

3.1.1 Case Studies

The sixteen cases include ten single waves and six waves that are involved in interactions (Table 3.1). The classic models are for single waves, but, if we get measurements of an interacting wave far away from the interaction, we expect that the effect of interaction is minimal. All the sixteen cases are analyzed, but only the cases on June 26 and May 24 will be described in detail. For the cases on June 26, the waves at Active Pass will be first analyzed and then the waves near Point Roberts. The analysis of the other cases follow the same approach.

Single waves around Active Pass observed on June 26, 2002.

The waves observed in the Strait of Georgia typically have a spacing between wave crests around $100 - 250$ m and (as discussed in Chapter 5) have an along crest extent more than 10 km, which is comparable to the width of the Strait of Georgia. On June 26, there was a large internal wave packet observed outside of Active Pass. Figure 2.6 is an example of processed photo image taken of the single wave packet at Active Pass. The original photo image is in Figure 1.1. Figure 3.5 is the water column data acquired during this time period. It includes the sounder backscatter, the ADCP backscatter, the ADCP vertical velocity, the temperature data obtained by the T-chain with temperatures at 4 m, 5 m, and 6 m plotted on top, and the GPS recorded hovercraft speed (smoothed) in the wave propagation direction with tide subtracted. The same internal waves are found in sounder backscatter, ADCP backscatter, and the T-chain contours. ADCP backscatter has relatively coarse spatial resolution. The sounder backscatter has finer resolution. T-chain contour provides the finest spatial resolution, but is greatly affected by advection of the line below the hovercraft. The leading wave is on the left. From the ADCP vertical velocity (Figure 3.5 c)), there are positive (upward) vertical velocities associated with the trailing edge of each internal wave. The largest upward velocities are of order 0.1 m s^{-1}. The hovercraft speed (in Figure 3.5 f)) shows that the hovercraft is being affected by internal waves when it crosses against their propagation direction and this affects the details of temperature profiles (Figure 3.5 e)) since the T-chain is swinging relative to the hovercraft, making them look very asymmetric compared with the view shown by the echo sounder (Figure 3.5 a)).

By carefully matching up the time stamps of the photo images and the hovercraft positions on the images to the water column data by time, the first wave, second wave,

and third wave in Figure 2.6 are identified in the water column data of Figure 3.5. Their amplitudes can then be estimated from the temperature contours. The wave amplitudes measured from the T-chain data (Figure 3.5 e) are 2.8 ± 0.3 m for the first wave, 2.8 ± 0.2 m for the second wave, and 2.6 ± 0.2 m for the third wave. Wave phase speeds are calculated by using the image sequence with the average tide subtracted. The wave phase speeds for the three waves are found to be 0.9 m s^{-1}, 0.86 m s^{-1}, and 0.88 m s^{-1}, respectively, with about 10% uncertainty in each case (Figure 3.6). Due to the rectification error of individual photographs one circle appears above the least square fit on all the three plots. The wave speed is not varying. Rather, this variation arises from uncertainties of aircraft position and camera orientation.

In order to use two-layer models we must approximate the true density profile. Examining Figure 3.2 and Figure 3.5, it is not obvious where the two layers should be separated, although the upper layer depth must be less than 5 m. Since the waves are evidently first baroclinic modes (the vertical displacements are in phase at all depths through the thermocline), most reasonably the separation between the upper and the lower layer will be near the depth at which the maximum vertical velocities and zero horizontal velocities occur. The vertical velocities induced by the internal waves can be obtained after subtracting the depth average from the ADCP vertical velocity data, but it is rather hard to determine a peak or zero from the noisy current data. The undisturbed level of the isopycnal with the largest displacement (i.e. the wave amplitude) is an initial estimate of interface thickness for the two-layer model. Density of the layer is taken to be the average in each layer. We can test the sensitivity of a solution to the assumed value of the upper layer depth by varying it over a range of $0.5 - 6$ m although a more reasonable range is [2 4] m based on water column data. Fits to the first, second, and third wave are then tentatively applied

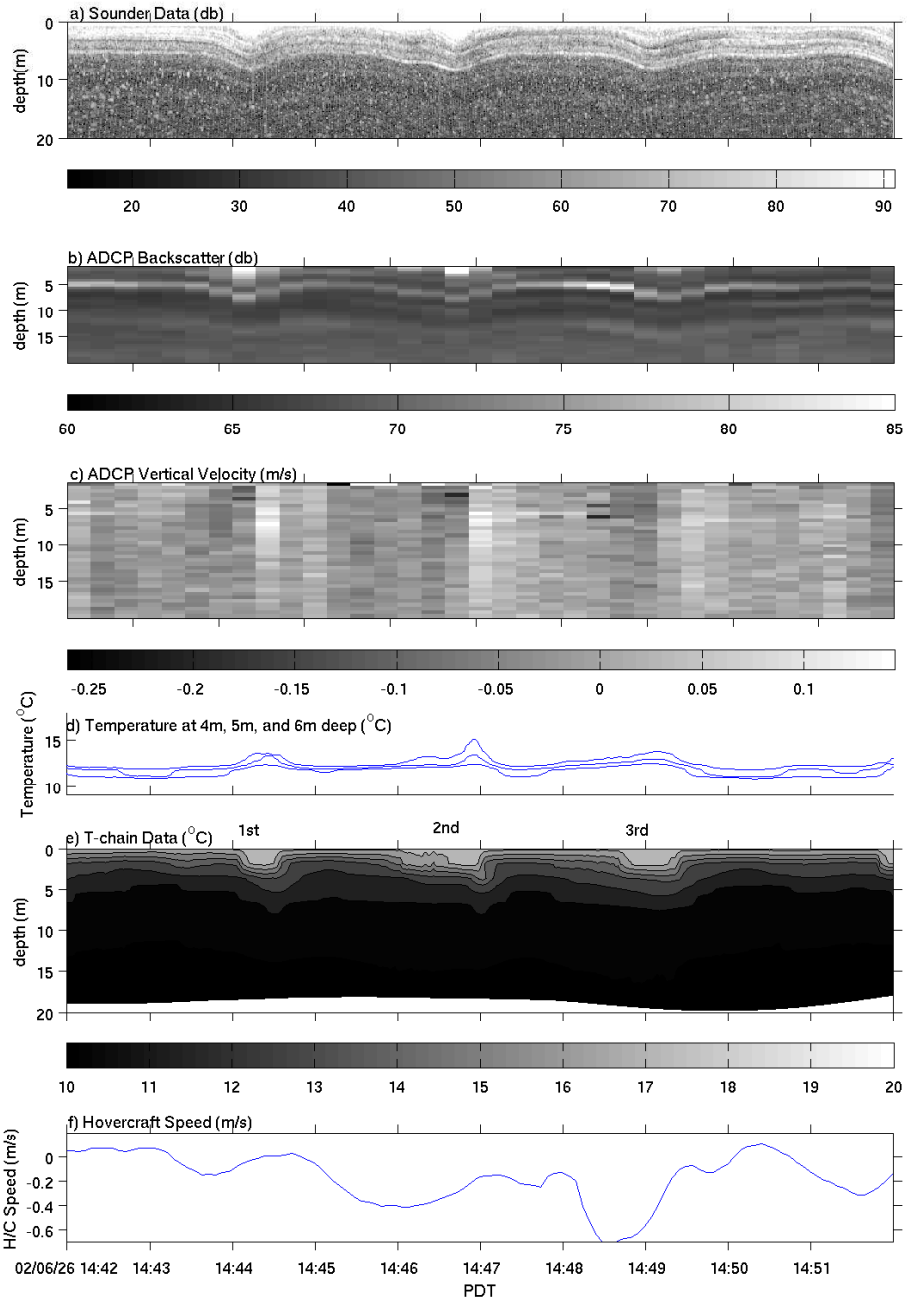

Figure 3.5: The in-water Sounder, ADCP, and T-chain data near Active Pass on June 26, 2006. a) echo sounder backscatter, b) ADCP backscatter, c) ADCP vertical velocity, d) temperature obtained by T-chain at depths of 4m, 5m, and 6m, e) T-chain temperature contours, f) hovercraft speed (smoothed) in wave propagation direction with tide subtracted. PDT is Pacific Daylight Time.

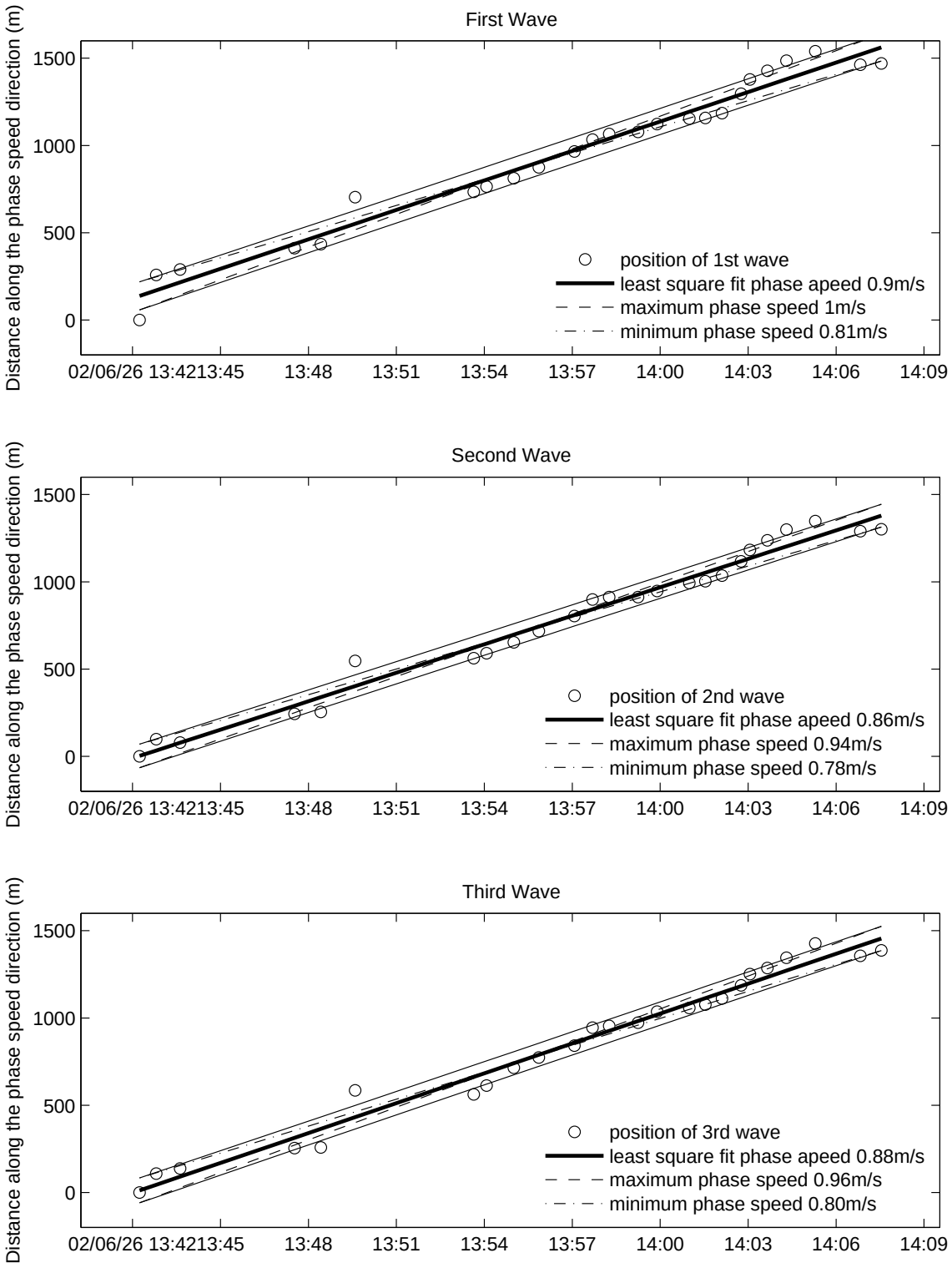

Figure 3.6: The positions of first, second, and third wave at different times and their calculated phase speeds with barotropic tides subtracted. The time and distances are calculated with the first image in the studied period as the reference and distances are measured perpendicular to crest directions. The horizontal-axis is Pacific Daylight Time (PDT).

with upper layer depths of $0.5 - 6$ m with the total water depth fixed at 120 m. The wave characteristics of the first, the second, and the third wave in the packet are applied to different equations to estimate wave phase speeds, which are then compared to observations. The results for the three waves are qualitatively the same, hence only the case of the first wave is shown in Figure 3.7.

Nonlinear wave equation (KdV, BO, ILW, eKdV, Strongly Nonlinear) phase speed predictions are always higher than linear predictions. KdV equation predictions are higher than other nonlinear predictions, especially when $h_1 < 4$ m. For this case, KdV prediction appears to be closest to the observed values although ILW and BO predictions are within the observational error. The predictions by eKdV model are lower than all the other studied nonlinear predictions, and are closest to linear predictions among all the studied nonlinear models. It is also found that as the upper layer depth h_1 increases: (1) the half-widths of the solitons increase and the soliton shapes get wider and flatter; (2) linear, eKdV, and strongly nonlinear phase speeds increase; (3) KdV and BO phase speeds first decrease rapidly with upper layer depth h_1, reach a broad minimum, and then slowly increase; (4) the differences between nonlinear and linear speeds decrease; (5) the upper layer particle speeds decrease.

The most noticeable effect of nonlinearity appears to be a change in phase speed. For small h_1 this change can be quite substantial. The second obvious feature is that nonlinear effects appear to compensate for large changes in c_0 (the linear phase speed) resulting in a broad flat minimum (KdV, BO, ILW) for predicted phase speed, of approximately constant magnitude. For $h_1 > 4$ all nonlinear equations (KdV, BO, ILW, eKdV, and strongly nonlinear) provide similar predictions. As expected, the wave phase speeds predicted by the ILW equation are very similar to those predicted by the BO equation for all the tested

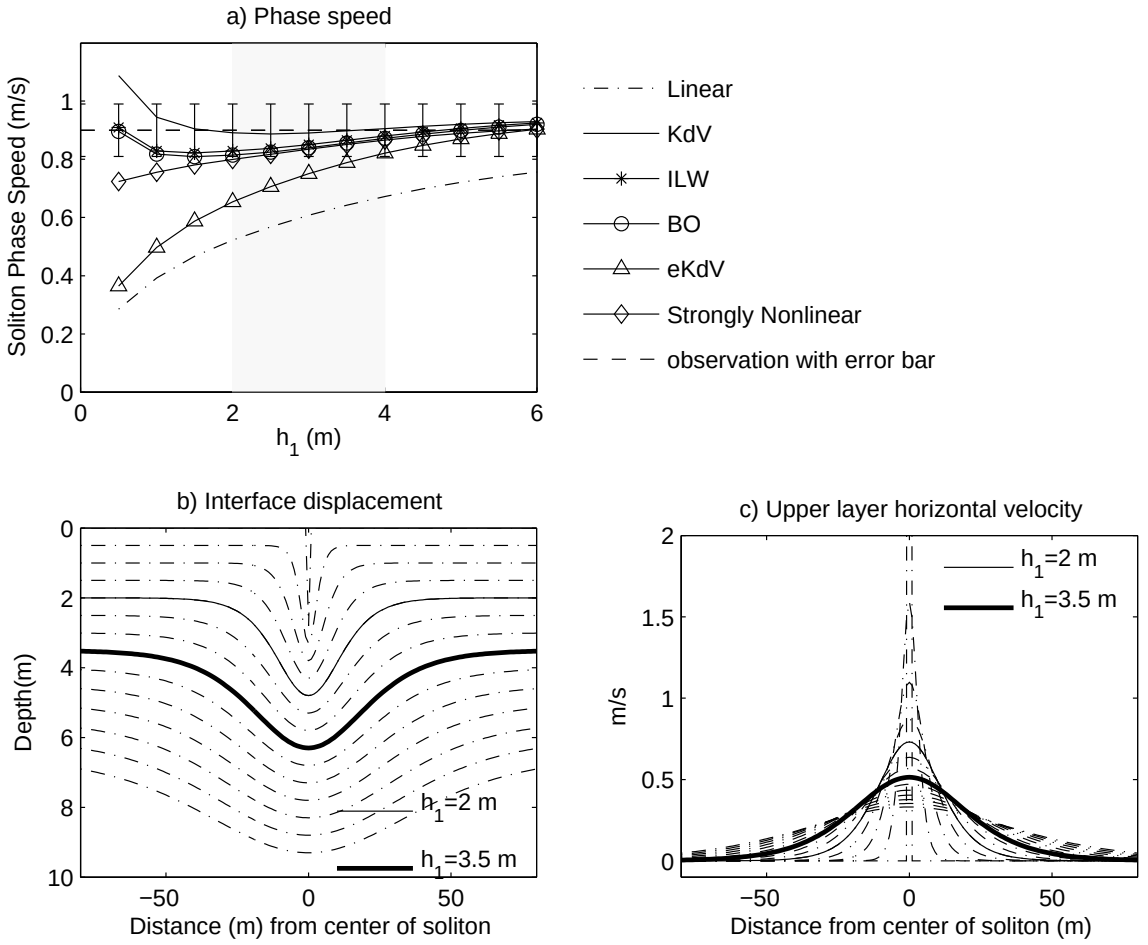

Figure 3.7: Sensitivity tests of the two-layer KdV, eKdV, ILW, BO, and strongly nonlinear wave models for the first wave in packet observed on June 26 near Active Pass. a) phase speeds estimated by different models as well as the observed values, b) interface displacement estimated by KdV model, and c) upper layer soliton induced horizontal velocity calculated by KdV model over a variety of upper layer depths between $0.5 - 6$ m and a fixed total water depth of 120 m. The shaded area in plot (a) shows the reasonable range of upper layer depth.

values of h_1. The strongly nonlinear model predicted wave speeds resemble BO model predictions when the upper layer depth h_1 is greater than 2 m.

Waves around Point Roberts observed on June 26, 2002.

On June 26, 2002, two wave packets (in Figure 4.4) were observed close to Point Roberts during the spring tide at Active Pass. The analysis of wave 4 (the wave labeled with number 4 in Figure 4.4) will be explained as an example. Wave 4 propagated to the north. After the average tide is subtracted, its phase speed is 0.76 ± 0.05 m s^{-1}. The estimated amplitude from T-chain data is 3.3 ± 0.3 m.

Comparison with predictions is shown in Figure 3.8. KdV speeds are higher than the observed speed. The observed speed is higher than the linear long wave speeds when h_1 is less than 7 m. No matter how we tune the two-layer model, the KdV model always overestimates speeds for wave 4. The two-layer linear model can be tuned to match observations by taking $h_1 \approx 7$ m, but the linear model is clearly inappropriate due to the nonlinear nature of the observed waves. KdV phase speeds reach minimum value when h_1 lies between 2 – 5 m. BO predicted wave speeds were lower than KdV predictions, higher than observations, but within the measurement error. The eKdV model predicted wave phase speeds are greater than linear speeds and lower than the other nonlinear models (KdV, BO, strongly nonlinear) when the upper layer depth is less than 5 m, including the reasonable range of [2 4] m in the Strait of Georgia. For small values of h_1 (< 2), the strongly nonlinear model predicted wave phase speeds are close to observed speed. The predictions of the ILW model is very similar to BO predictions and hence is not shown in this figure. The strongly nonlinear and BO models predicted similar wave speeds for $h_1 > 2$ m. When the upper layer depth increases the BO and eKdV estimated speeds gradually approach those of the

KdV equation. In the reasonable range of h_1 in the Strait of Georgia ([2 4] m), both eKdV and linear predictions are lower than observations.

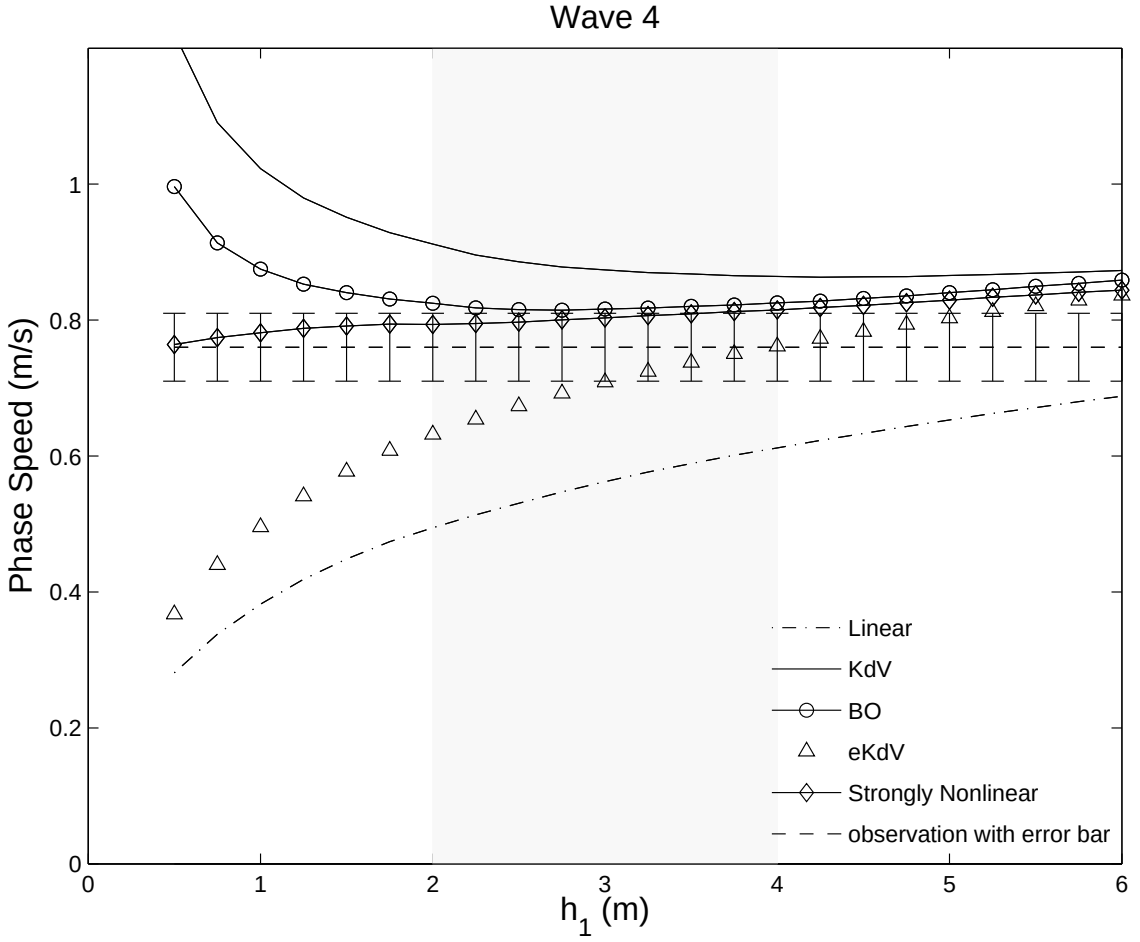

Figure 3.8: Phase speeds for wave 4 observed on June 26, 2002 around Point Roberts are estimated by linear, KdV, eKdV, BO, and strongly nonlinear models over a variety of upper layer depths between $0.5 - 6$ m and a fixed total water depth of 120 m. The shaded area again shows the reasonable range of h_1 ([2 4] m). In this study, the wave amplitude is fixed at the observed value.

Similar model fitting was applied to other cases of Table 3.1 on May 24, June 7, June 10, June 25, and July 15. The fitting results vary from case to case and will be discussed in the following section.

3.1.2 Summary and Discussion

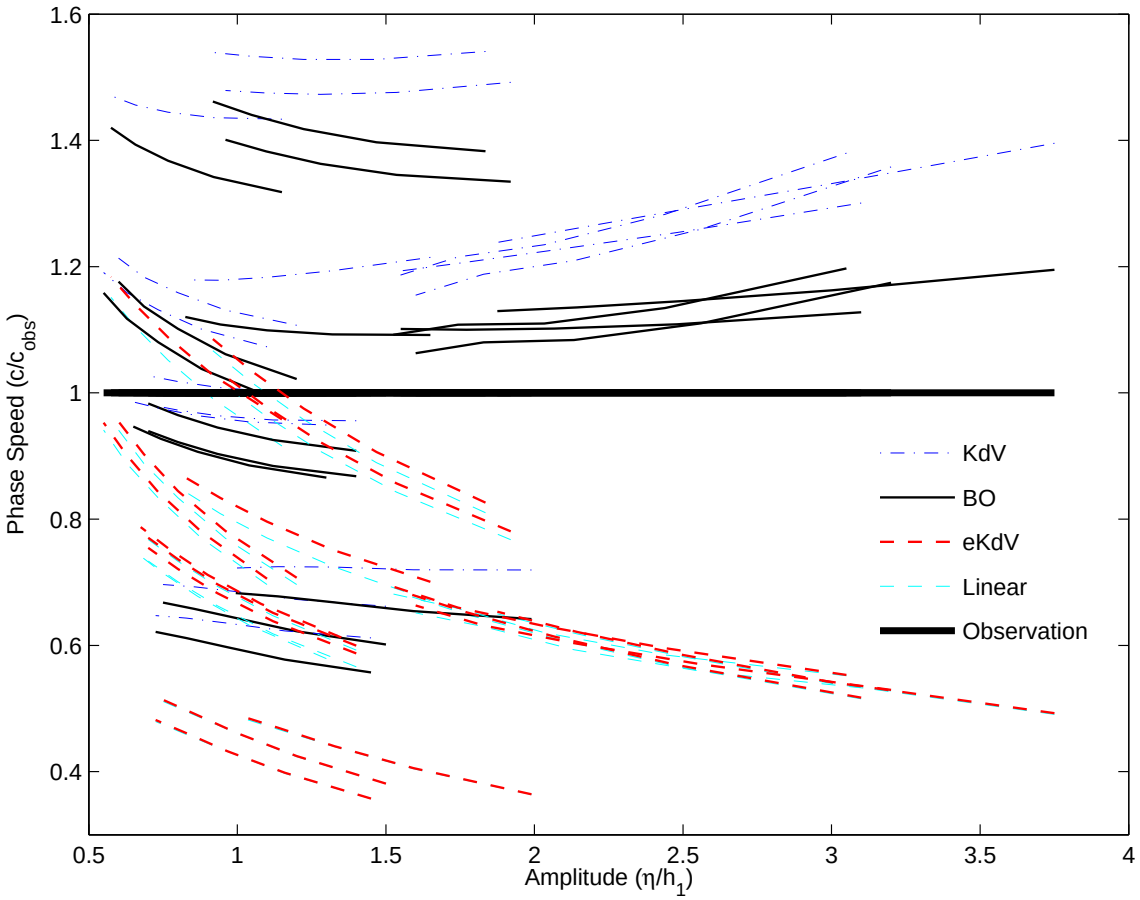

Figure 3.9: This figure compares wave speeds predicted by theories (KdV, BO, eKdV, linear) with observed values. For each wave case, the wave amplitude is fixed as the observed value for that wave and the upper layer depth h_1 varied between 2m and 4m. The vertical axis is model predicted phase speed normalized by the corresponding observed wave phase speeds c/c_{obs}. The horizontal axis is the normalized wave amplitudes. The data points appear to be horizontally distributed and this suggests that the comparison is not very sensitive to depth change. If the observed and predicted speeds match, the data point of that case should be on the line of $c/c_{obs} = 1$. The point of this figure is to show if the normalized wave speed predictions are close to 1 for different models.

In order to summarize all the cases (linear, KdV, BO, eKdV, and strongly nonlinear), results are shown in a different way. In Figure 3.9, the horizontal axis is the wave amplitude non-dimensionalized by dividing by the (varying) upper layer depth and the vertical axis is the predicted wave phase speed non-dimensionalized by the corresponding observed wave

phase speeds. Ideally we could have $c/c_{obs} = 1$ for some η/h_1. The upper layer depth h_1 varies between 2 m and 4 m. Although the detailed stratifications are different from case to case, [2 4] m would still be a reasonable range for the upper layer depth for the whole summer in the strait. With the same wave amplitude and stratification, for all the studied cases, the BO equation predicts wave phase speeds lower than the KdV phase speed and higher than linear speeds. For some cases, BO estimated speeds are higher than observations and for the other cases they are lower than observations. This is also true for the KdV equation predictions. The majority of KdV predictions are higher than observations. The majority of linear and eKdV predictions are lower than observations. Only BO predictions appear to more evenly spread around observations, which suggests that BO equation provides better predictions of observations than KdV, eKdV, and linear equations, but still not accurate enough even with tuning of the upper layer depth.

The fitting results are not exactly the same between different cases quantitatively, but some qualitative conclusions can be made. First of all, at this stage, none of the two-layer model equations can be chosen with confidence to predict the propagation of the studied waves. Second, for all the studied cases, the BO equation predictions are very similar to strongly nonlinear equation and ILW equation predictions. Third, the predictions by the linear equation are much lower than the nonlinear predictions. Fourth, the predicted values using the eKdV equation are generally located between the linear predictions and nonlinear predictions, especially when the upper layer depth h_1 is small, which is the situation in the Strait of Georgia. Although it is not clear which of the KdV, ILW, BO, and strongly nonlinear equations best describes the propagation speeds of the studied waves, it is rather obvious that the linear and the eKdV predictions are generally lower than the observed values. Therefore, the linear equation and the eKdV equation will not be considered further.

3.2 Two-layer Model Equations with Shear

As different length scales and various nonlinear effects do not improve comparisons, we now examine the effects of shear. Shear profiles for all cases, obtained from ADCP data, are shown in Figure 3.10. These profiles represent the baroclinic currents in the direction of wave propagation. If the current at the surface is in the same direction as the wave propagation direction, it is positive (refer to Figure 3.10). Currents with surface values opposite to wave propagation are then negative. In general, the baroclinic currents are large near the surface and relatively small below 30 m. The baroclinic currents near the surface are either positive or negative. The maximum magnitude of shear currents is less than 0.5 m s^{-1}, and usually less than 0.2 m s^{-1}, which implies that they are smaller than wave propagation speeds. Thus the complicating issue of critical layers (Baines, 1995) does not arise here.

3.2.1 Two-layer Linear Equation with Shear

We begin with an analysis of linear equations before considering the more complicated nonlinear wave equations. Again, for the waves we are studying, bottom topography is not an important factor to consider since the observed waves and shear currents are both located in the thin upper layer which is far from the bottom.

In the fluid system of Figure 3.1, if we consider small-amplitude perturbations and rigid horizontal boundaries above and below, when shear currents are included, the linear wave phase speed c_{shear} is calculated as (Baines, 1995):

$$c_{shear} = \frac{U_1 T_1 + U_2 T_2 + \sqrt{(T_1 + T_2)(\rho_2 - \rho_1)g - T_1 T_2 (U_2 - U_1)^2}}{T_1 + T_2}, \tag{3.42}$$

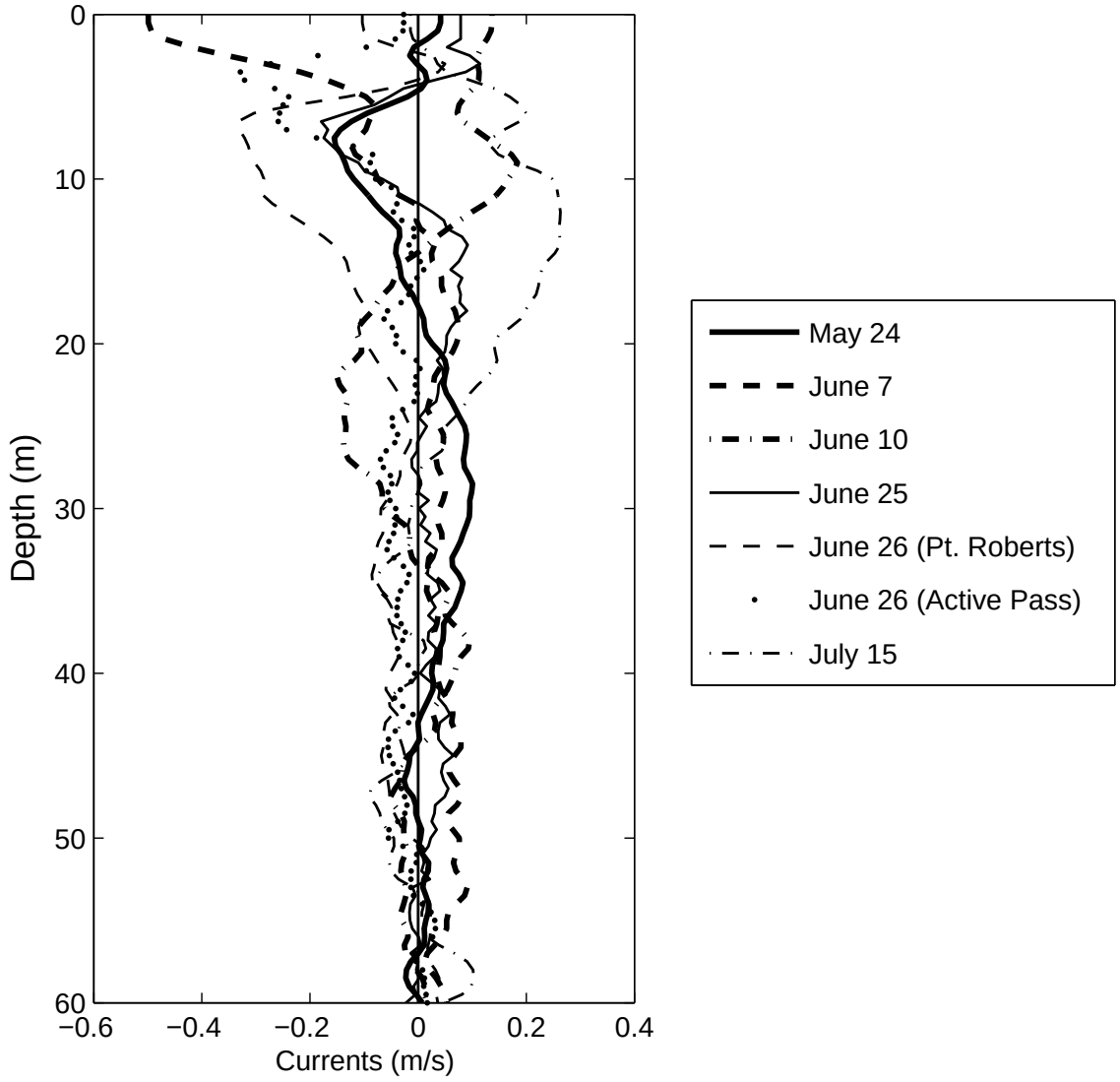

Figure 3.10: The baroclinic currents in the direction of wave propagation for the studied cases of May 24, June 7, June 10, June 25, June 26, and July 15. On June 26, data of currents are available for two locations, one location near Point Roberts and another around Active Pass. Positive currents are in the same direction of wave propagation and negative currents are in the opposite direction of wave propagation. Similar to density stratifications, the baroclinic currents are confined to a shallow layer (near 30 m deep) of water near the water surface. The baroclinic currents below are generally very small and tend to zero as the depth approaches the water bottom. The maximum magnitude of the baroclinic currents is less than 0.5 m s^{-1}.

where

$$T_i = \frac{\rho_i k}{\tanh kh_i}, \tag{3.43}$$

and U_1 and U_2 are the shear velocity in the upper and lower layer, respectively.

For any given wave number k, with sufficiently large $|\Delta U|$=$|U_2 - U_1|$, i.e. when

$$| \Delta U | > \frac{T_1 + T_2}{T_1 T_2}(\rho_2 - \rho_1)g, \tag{3.44}$$

where c_{shear} as calculated from Equation (3.42) is a complex number and the wave will become unstable.

When there is no shear current, $U_1 = U_2 = 0$, the above solution simplifies to

$$c_0 = \sqrt{\frac{(\rho_2 - \rho_1)g}{T_1 + T_2}}. \tag{3.45}$$

In the long wave limit, $kh_i \longrightarrow 0$, $\tanh kh_i \longrightarrow kh_i$, $T_i \longrightarrow \rho_i/h_i$, and Equation 3.45 is reduced to Equation 3.32.

The same sixteen waves as in the previous section are used. The wave phase speed with shear or without shear is calculated by substituting the corresponding values of ρ_1, ρ_2, U_1, U_2, h_1, and h_2 into the above Equations (3.42 - 3.45) with wave number k specified. ρ_i and U_i (i=1, 2) are the average observed values of density and shear currents in each layer. Note that this particular analysis is more an experiment on Equations (3.42 - 3.45) than on the waves in the Strait of Georgia, although the currents and the density profiles obtained in the Strait of Georgia are used. This analysis is meant to illustrate how differently a shorter wave and a longer wave are affected by shear currents. The upper layer depth h_1 is taken as 5 m. The two studied wave numbers ($k = 0.01$ m^{-1}; $K = 3$ m^{-1}) are specified

rather arbitrarily in the reasonable range of the waves in the Strait of Georgia. $K = 3$ m^{-1} represents a shorter wave case, while $k = 0.01$ m^{-1} represents a longer wave case.

The results for all of the above sixteen cases are summarized in Table 3.2 (see end of this chapter). The second column, $\Delta\rho$, is stratification, i.e. the density difference between the two layers. The third column, ΔU, is the shear strength, which is defined as the difference between the mean currents in the upper and the lower layer. The fourth column, sgn(U_1), is the sign of the mean current in the upper layer, positive when it is in the same direction of wave propagation and negative when it is opposite to wave propagation. The fifth column, sgn$(c_{shear} - c)$, is the sign of the difference between the sheared wave speed and the wave speed without shear. It is positive when the shear current increases wave phase speed and negative when shear current decreases wave speed. The sixth column, $|\Delta c|$, compares the magnitude of the wave phase speed change caused by shear currents to the values when there is no shear current. $|\Delta c|_k$ and $|\Delta c|_K$ are for small and large wave numbers, respectively. The seventh column is the non-dimensionalized value of the sixth column, which measures the shear effect on wave speed relative to its original values without shear currents. The nondimensionization is done by dividing by the predicted phase speed c without shear. The eighth column compares the shear effects on small wave number with those on large wave number in column seven. The ninth column compares the relative magnitudes of the predicted wave phase speed without shear and the observed wave speed. The tenth column is the same as column nine but the predictions include shear effects. The eleventh column shows whether the difference between the phase speed predicted by the related equations and observation is increased or decreased by the inclusion of shear current.

From Table 3.2, we see that 1) shear currents in the upper layer U_1 have the same sign as that of $\Delta U = U_1 - U_2$ (comparing the third and the fourth column) because the lower layer

current U_2 is much weaker than the upper layer current U_1 and also the vertical integral of U is zero; 2) from column three, four, and five, positive upper layer shear current U_1 or positive ΔU increases the linear internal wave phase speeds; 3) for the same stratification $\Delta\rho$, the same shear currents increase the small wave number internal wave phase speeds more than they do the larger wave number waves (column six, seven, and eight); 4) with a fixed wave number, the magnitude of the change of wave phase speed Δc is mainly determined by the magnitude of U_1 or ΔU, the larger the magnitude of ΔU, the larger the magnitude of Δc (column three and six); 5) if we treat the observed waves as linear waves, as shown in column nine, the phase speeds predicted by linear two-layer equation are always smaller than the observed phase speeds; 6) from column eleven, after including shear currents into account, although the difference between prediction and observation is decreased for more (nine) cases than those (six) when difference increased, the linear predictions with shear are still lower than observations in column ten. This short-wave linear two-layer model with shear apparently is not adequate to predict the wave propagation in the Strait of Georgia. Although the inclusion of shear does slightly improve the results, the linear equation is far from being adequate in describing propagation of the waves in the Strait of Georgia.

3.2.2 Two-Layer Nonlinear Model Equations with Shear

The waves observed in the Strait of Georgia have wave-wave spacing greater than 200 m. The horizontal dimension of the waves are much greater than the thin upper layer depth and the observed waves are long waves.

In the long wave limit of Equation (3.42), $kh_i \longrightarrow 0$, $\tanh kh_i \longrightarrow kh_i$, $T_i \longrightarrow \rho_i/h_i$,

and the linear long wave speed with shear current is

$$c_{shear} = \frac{U_1\rho_1 h_2 + U_2\rho_2 h_1}{\rho_1 h_2 + \rho_2 h_1} + \sqrt{-\frac{h_1 h_2 \rho_1 \rho_2 (U_2 - U_1)^2}{(\rho_1 h_2 + \rho_2 h_1)^2} + \frac{h_1 h_2 (\rho_2 - \rho_1) g}{(\rho_1 h_2 + \rho_2 h_1)}}. \tag{3.46}$$

The results of fitting to two-layer wave equations (linear, KdV, BO, strongly nonlinear) with and without shear currents for the same waves, and their comparison with observations are shown in Figure 3.11. The results for waves on the same day are very similar, therefore, only one wave on each day is illustrated. The upper layer depth h_1 varies as in the previous section. The effects of shear currents on wave phase speeds of KdV, BO, and strongly nonlinear waves are essentially similar to that on linear waves in the sense that positive shear currents U_1 or $U_1 - U_2$ increase wave phase speeds while the negative shear currents decrease wave phase speeds. However, it is also clear that none of the two-layer linear, weakly nonlinear or strongly nonlinear models can convincingly predict wave propagation speeds in the Strait of Georgia.

The inclusion of shear currents modified all of the wave solutions. One more fact that draws our attention is that although the solution of the strongly nonlinear equation is different from the weakly nonlinear equation (KdV and BO) solutions, especially when the upper layer is very thin i.e. very strong nonlinearity, the differences between the strongly and weakly nonlinear solutions are comparable with the error bars of wave phase speed calculation associated with digitized photo images. The difference between the strongly nonlinear solution and the BO solution is small for most of the cases especially for those waves on June 7, June 10, June 26 and June 15, while the difference between KdV solution and strongly nonlinear solution is greater.

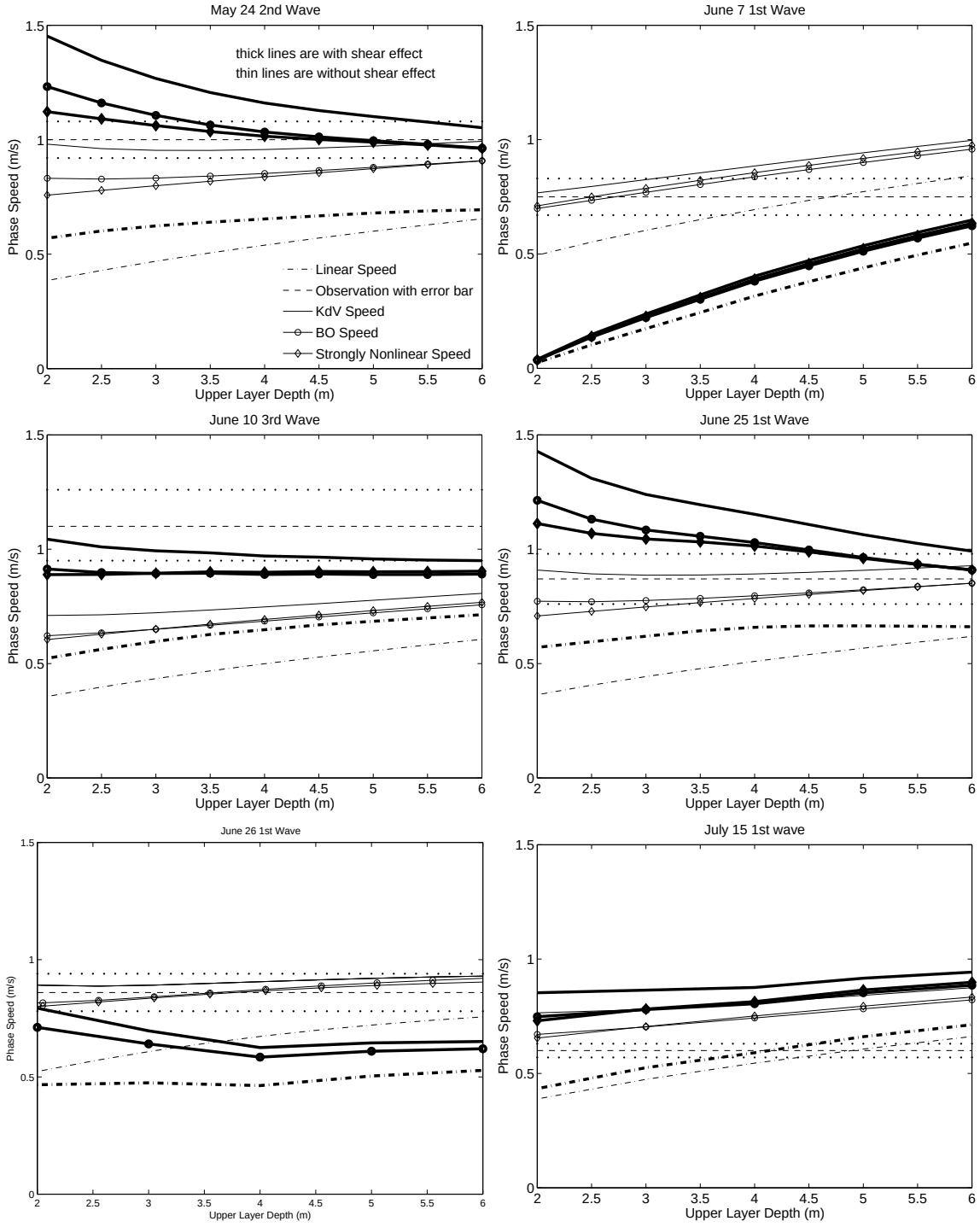

Figure 3.11: The effect of shear current on two-layer long internal waves with varying upper layer depth. All of the six plots share the same legend as in the top left plot. The corresponding thick lines are the results with shear currents for each above mentioned model equation.

3.3 Continuously Stratified Wave Equations with Shear

3.3.1 Continuously Stratified Linear Wave Equation and Shear

The above analysis suggests that although nonlinearities and shear can make an important difference in wave predictions, the two-layer idealization is probably a limiting factor in accuracy. Therefore, continuously stratified equations seem more appropriate than two-layer models. Before continuously stratified nonlinear model equations are applied, we first investigate the shear effect on continuously stratified linear waves modeled with the Taylor-Goldstein (TG) equation (Baines,1995):

$$\frac{d^2}{dz^2}\phi + \left[\frac{N^2}{(U-c_{shear})^2} - \frac{U_{zz}}{U-c_{shear}}\right]\phi - k^2\phi = 0. \tag{3.47}$$

Boundary conditions are:

at $z = 0$,

$$\phi = 0, \tag{3.48}$$

at $z = -D$,

$$\phi = 0, \tag{3.49}$$

where ϕ is mode shape, k is wave number, U is the shear current, c_{shear} is the linear wave phase speed with shear current U, $N = \sqrt{-\frac{g}{\rho}\frac{\partial \rho}{\partial z}}$ is the buoyancy frequency.

The density and shear current profiles of the sixteen waves are applied to the continuously stratified linear wave equation (3.47). This time we compare two cases with wave periods of 10 and 3 minutes instead of giving wave numbers directly. Results are listed in Table 3.3 (see end of this chapter) and summarized as follows: 1) The continuously stratified linear equation predicts wave speeds which are almost always lower than the observed wave

speeds (column five). 2) Positive shear current U_1 or $U_1 - U_2$ increases predicted wave phase speed, while negative shear current decreases wave phase speed (column two and three). 3) For longer internal waves, $|c_{shear} - c|/c$ (column four) is less than that for shorter waves, which means that shear has a proportionally greater effect on shorter waves, similar to the two-layer case. Shorter waves have smaller propagation speeds and hence will be more affected by background currents. 4) The phase speeds predicted by equation (3.47) are not always shifted towards the observed phase speeds by including shear currents (column six), positive shear currents shift predictions towards observations and negative shear current shift prediction away from observations since linear predicted speeds are generally smaller than observations. Although continuous stratification does make an evident difference, the matching to observations of continuous linear wave equations are not remarkably improved from those of two-layer linear wave equations.

3.3.2 Continuously Stratified Nonlinear Wave Equations and Shear

Concluding that continuous stratification and shear current both make a significant difference to phase speeds predicted by linear equations, it is important to re-examine the weakly nonlinear model equations again under continuously stratified and sheared conditions. In a continuously stratified and sheared system, the KdV equation (3.4) and its solution (3.9) still apply, but its coefficients are now dependent on the mode shape (ϕ) and mode speed (c_{shear}) of the linear long wave Taylor-Goldstein (TG) equation (3.47) with wave number $k = 0$.

In solution (3.9) c_0 is replaced by the mode speed c_{shear} of Equation (3.47) and α and

γ are replaced by (Grimshaw, 1998 and Stastna and Lamb, 2002)

$$\alpha = \frac{3}{2}\int_{-D}^{0} \rho_0 (c_{shear} - U)^2 \psi_z^3 dz / I, \tag{3.50}$$

$$\gamma = \frac{1}{2}\int_{-D}^{0} \rho_0 (c_{shear} - U)^2 \psi^2 dz / I, \tag{3.51}$$

where

$$I = \int_{-D}^{0} \rho_0 (c_{shear} - U) \psi_z^2 dz, \tag{3.52}$$

with $\psi = \frac{\phi}{c_{shear} - U}$.

For the BO equation, the solutions (3.28–3.30) are still valid, but the coefficients are to be found differently. Since the internal waves observed in the Strait of Georgia have wave lengths much greater than the depth of the upper thin layer where density stratification and shear currents reside, these internal waves can be treated as long waves inside the upper thin shear layer (with depth h_1). The shear current and density profiles are first extrapolated to $-\infty$ so that the deep water layer has uniform density and zero shear. These extrapolated data are then used in the Taylor-Goldstein equation to get mode shape (ϕ) and mode speed (c_{shear}) (Grimshaw 1998, Tung et al. 1981, Maslowe and Redekopp 1980). The boundary conditions are rigid top and zero derivatives at the virtual boundary at infinity ($\phi_z = 0$ at $z = -\infty$). With this mode shape and mode speed, α is again given by Equations (3.50) and (3.52) with $-D$ now replaced by $-\infty$. The parameter γ is given by $I\gamma = (\rho_0 {c_0}^2 \psi^2)_{z\to\infty}$ according to Grimshaw (1998). The lower boundary is taken to be at -500 m for numerical convenience, changing to -1000 m makes little difference.

Below the shear layer, the wave is not "long" any longer, therefore the term $-k^2\phi$ in the TG equation needs to be considered. Also stratification and currents below the shear

layer will be uniform, which means that the shear and the buoyancy frequency will both be zero. Then the equation for this outside domain will be $\frac{d^2}{dz^2}\phi - k^2\phi = 0$, and the outside region solution has to match with the inside solution of the shear layer. The solution of this outside domain then is $\phi = Ae^{-kz}$, which will need to be normalized so that its maximum is 1 in order to match the wave modes of the inside wave guide domain.

The results of fitting to weakly nonlinear model equations with continuous stratification for studied wave cases with and without shear currents are summarized in Figure 3.12. Three waves, wave 3 (the wave labeled with number 3 in Figure 4.4) in the oblique interaction pattern observed on June 26 and First wave and Second wave in the western packet in the oblique wave-wave interaction observed on July 15, are not included in Figure 3.12 because predictions for them still do not match observations. The reason for this is that these three waves are likely too close to the active interaction center and can not be treated as solitary-like waves. For instance, the wave speed of wave 4 (the wave labeled with number 4 in Figure 4.4) used in this chapter is obtained at a location away from interaction, while the speed obtained for the same wave in the interaction region (the wave labeled by 4i in Figure 4.4) is about 0.2 m s^{-1} slower. In this figure there are four cases on June 26 (red), three on June 10 (blue), two on June 7 (cyan), two on June 25 (purple), and two on May 24 (brown). The results are displayed in six panels, the three panels (a, c, and e) on the left-hand-side compare unsheared equation predictions with observations. Panel a) compares the linear equation predicted wave phase speeds with observed values, panel c) compares the KdV predictions with observations, and panel e) compares between the BO equation predictions and the observed phase speeds. The three panels (b, d, and f) on the right-hand-side show the comparison results between the sheared equation predictions and the corresponding observations. Panel b) is the comparison between the predicted wave

speeds by the sheared linear equation and the observed speeds. Panel d) is between the sheared KdV equation predictions and observations. Panel f) is between the sheared BO predictions and observations. On each panel, there is a black 1:1 line along which predictions equal observations. If a case is above the 1:1 line, the predicted speed is greater than the observed speed, i.e. the equation overestimates observation for this case. Contrarily, the equation underestimates observation for a case below the 1:1 line. The closer a solid circle to the 1:1 line, the better the equation predicted value matches observation for that case. There are no longer any "tunable" parameters like layer depth. Uncertainties in observed propagation speeds are given by horizontal error bars, and in predicted quantities (mostly a function of uncertainty in amplitude) by vertical error bars. By observing all of the six panels in general, the observed wave speeds are between 0.7 m s^{-1} and 1.1 m s^{-1} with error bars less than 0.1 m s^{-1} and the predicted speeds are between 0.6 m s^{-1} and 1.1 m s^{-1} with error bars less than 0.1 m s^{-1} as well. The thirteen cases scatter around the 1:1 line in a wide range (distance to the 1:1 line greater than the error bars) except panel f). By comparing the three panels on the left-hand-side with the three on the right-hand-side, it is also evident shear significantly affects wave speeds. First consider the linear cases in the top two panels a) and b). Before the shear effect is considered, for most cases except two waves on June 7, predictions are smaller than observations. After shear is included, predictions are smaller than observations for all cases. For all of our studied cases, the linear equation with or without shear underestimates the observed propagation speeds with the predicted wave speeds between 0.6 m s^{-1} and 0.9 m s^{-1}. Now consider the two KdV panels (c and d) in the middle. The KdV predicted wave speeds are generally faster than the linear equation predictions with predictions ranging between 0.7 m s^{-1} and 1.0 m s^{-1}. The comparison between predictions and observations are better than the linear cases, but

there is still much scatter. Finally consider the bottom two panels (e and f) for the BO equation. Comparing the sheared BO (f) with the sheared KdV (d), some of the dots are further moved upward and some dots are moved downward since the BO equation predicted phase speeds are different from KdV equation, and moved closer toward the 1:1 line, and such that for most of cases the BO predictions with error bars overlap with the 1:1 line. Without shear, none of the classic models are particularly satisfactory. For most cases, the difference between the predicted values and the observed values are much greater than the error bars. Before shear is included, the matching between the BO equation predictions and observations are not obviously better than the matching between KdV predictions and observations. After shear is included, the matching between the BO equation predictions and observations are greatly improved and the BO predictions are overall closer to observations than KdV predictions. Including shear significantly improves predictions for KdV and BO models in the sense of matching with observations, but only the BO equation can predict wave propagation within the observational uncertainties.

The comparison results of the thirteen wave cases in Figure 3.12 are further confirmed by a χ^2-test between prediction error and observational uncertainty. The χ^2-test compares the sum of squared prediction errors (i.e. predicted minus observed speeds) with the mean variance of the uncertainty (i.e. the mean sum of squares of horizontal and vertical error bars). As the error bars represent the range of uncertainty, which is slightly larger than the standard error, the absolute value of a test statistic is less important than the relative ranking. Our computed test statistic (Table 3.4) is compared with a χ^2 distribution with 12 degrees of freedom, which peaks at a value of about 12. Values larger than 12 suggest an increasing likelihood that we should reject the hypothesis that the observed errors arise only due to statistical variation. One-side p-value gives the probability that the data arises

from this uncertainty. The BO + shear case is completely consistent with this hypothesis, whereas the others are relatively unlikely.

A comparison between the observed wave widths and model predictions are also made. The half wave widths of the observed waves are obtained by the transformation of sounder backscatter and then compared with model predictions. Wave shapes in Figure 3.5 are plotted against time coordinate. With the knowledge of hovercraft speed when crossing against one certain wave, the waves shapes such as in Figure 3.5 a) can be replotted against a distance coordinate. The intuitive idea of transformation between time and distance coordinates is to multiply time by the corresponding hovercraft speed. The actual transformation is complicated by the fact that the hovercraft may cross the wave with an angle to the direction of wave propagation and also the speed of the hovercraft varies with time. The speed of the hovercraft is first obtained by differentiating hovercraft locations measured by GPS, then projected to wave speed direction with the barotropic tide taken out. The so obtained hovercraft speed is then interpolated to sounder data time and the sum of hovercraft speed and wave speed (hovercraft crosses against wave) is integrated to obtain distance of the hovercraft while traveling across solitary waves. One example of the sounder observed wave shape for a wave in the single wave packet on June 26 is as shown in Figure 3.13. The width of this wave is approximately 40$\pm$10 m.

The half wave width can easily be predicted by model equations such as equation 3.29 for continuously stratified BO model. The comparison between continuously stratified BO model predictions and observations is shown in Figure 3.14. Similar to Figure 3.12, the thirteen solid dots in each plot represent thirteen studied waves (same as Figure 3.12). The horizontal axis is the observed solitary wave half width and the vertical axis is the BO equation predicted half wave width. The diagonal line is again the 1:1 line and stands for

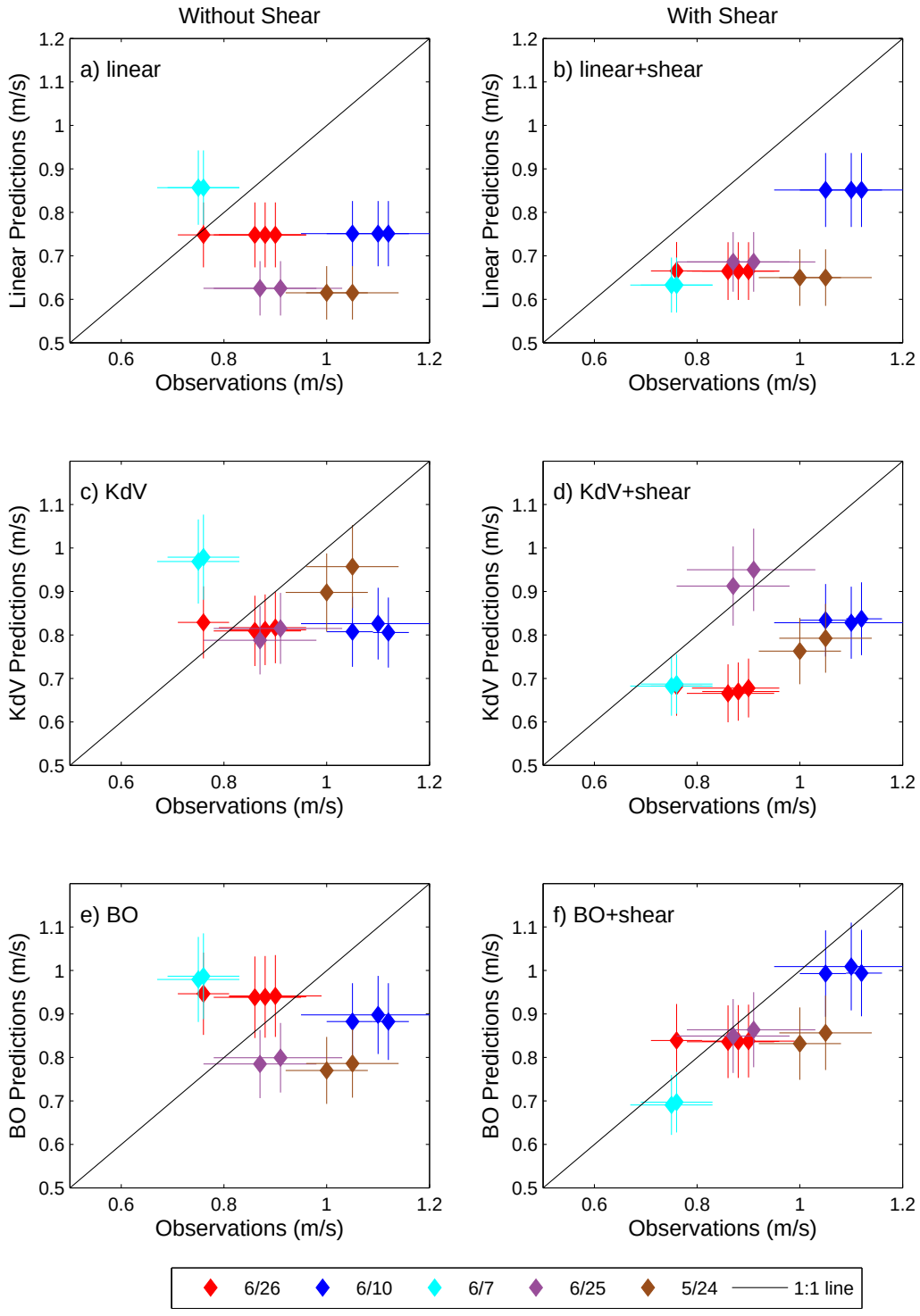

Figure 3.12: The comparison between the observed and predicted wave propagation speeds without and with shear using the continuous models. There are thirteen wave cases from five different days. Each solid dot represents one wave case. The vertical line crossing each dot is the error bar due to wave amplitude estimation. The horizontal line is the error bar coming from wave phase speed estimation. The diagonal line is the 1:1 line. A dot on the 1:1 line means a perfect match between prediction and observation.

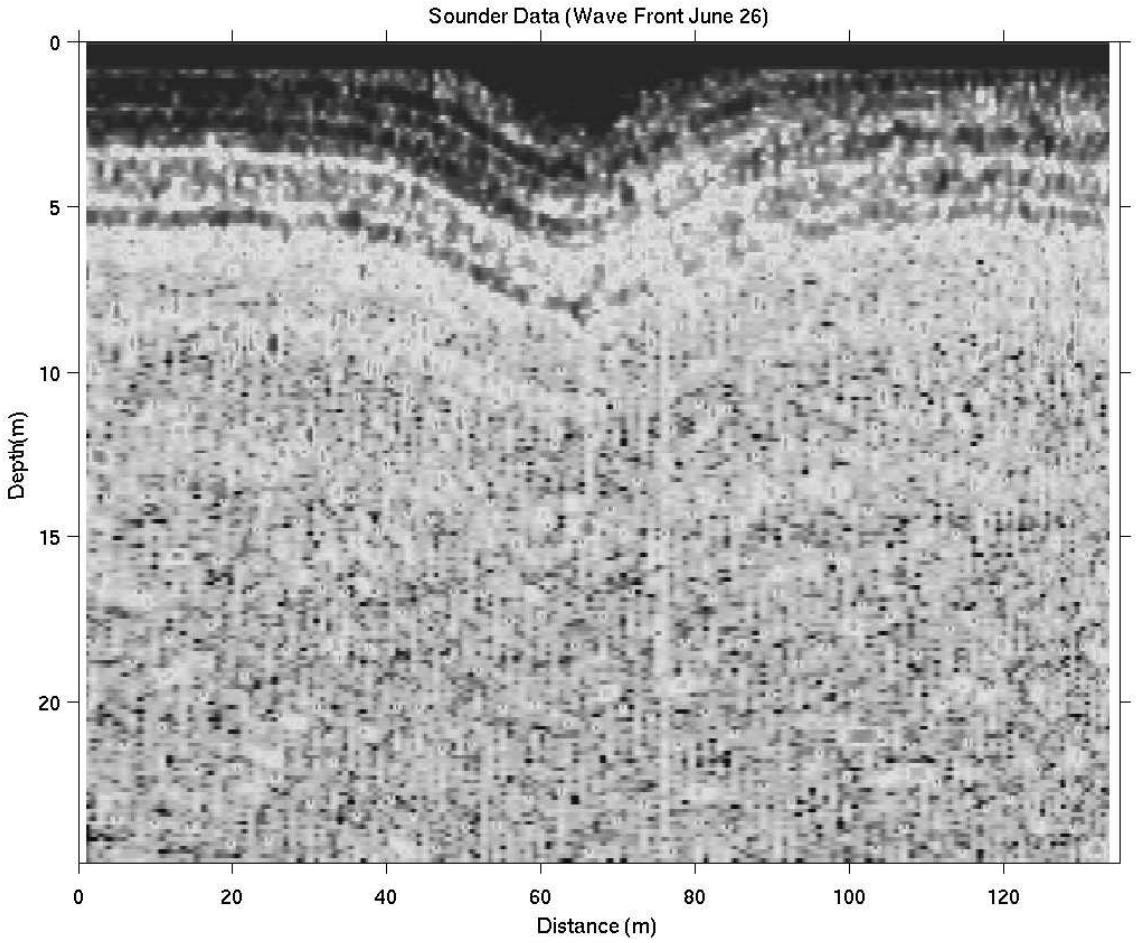

Figure 3.13: The observed shape of the first wave in Figure 3.6 in distance coordinate. From this image, the width 2L of this wave can be estimated to be about 40±10 m.

a perfect match between prediction and observation. The horizontal error bar is associated with estimating wave width from sounder data (e.g. Figure 3.13). The vertical error bar is due to the uncertainty of wave amplitude estimation which is used to calculate half soliton width L by equation 3.29. From Figure 3.14, it is obvious that the matching between prediction and observation is far from satisfactory. Most of the observed half solitary wave widths are in the range of [10 80] m, while the predicted half widths fall in the range of [10 40] m.

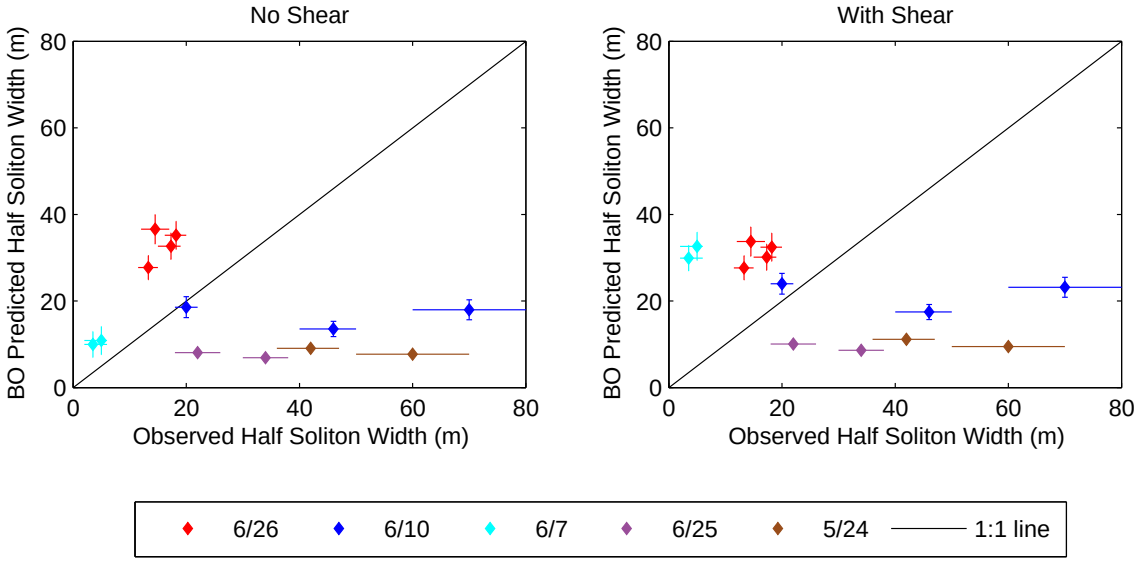

Figure 3.14: The comparison between the continuously stratified BO equation (without and with shear current) predicted half wave width and the observed half wave width. Please refer to the text for details of this figure.

3.4 Summary and Discussion

The shear effect is very evident in all of the studied cases for all the equation predictions. If the surface current is in the same direction as the wave propagation, the predicted phase speeds in all situations are increased, and when the upper layer shear is negative, they are all decreased. A deep water weakly nonlinear equation (BO) with shear adequately models

the observed wave phase speed even though the amplitude is far from small. Both BO and strongly nonlinear results in the two-layer case are similar.

Our situation is somewhat different from Choi (2006) who studied the effect of shear numerically. Choi's model has uniform linear shear slope in both the upper layer and the lower layer, while for our cases, the lower layer is rather quiet with nearly no stratification and zero shear current or shear slope. If we substitute $\Omega_2 = 0$ (zero lower layer shear) or $\Omega_2 \ll \Omega_1$ into Choi's equation (2.9), positive Ω_1 (positive upper layer shear current) will increase the wave propagation speed in the positive x-direction, i.e. the upper layer shear current direction, which is what we expect based on our observations above.

However, the details are important. Even for the same wave equation, such as BO, the two-layer BO predicted wave speed does not get as close to the observed speed as the continuously stratified BO prediction. The fact that continuously stratified equations predict better wave properties than two-layer ones was also discovered by Gan and Ingram (1992) when comparing field observations with theoretical predictions of KdV model. Continuous KdV predictions were even closer to observations than a two-layer KdV with higher order nonlinear and dispersive terms. It seems likely that in order to predict wave propagation in the ocean, it is important to use models with continuous stratifications, unless for some particular ocean the actual stratification is very nearly two-layered. Stratification in the Strait of Georgia cannot be treated in this simple way.

Finally, it is perhaps unexpected that the propagation speed of nonlinear internal waves in the Strait of Georgia are reasonably well described by weakly nonlinear deep water theory (with continuous stratification and shear) even though their amplitudes are $O(1)$. However, this conclusion is also supported by a recent numerical analysis. Camassa et al. (2006) compared a strongly nonlinear model with weakly nonlinear KdV and ILW theory in a

two-layer system. In their figures of 14 (a) and 15 (a), when the wave amplitude is about 1 or less, the weakly nonlinear theory is not dramatically different from the fully nonlinear theory or the experimental data collected in Michallet and Barthelemy (1998). Of course the difference between the weakly nonlinear theories and the strongly nonlinear theory and the difference between theories and the experimental data increases with the increase of the wave amplitude and based on their results, if the wave amplitudes in the Strait of Georgia are much greater than 1, we may find that no weakly nonlinear theory is able to describe the waves in the strait. Interestingly, Camassa et al. (2006), like most of other existing literature, found that KdV theory works better than a deep-water configuration (called ILW in their paper) even in deep-water situations.

The comparison between the model predicted half wave width and the observed values are also studied and it turned out that none of the equations can satisfactorily predict the observed wave widths. Actually, if we recall Figure 1.2, the fact that wave shape is hard to be predicted by any of the classic models was also found by Koop and Butler (1981) by tank experiments.

(1)	(2)	(3)	(4)	(5)	(6)	(7)	(8)	(9)	(10)	(11)
Cases Studied	$\Delta\rho$	$\Delta\ U$	sgn(U_1)	sgn(Δc)	$\lvert\Delta c\rvert_k$ $\lvert\Delta c\rvert_K$	$\lvert\frac{\Delta c}{c}\rvert_k$ $\lvert\frac{\Delta c}{c}\rvert_K$	$\frac{(\Delta c/c)_k}{(\Delta c/c)_K}$	sgn(c-c_{obs})	sgn(c_{shear}-c_{obs})	$\frac{\lvert c_{shear}-c_{obs}\rvert}{\lvert c-c_{obs}\rvert}$
5/24 Second wave	8.7	0.05	+	+	[0.045 0.02]	[0.07 0.16]	< 1	-	-	< 1
5/24 Third wave	8.7	0.05	+	+	[0.045 0.02]	[0.07 0.16]	< 1	-	-	< 1
6/7 First wave	13	-0.37	-	-	[0.34 0.25]	[0.45 1]	< 1	-	-	> 1
6/7 Second wave	13	-0.37	-	-	[0.34 0.25]	[0.45 1]	< 1	-	-	> 1
6/10 First wave	7	0.13	+	+	[0.11 0.04]	[0.2 0.34]	< 1	-	-	< 1
6/10 Second wave	7	0.13	+	+	[0.11 0.04]	[0.2 0.34]	< 1	-	-	< 1
6/10 Third wave	7	0.13	+	+	[0.11 0.04]	[0.2 0.34]	< 1	-	-	< 1
6/25 First wave	7.8	0.07	+	+	[0.06 0.03]	[0.1 0.2]	< 1	-	-	< 1
6/25 Second wave	7.8	0.07	+	+	[0.06 0.03]	[0.1 0.2]	< 1	-	-	< 1
6/26 wave 3	9.8	0.03	+	+	[0.03 0.015]	[0.048 0.1]	< 1	+ (k) or - (K)	-	$> 1(k)$ or < 1 (K)
6/26 wave 4	9.8	-0.18	-	-	[0.16 0.1]	[0.24 0.8]	< 1	-	-	> 1
6/26 First wave	9.8	-0.16	-	-	[0.15 0.1]	[0.22 0.7]	< 1	-	-	> 1
6/26 Second wave	9.8	-0.16	-	-	[0.15 0.1]	[0.22 0.7]	< 1	-	-	> 1
6/26 Third wave	9.8	-0.16	-	-	[0.15 0.1]	[0.22 0.7]	< 1	-	-	> 1
7/15 First wave	8	0.03	+	+	[0.03 0.013]	[0.04 0.11]	< 1	-	-	< 1
7/15 Second wave	8	0.03	+	+	[0.03 0.013]	[0.04 0.11]	< 1	-	-	< 1

Table 3.2: Summary of two-layer short linear wave equation fitting and shear effect study.
1 - upper layer, 2 - lower layer, $h_1 = 5$ m, $D = 120$ m, $\Delta\rho = \rho_2 - \rho_1$ (kg/m^3),$\Delta U = U_1 - U_2$ (m s^{-1}), $\Delta c = c_{shear} - c$ (m s^{-1}), c_{obs} - observed phase speed, c - phase speed predicted by equation without shear current, c_{shear} - phase speed predicted by equation with shear current, U - shear current, k - small wave number (0.01 m^{-1}), K - large wave number (3 m^{-1}).

(1)	(2)	(3)	(4)	(5)	(6)
Cases Studied	sgn(U_1)	sgn(Δc)	$\frac{(\Delta c/c)_T}{(\Delta c/c)_t}$	sgn(c_{shear}-c_{obs})	$\frac{\lvert c_{shear}-c_{obs}\rvert}{\lvert c-c_{obs}\rvert}$
5/24 Second wave	+	+	< 1	-	< 1
5/24 Third wave	+	+	< 1	-	< 1
6/7 First wave	-	-	< 1	-	> 1
6/7 Second wave	-	-	< 1	-	> 1
6/10 First wave	+	+	< 1	-	< 1
6/10 Second wave	+	+	< 1	-	< 1
6/10 Third wave	+	+	< 1	-	< 1
6/25 First wave	+	+	< 1	-	< 1
6/25 Second wave	+	+	< 1	-	< 1
6/26 wave 3	+	+	< 1	+	> 1
6/26 wave 4	-	-	< 1	-	> 1
6/26 First wave	-	-	< 1	-	> 1
6/26 Second wave	-	-	< 1	-	> 1
6/26 Third wave	-	-	< 1	-	> 1
7/15 First wave	+	+	< 1	-	> 1
7/15 Second wave	+	+	< 1	-	> 1

Table 3.3: Summary of continuous linear equation fitting and shear effect study. 1 - upper layer, $\Delta c = c_{shear} - c$, c_{obs} - observed phase speed, c - phase speeds predicted by equation without shear, c_{shear} - phase speeds predicted by equation with shear, U - shear current, T - large wave period (10 min), t - small wave period (3 min).

Classic Model Equation	Statistic	p-value
Linear	124	0.
KdV	45	9e-06
BO	48	2e-06
Linear+shear	102	2e-16
KdV+shear	76	2e-11
BO+shear	18	0.1

Table 3.4: A χ^2-test in order to compare the six studied model equations in predicting wave phase speeds.

Chapter 4

Oblique Internal Solitary Wave-Wave Interaction

As discussed in Chapter 1, the oblique interactions of solitons are poorly studied, and yet such interactions can often be seen even on flat beaches as surface waves run up onto the shore. Experience in the Strait of Georgia also suggests they are widespread in internal waves, but to my knowledge there have been no geophysical studies of the phenomenon.

When two waves of finite amplitude cross, an interaction can occur. This is different from the case of linear waves, which superimpose without affecting each other. In this chapter, we will study a few observed wave-wave interaction patterns in the Strait of Georgia.

A careful study of the literature suggests that wave interaction patterns for finite but small amplitude waves can be categorized into seven types, which are illustrated in the cartoons of Figure 4.1. An important parameter is the interaction radian angle ψ, defined as the angle between the two wave normals, i.e. between the propagation directions of the interacting waves. When two waves come from exactly opposite directions (case (7) of Figure 4.1), the angle between the two wave normals is 180°, and the interaction is called head-on collision. Both of the interacting waves are shifted backwards. When the interaction angle is between 120° and 180°, the two interacting waves also both shift backward

(case (6) of Figure 4.1). When the angle between the wave normals of the two interacting waves is 120° (case (5)), the two interacting waves experience no phase shift at all. When the two waves interact at a medium angle (less than 120° and much greater than 0° as in case (4)), the two interacting waves both experience forward phase shift. When the interaction angle is small (case (2)), one wave shifts forward and another wave shifts backward. When two waves travel in the same direction (case (1)) while the wave in the back is faster than the wave in the front and it will catch up with the first wave and interact and the wave in the front will shift backward while the wave in the back will shift forward. There is a singular case when two waves interact at a small interaction angle, for which the interaction angle and the two wave amplitudes satisfy a certain relationship. In this case, a third wave (the so-called Mach stem) is generated due to the interaction. This is called Mach interaction (case (3)).

4.1 Theory on Wave-Wave Interaction

Miles (1977 a, b) studied small-amplitude, shallow-water surface wave interactions between KdV waves of similar size and classified the interaction processes of solitary waves into "strong" and "weak", "symmetric" and "asymmetric", "phase-conserving" and "phase-not-conserving", "regular" and "Mach" interactions.

The wave interactions were categorized into "strong" and "weak" according to the length of the interaction time and the magnitude of the resulting phase shift. A strong interaction occurs when the two solitary waves propagate in almost the same direction, interact for a relatively long time and emerge with phase shifts of order $O(1)$. Mathematically, if the dimensionless wave amplitudes of two interacting waves are $\eta'_{1,2}$ and the interaction angle is ψ, then an interaction is strong when $(\frac{\psi}{2})^2 = O(\eta'_{1,2})$. Overtaking is the special case of a

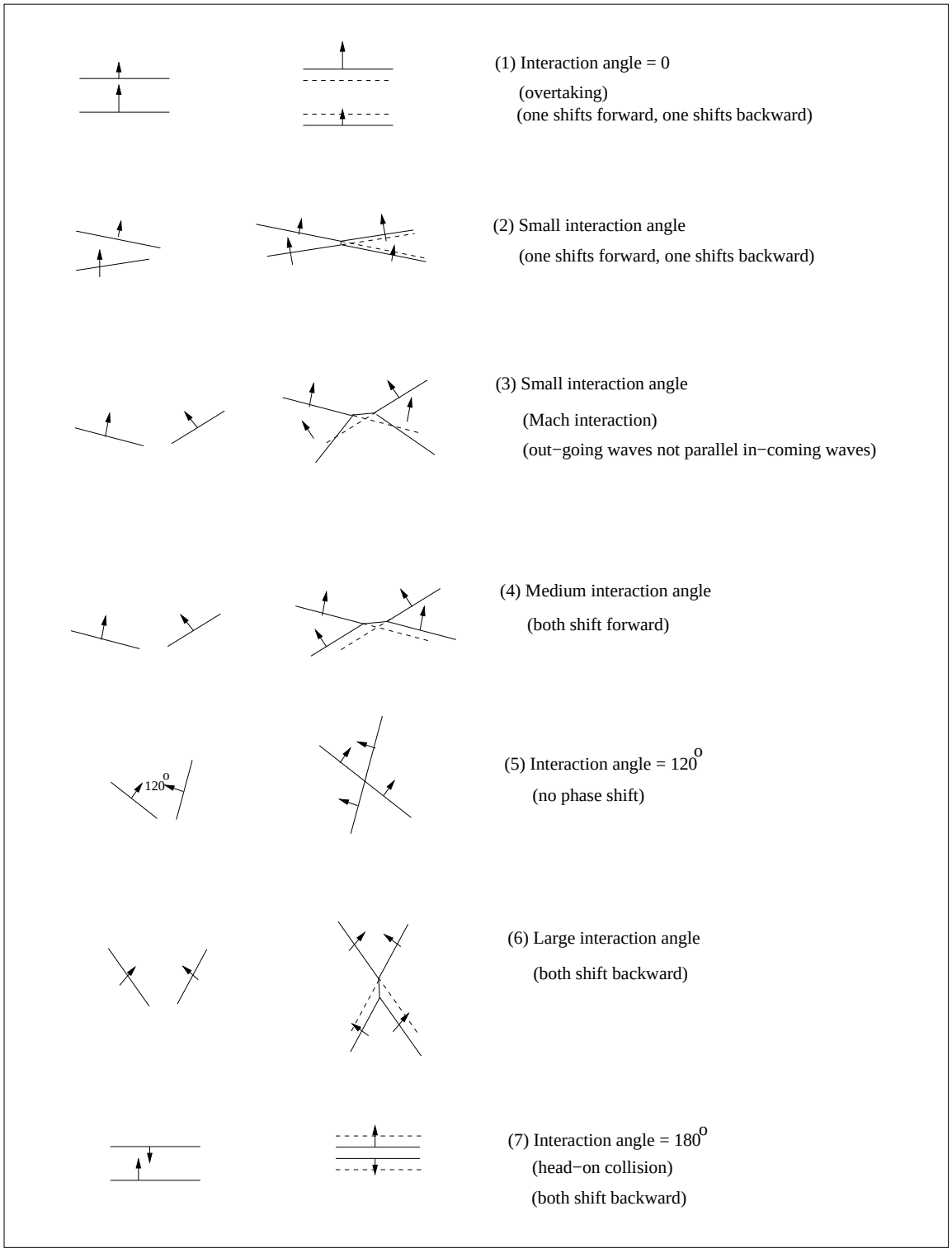

Figure 4.1: Illustration of the phases of small amplitude wave-wave interaction patterns. Solid lines are the wave crests, showing the shifts after the interaction. Dashed lines show phases if there is no interaction. Interaction angle is the angle between the wave normals of the two interacting waves.

strong interaction when the interacting waves are propagating in the same direction (case 1 of Figure 4.1). A weak interaction corresponds to the interaction of solitary waves propagating in very different directions, so that the interaction time is relatively short. Phase shifts are of order $O(\eta_{1,2}^{'})$. A head-on collision is one special case of a weak interaction when the propagation directions of the interacting waves are opposite (case 7 of Figure 4.1). Weak interactions permit superposition of the individual solutions to a first order approximation. Strong interactions are intrinsically nonlinear.

The interaction processes of solitary waves were classified into "symmetric" interactions (i.e. reflections) and "asymmetric" interactions by comparing the wave amplitude difference and the interaction angle. If two waves interact and their amplitude difference is small compared to the interaction angle $|\eta_2^{'} - \eta_1^{'}| < \psi^2$, then their interaction can be treated as reflection to first order. One of the two interacting waves is regarded as the incident wave and the other one as its image. This is a symmetric interaction (Figure 4.2). Otherwise, it is an asymmetric interaction.

Reflection processes in turn can be classified into "regular" and "Mach" reflections. In Mach reflection, the point of intersection of the incident and the reflected waves moves away from the wall at a constant angle, which is called the step angle, and is joined to the wall by a third solitary wave called the Mach stem (refer to the first picture of Figure 4.2). For a regular reflection the wave generated between the original waves and the phase shifted waves due to interaction is called run-up (see the second and the third picture of Figure 4.2). The difference between the two is that the Mach stem grows with time, so the step angle is nonzero and the reflected wave amplitude is smaller than, and the reflected wave angle is larger than that of the incident wave. In regular reflection the incident and reflected wave angles and amplitudes are equal and the run-up does not grow with time.

The critical incident angle ψ_c separating Mach reflection and regular reflection is $(3\eta_i')^{1/2}$, where η_i' is the non-dimensional amplitude of the incident wave. Miles' results on reflections were summarized by Tanaka (1993):

- when $\varepsilon \equiv \frac{\psi}{2}/\sqrt{3\eta_i'} > 1$ (i.e. when incident angle $\psi_c = \frac{\psi}{2} > \sqrt{3\eta_i'}$) it is a regular reflection; otherwise, it is a Mach reflection .
- the step angle ψ_* is 0 for regular reflection; $\sqrt{\frac{1}{3}\eta_i'}\ (1-\varepsilon)$ for Mach reflection.
- the maximum run-up at the wall η_M is $(2+(\frac{3}{2\sin^2\frac{\psi}{2}}-3+2\sin^2\frac{\psi}{2})\eta_i')\eta_i$ for non-grazing regular reflection. The amplitude of Mach stem η_M is $(1+\varepsilon)^2\eta_i$ for Mach reflection.
- the amplitude of the reflected wave η_r equals η_i for regular reflection and $\varepsilon^2\eta_i$ for Mach reflection.
- the angle of reflection ψ_r equals ψ_i for regular reflection and $\sqrt{3\eta_i'}$ for Mach reflection.

When wave amplitudes are unequal the formulas are more complicated. Mach interactions occur when $\psi_- < |\sin^2\frac{\psi}{2}| < \psi_+$ with $\psi_\pm = \frac{3}{4}(\sqrt{\eta_2'} \pm \sqrt{\eta_1'})^2$. Case 3 of Figure 4.1 is a Mach interaction.

An interaction is phase-conserving if the sum of the phases of the incoming waves is equal to the sum of the phases of the out-going waves. The phase shift is defined as δ such that a wave, $\mathrm{sech}^2(\theta)$, after phase shift δ is expressed as $\mathrm{sech}^2(\theta-\delta)$, i.e. a positive phase shift means the wave appears to jump forwards in relation to phase $\theta = k(x-ct)$. Interactions are phase-conserving if the difference in wave amplitudes ($|\eta_2' - \eta_1'|$) is greater than the square of interaction angle (ψ^2) (case 1 and case 2 of Figure 4.1), but not conserved if $|\eta_2' - \eta_1'| < \psi^2$ (case 3, case 4, case 6, and case 7 of Figure 4.1).

If two internal solitary waves interact at a particular angle $\psi = 2\pi/3$ (case 5 of Figure 4.1), each solitary wave exhibits zero phase shift after the interaction (similar to a linear

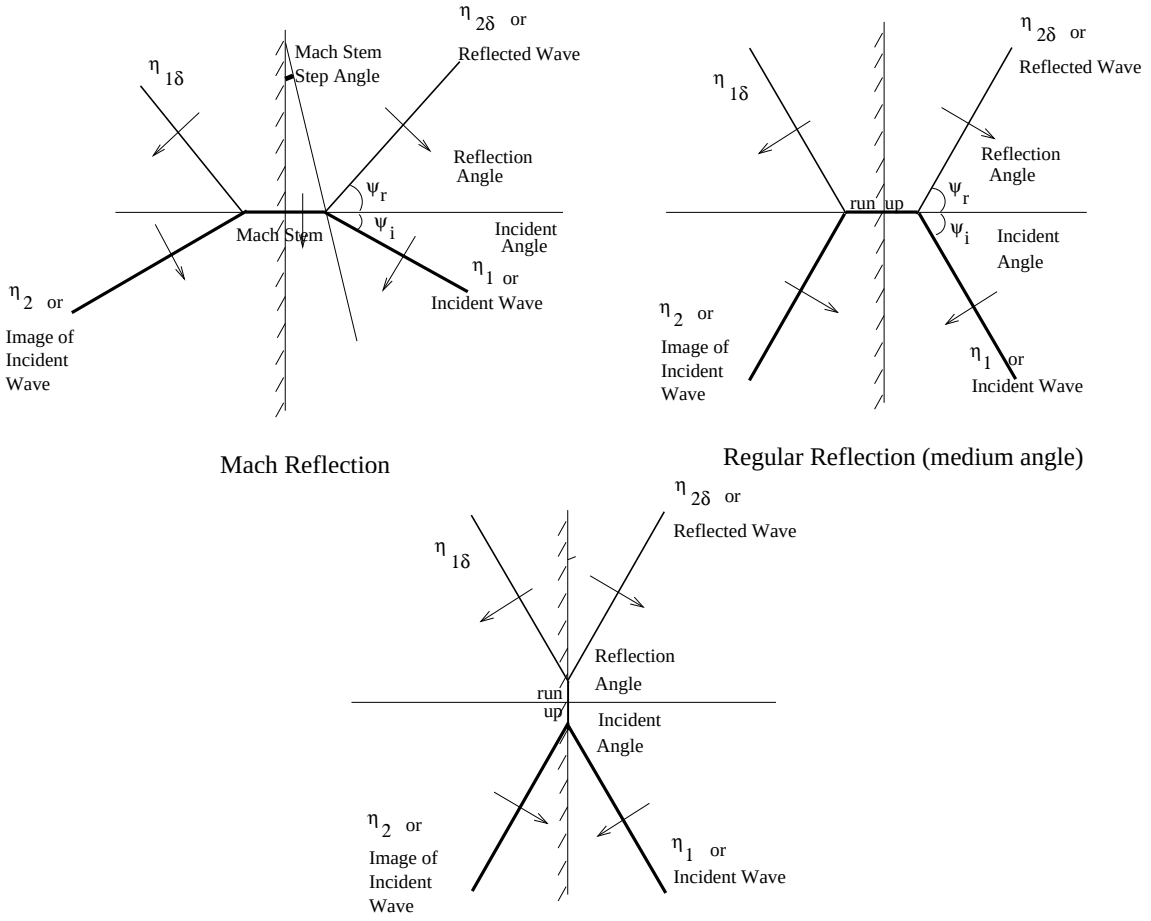

Figure 4.2: Schematic definition of Mach Stem interaction and regular interaction of two waves $\eta_1$and η_2, (η_1, η_2)→($\eta_{1\delta}$, $\eta_{2\delta}$). η_2 ($\eta_{1\delta}$) will be the image of η_1 ($\eta_{2\delta}$) for the reflection case. The top left plot corresponds to case 3 of Figure 4.1. The top right plot corresponds to case 4 of Figure 4.1. The third plot corresponds to case 6 of Figure 4.1. When incident waves are similar a plane of symmetry exists (hatched line), which can be replaced by a solid wall to create a reflection problem.

interaction). This result was found by Matsuno (1998) and Grimshaw and Zhu (1994). At smaller angles both waves shift forward, but at larger angles (case 6, 7) they shift back.

The set of possible interactions in small-amplitude theory is therefore quite wide. In this thesis, two out of the five oblique wave-wave interaction patterns in Figure 4.1 and one interaction pattern possibly different from those in Figure 4.1 are observed in the Strait. Interaction patterns similar to Mach interaction (case 3 in Figure 4.1) were observed on both June 26 and July 15 (Table 2.1). On June 25, a pattern not described by cases in Figure 4.1 was observed. On June 10, the interaction pattern resembles case 2 of Figure 4.1, with a very shallow interaction angle and relatively large amplitude difference. One wave suffered a negative phase shift, another wave experienced a positive phase shift, and the total phase was conserved.

Note that the internal solitary-like waves observed in the Strait of Georgia are neither small amplitude (although they are far from maximal) nor shallow water waves and background shear is present. However, in the preceding chapter, it was showed that some aspects of the propagation of internal solitary-like waves in the Strait of Georgia could be described by weakly nonlinear wave equations and it is possible the same is true for interactions. So, it is reasonable to begin a comparison using existing theory.

There are thus two questions this chapter will address: 1) can the weakly nonlinear theories on internal wave interaction help us to describe the observed internal wave interactions? and 2) do the general behaviors of deep water wave-wave interactions resemble those of shallow water waves?

In order to apply the mathematical theories to the interactions in the Strait of Georgia, we need to first estimate the non-dimensional wave amplitudes, and second measure the interaction angle between two wave normals. At this point we classify the interaction as

weak or strong, decide if the interactions are phase-conserving, and determine whether the interactions are Mach or regular interactions.

The interaction angle is measured on the processed images bearing the appropriate interaction pattern. The wave amplitudes are provided by the water column data. When water column data are not available for certain waves, estimations of wave amplitudes are obtained based on the measurements of propagation speeds.

4.2 Observations

First I am going to discuss the observations and qualitatively classify them according to the cases in Figure 4.1. In section 4.3 I will make more detailed comparisons with theory for some of the cases.

4.2.1 Mach Interaction

First Example of Mach Interaction

A wave-wave interaction (Figure 4.3 and Figure 4.4) was observed near Point Roberts on June 26, 2002 and will be studied first as an example to provide more details of our wave-wave interaction analysis. For the other case studies, some of the details will not be repeated.

Ten photo images taken between 15:20 and 15:50 bearing the same interaction pattern as shown in Figure 4.4 are used for the study of this internal wave interaction. In this chapter's discussion, the three wave packets in all of the photo images are named by their geographical positions on the map as the western packet, the eastern packet, and the merged packet. The western packet stands for the wave packet on the western side (left side) of the three wave pattern, and its wave front is then called the western wave front. The

Figure 4.3: A sample of the original photo images taken on June 26, 2002. On the image is an oblique top view of two internal wave packets interacting obliquely. A third packet resulting from the interaction is also visible. Slicks are spaced about 200 m apart. The red dot at the center left is the hovercraft.

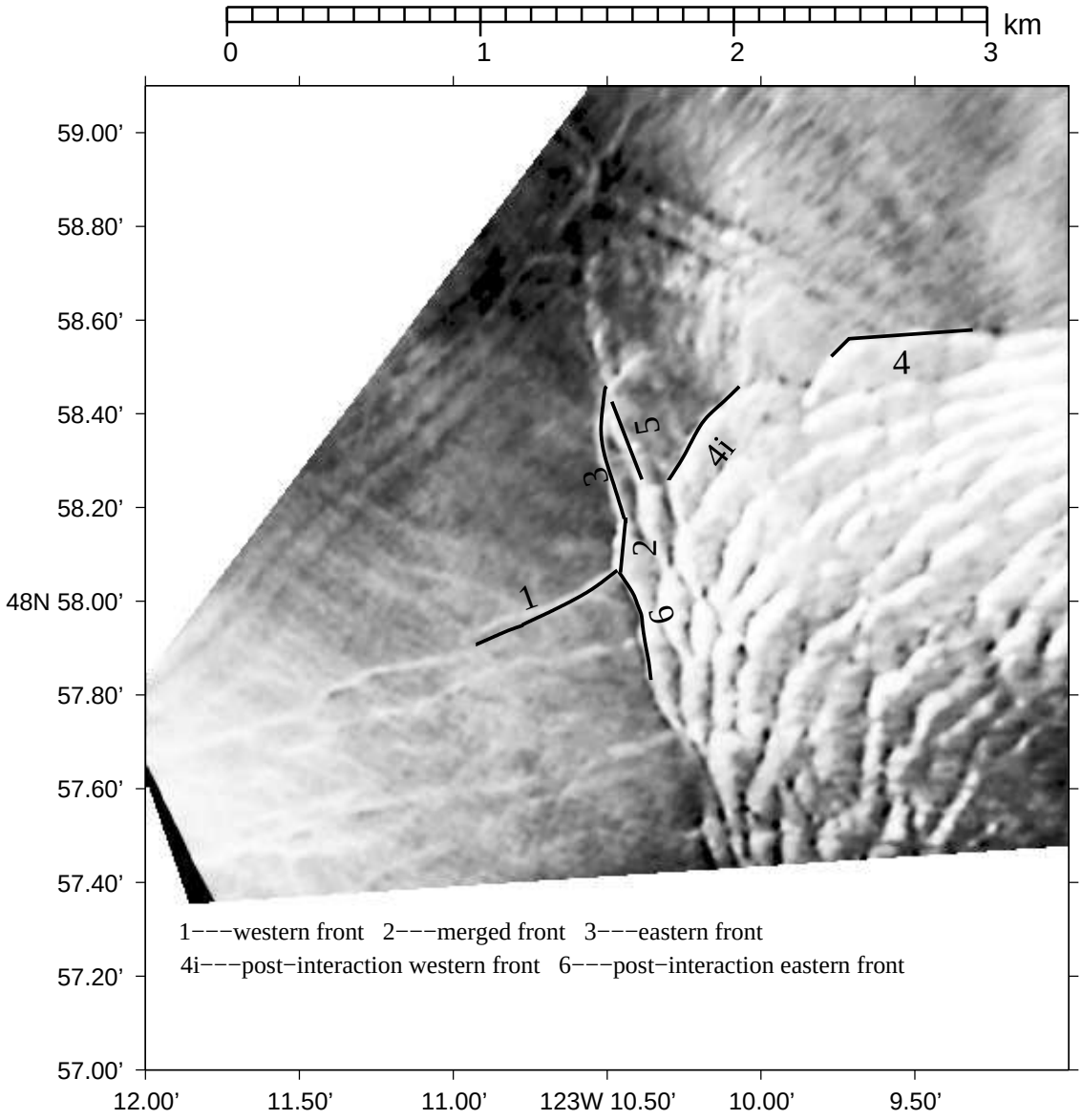

Figure 4.4: A rectified and processed version of the image in Figure 4.3. Labels refer to different waves (see text for details). This image was taken when the aircraft was to the southwest of the observed waves. In the image, there are three wave packets. The wave packet on the left side of the image is propagating to the northwest and its front wave 1 was named as western front. The wave packet with fewer waves (3 and 5) on the north side of the image is propagating to the west. This wave packet is named as eastern packet with 3 being eastern front and 5 being the second wave of this packet. 2 is the merged front of the merged packet. 4i and 6 are post-interaction crests, called post-interaction western front and post-interaction eastern front, respectively. 4 (studied in Chapter 3) is the part of post-interaction western front outside of the intensive interaction region.

eastern packet stands for the wave packet on the eastern side (right side) of the three wave pattern and its wave front is called the eastern wave front. The wave packet generated due to the interaction of the western and eastern packets is located in the middle of the two interacting wave packets and is called the merged packet. The western packet is composed of at least three visible waves, although surface expressions are much more visible after the interactions. The eastern packet has two visible waves. In Figure 4.4, the waves are labeled by numbers for a better presentation of the image. In this chapter, the leading waves of these three wave packets are called the western front (the wave with label 1 in Figure 4.4), the merged front (the wave with label 2 in Figure 4.4), and the eastern front (the wave with label 3 in Figure 4.4). Two waves labeled by 1 and 2 are not included in Table 3.1 but only discussed in text since they are not studied cases in Chapter 3. The waves labeled as 4i and 6 are the post-interaction waves of the western front and the eastern front, respectively. Data of the wave 4 gathered away from interaction was used in single wave studies of Chapter 3. The wave labeled as 5 is the second wave in the eastern packet.

Figure 4.5 is a schematic redrawn of the wave crests in Figure 4.4 in order to better analyze the wave-wave interaction. The western front travels to the northwest in the direction of 60° to the north from west (tidal effects subtracted). The eastern front propagates to the southwest with an angle of 23° south of west. The merged front due to the interaction is traveling to the west and has an angle of 4° to the north of west. The interaction angle between the western front and the eastern front is therefore 83°. The angles between the leading front of the eastern and the western packets and the merged front are measured as 28° and 55°, respectively. The angle between the post-interaction eastern front and the merged front is 40°. The angle between the post-interaction western front and the merged front is not easy to identify because it has also interacted with the second wave of the east-

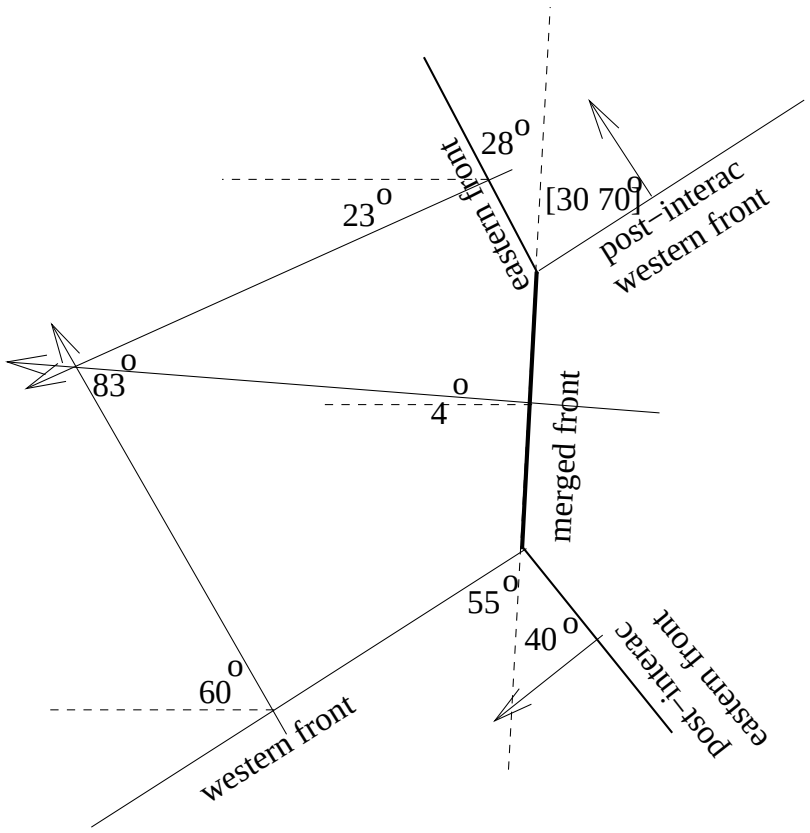

Figure 4.5: A cartoon of the interacting wave fronts and their individual propagation direction for the interaction observed on June 26, 2002. The western front and the eastern front interact and a third wave, the merged front, is generated between them. The merged front travels in between the propagation directions of the two interacting waves.

ern wave packet, but appears to be approximately $(50 \pm 20)°$. Wave crests after interaction are not parallel to their original positions. The post-interaction eastern wave was rotated 12° counter-clockwise. The post-interaction western wave was rotated in the range of [−25° 15°] clockwise.

There are only two waves visible in the eastern packet of this image. The second wave has larger amplitude (3.8 ± 0.3 m) than the leading wave (2.3 ± 0.1 m). Thus it will eventually overtake the leading wave, but over the time period of our observations the collision does not occur. Since we are looking at the interaction over a period of about 30 minutes, it is not unreasonable to assume that the post-interaction western front

is affected mainly by interaction between the western packet and the larger wave of the eastern packet. The amplitude of the post-interaction western front is 3.3 ± 0.3 m. Since the measured phase speed of the western front and the post-interaction western front are similar ($\approx 0.5 \pm 0.1$ m s^{-1}), it is assumed that the amplitude of the western front is also approximately 3.3 ± 0.3 m. These measured values including the angles will allow us to compare with Miles' theory. When applying the formulas, the average values of wave amplitudes are used for simplicity because their uncertainties are small compared with other effects and they do not qualitatively change the comparison results. The amplitudes must be nondimensionalized and this is done by dividing the amplitudes by $h_{eff} = \frac{h_1 h_2}{h_2 - h_1} \approx h_1$ in our situation, with h_1 in the range of [2 4] m. For this case, $\eta_1 = \eta_w = 3.3$ m, $\eta_2 = \eta_e = 3.8$ m, and $\psi = 1.4$ (*i.e.* 83°). Thus we have nondimensional wave amplitudes in the range of $\eta_1^{'} = \eta_w^{'}$=[**0.8** 1.6] and $\eta_2^{'} = \eta_e^{'}$=[**0.9** 1.9]. The amplitudes non-dimensionalized by $h_1 = 4$ m are highlighted with bold characters.

First, the interaction can be viewed as a reflection (i.e. a symmetric interaction) since $|\eta_1' - \eta_2'| < \psi^2$ although in fact it is not quite symmetric geometrically.

Nonlinear oblique interactions between two solitary waves are classified as weak if $\sin^2(\frac{\psi}{2}) \gg O(\eta_{1,2}')$ or strong interactions if $(\frac{\psi}{2})^2 = O(\eta_{1,2}^{'})$. After substituting the measured wave amplitudes and the interaction angle, it is found that this is a strong interaction, and this can be confirmed by the magnitude of the large spatial shifts in wave crests caused by the interaction. As shown in Figure 4.4, the displacements in the direction of wave propagation between the post-interaction western front and the western front, and between the post-interaction eastern front and the eastern front are 100–200 m, comparable to horizontal wave scales. Also, as will be shown later, this interaction lasts for a quite long time (over one hour) while the time scale of the particles moved by the waves is only several

minutes.

A regular interaction becomes Mach interaction when $\psi_- < \sin^2\frac{\psi}{2} < \psi_+$ and $\psi_\pm = \frac{3}{4}(\sqrt{\eta_1'} \pm \sqrt{\eta_2'})^2$. Here, $\psi = 1.4$, $\sin^2\frac{\psi}{2} = 0.4$, ψ_-=[**0.003** 0.006], and ψ_+=[**2.6** 5.3], so it is well within the theoretical Mach interaction regime. For the sake of comparison, if we treat it as a reflection problem and the eastern wave as the incident wave, the critical angle $\psi_i = \psi_c = \sqrt{3\eta_i'}$ has the value of [**1.7** 2.4], i.e. [**97**° 137°]. The post-interaction western front is then the "reflected wave". The observed incident angle is 42° (half of interaction angle) and is smaller than the critical angle, again suggesting Mach reflection. In addition, the crest length of the merged front grows slowly with time and this can be seen from Figure 4.6. The solid line is the least square fit (3.3°) of step angle and the dashed line and the dot-dashed line are the estimated maximum (5.8°) and minimum (0.8°) step angles. Growth in the crest length of the merged front confirms that it is a Mach stem, since regular reflections do not show this behavior. Since there are no direct measurements of the wave amplitudes for Mach stem and the post-interaction waves, these are estimated from wave phase speed observations and a heuristic rule that a larger amplitude wave has faster wave speed than a smaller wave under the same conditions. The observed wave speed of the Mach stem ([0.67 0.86] m s^{-1}) is larger than any of the other waves ([0.43 0.6] m s^{-1} and [0.49 0.6] m s^{-1} for the western front and the eastern front, respectively), therefore, the estimated amplitude for the Mach stem is larger than 3.3 ± 0.3 m. Note that the Mach stem is aligned more with the (larger) eastern wave rather than being exactly symmetric, as would occur in a true reflection case. Ignoring this for the moment, we track the increase in length as a function of distance traveled to find a step angle of $3.3° \pm 2.5°$. The apparent origination time of the Mach stem is also estimated by tracking the length of the stem backward in time (Figure 4.7) and this is found to be around 14:20 ([12:40 15:10]) or about

one hour before our observations. Therefore, we infer that the time length for the full development of the Mach interaction is longer than one hour. This is much longer than the time scale (wave length/wave speed) of the observed waves which is several minutes. The observed long maturing time also agrees with Funakoshi (1980, 1981) that Mach reflection is a much slower process than a regular reflection, and it generally takes a long time for the asymptotic situation to be achieved. Since the stem length increases with time and this is one unique characteristic of a Mach interaction differing from a regular interaction, this observed case is most probably a Mach interaction. However, it is also possible that this growth rate occurs as a transient related to the finite length of crest of real waves. We do not have any further data to address this issue.

Second Example of Mach Interaction

On July 15, 2002, another possible Mach interaction was observed close to Point Roberts between a northward propagating wave packet and a westward propagating wave packet (Figure 4.8). The packet on the right-hand-side or on the northeast is called the eastern wave packet while the other packet on the left or on the southwest is called the western wave packet. The waves in Figure 4.8 are again labeled by numbers. A phase diagram (Figure 4.9) was created based on the image in Figure 4.8. The western front (1 in Figure 4.8) was propagating to the north with an angle of 80° from the east. The eastern front (3 in Figure 4.8) was propagating to the southwest and had an angle of 6° from the west. The merged front (2 in Figure 4.8) was propagating to the northwest with an angle of 35° from the west. The angle between the western front and the merged front is 60°, the angle between the eastern front and the merged front is 37°, the angle between the post-interaction eastern front (5 in Figure 4.8) and the merged front is 42°, the angle between

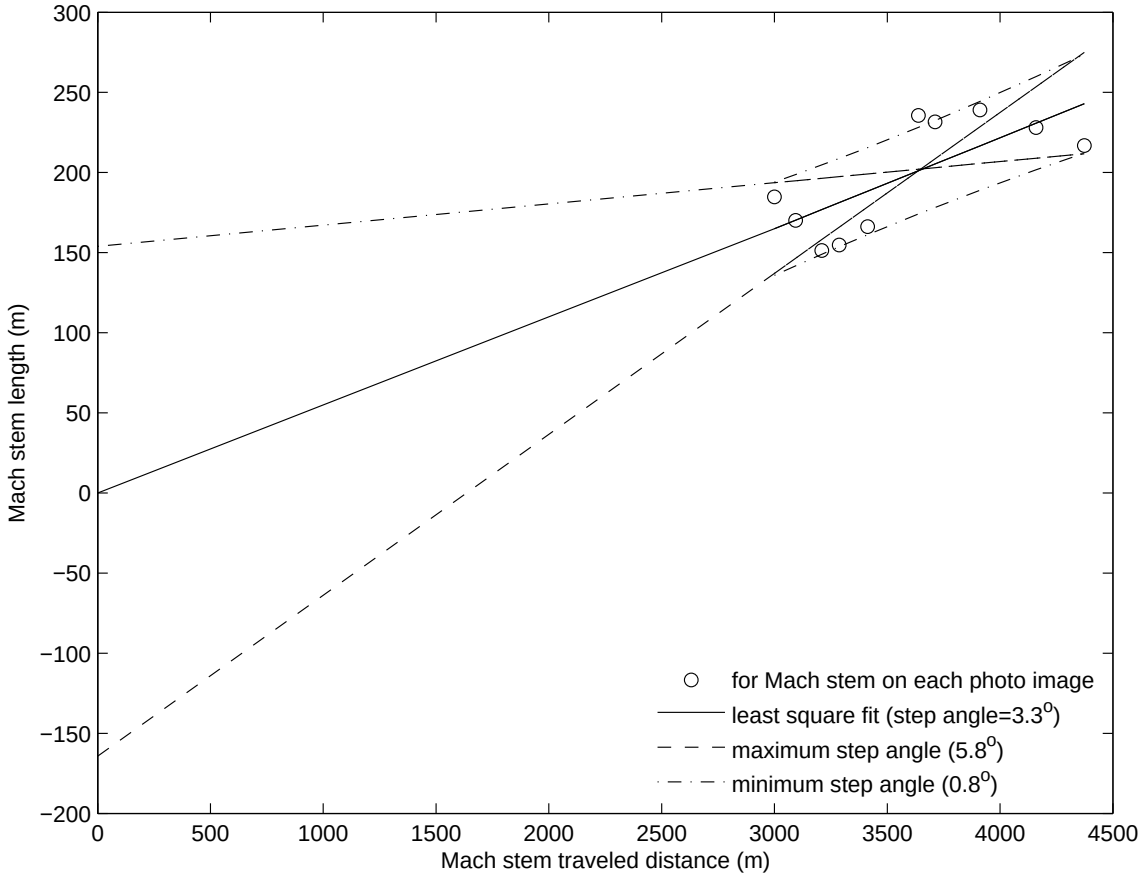

Figure 4.6: The Mach stem step angle is estimated by tracking the crest length of Mach stem (2 in Figure 4.4) on June 26. Each circle stands for the length in one photo image. The horizontal axis is the distance traveled by the Mach stem. The vertical axis is the length of the studied Mach stem. The solid line is the least square fit of the data points and the slope of this line is the best estimate of the Mach stem step angle. The dashed and dot dashed lines represent the maximum and minimum estimates of step angle.

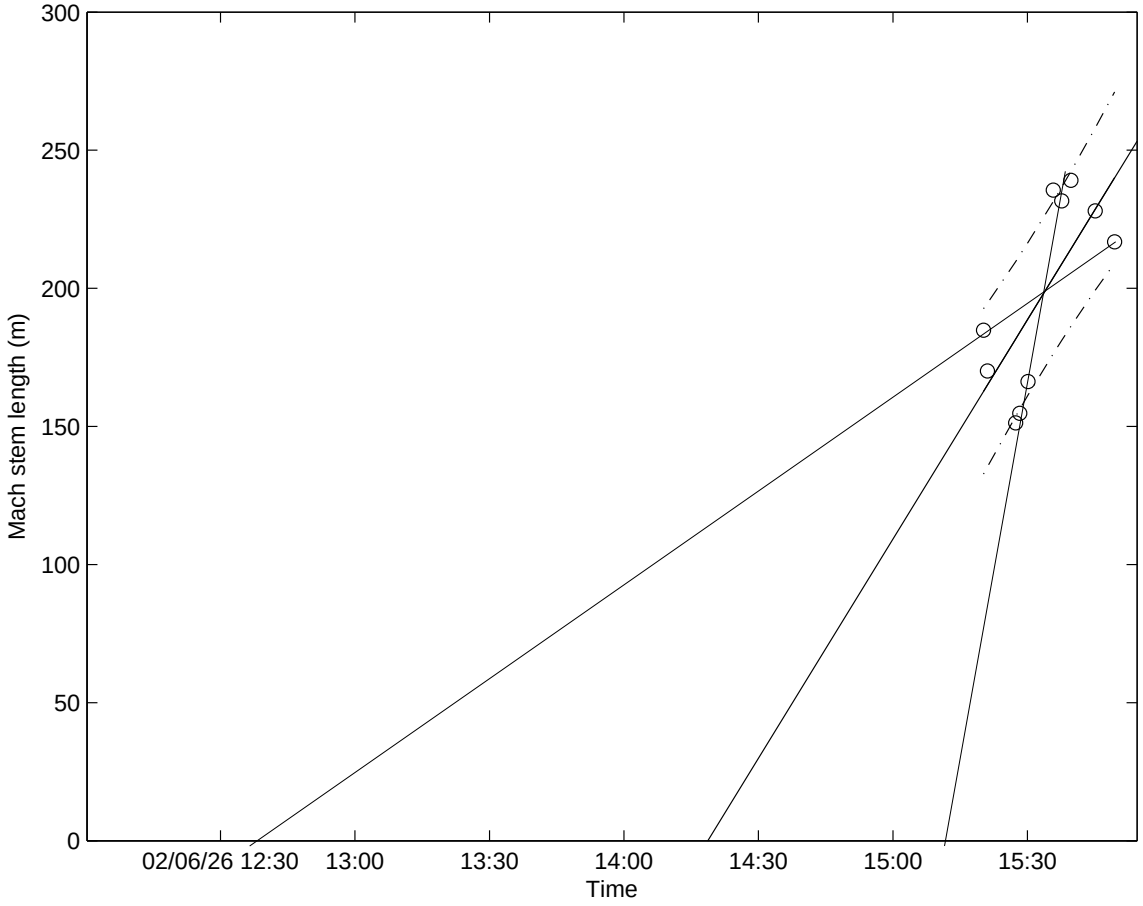

Figure 4.7: The start time of Mach interaction observed on June 26 is estimated by tracking the growth of Mach stem length back to zero. The start time by the least square fit of data slope is 14:20 on June 26. The start time estimated by the minimum and maximum slope fit of data is 12:08 and 15:12 on June 26.

the post-interaction western front (4 in Figure 4.8) and the merged front is 66°. The post-interaction eastern front is rotated 5° relative to eastern front and the post-interaction western front is rotated 6° relative to western front.

The amplitude of the eastern wave front is 4 ± 0.4 m and the amplitude of the western wave front is 3.8 ± 0.4 m. The amplitude of the post-interaction western front is measured with water column data as 3.2 ± 0.2 m. The amplitude of the post-interaction eastern front was not directly measured and its phase speed can not be easily estimated because of difficulties in identifying it in the available photo images. The interaction angle between the two wave normals is $\psi = 1.7$ (98°). The dimensionless amplitudes (relative to the equivalent depth h_{eff} = [2 **4**] m) are η_1' = [**0.95** 1.9] (western front) and η_2' = [**1** 2] (eastern front). The interaction angle ψ gives $\sin^2(\psi/2) = 0.57$, which is less than $O(\eta_{1,2}')$, suggesting it is a strong interaction. $|\eta_2' - \eta_1'| < \psi^2$ (phase-not-conserving) holds and this agrees with the observed forward phase shifts of both of the two interacting waves near the interaction. Again it is not exactly symmetric, even though the amplitudes are similar enough that it can be treated as a reflection. The asymmetry is caused by the difference between the interacting wave amplitudes. For the case observed on July 15, if treated as a reflection problem in order to compare with theory, the eastern wave front is taken as the incident wave and the post-interaction western front as the reflected wave. The incident angle is half of the interaction angle, which is $\psi_i = \frac{\psi}{2} = 49°$ (≈ 0.86) and the incident amplitude is $\eta_i = 4$ m (η_i'=[**1** 2]). The reflected angle ψ_r is again taken as half of the angle between the two post-interaction waves, which is 54°. With our measured angle and amplitude, $\psi_i/(3\eta_i')^{1/2} \leq 1$, i.e. it is a Mach reflection. The speed of the Mach stem is greater than the speed of the western and eastern front. Therefore, the Mach stem's amplitude must be larger than the western and the eastern wave front, i.e. greater than 4 m. The eastern front

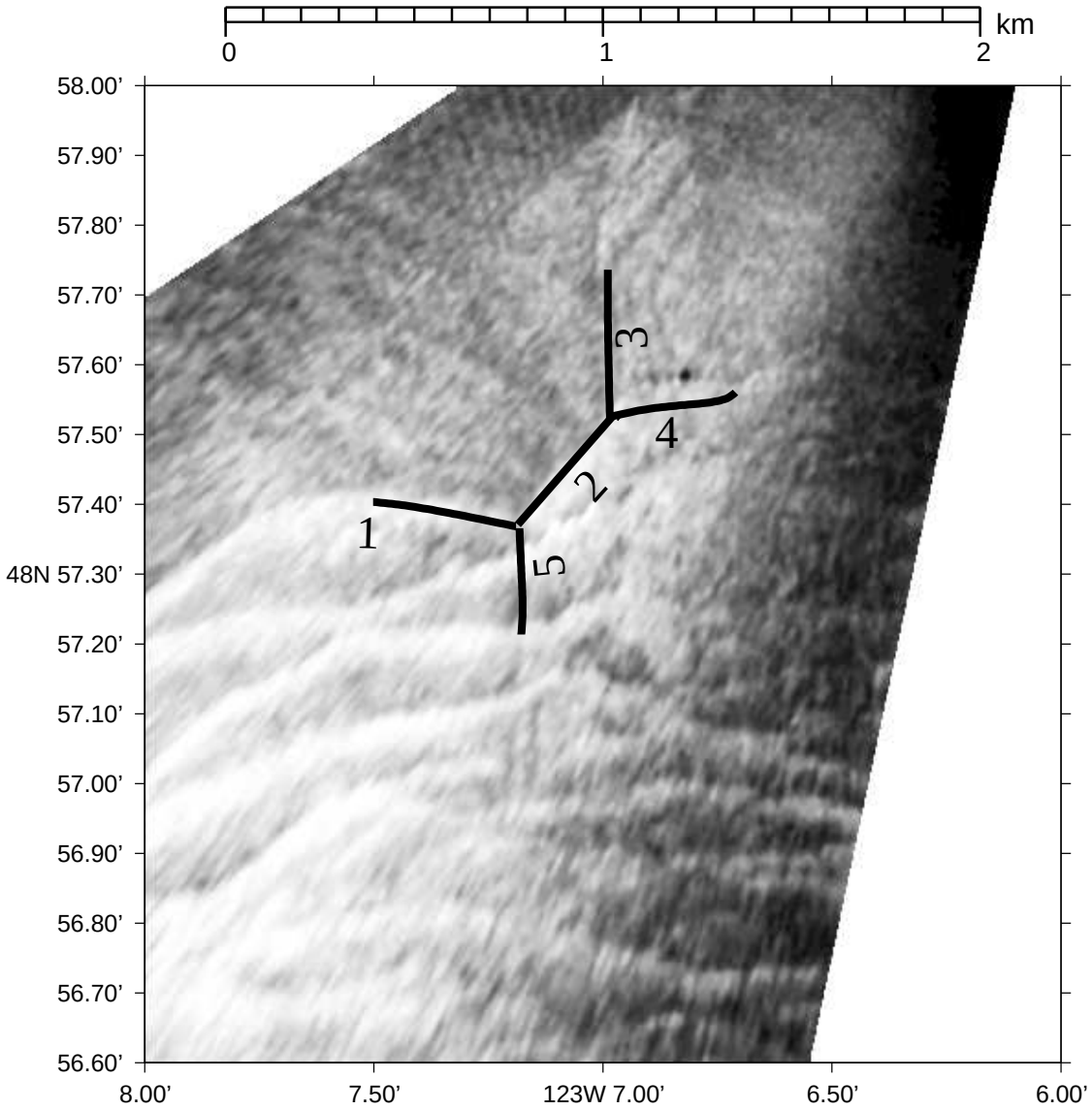

Figure 4.8: Image of the interaction pattern observed on July 15, 2002. This image was taken from the northeast. There are three wave packets observed. The wave packet on the left side of the image was propagating to the northeast, the wave packet on the north side of the image was propagating to the west, and the third wave packet generated due to the interaction of the preceding two wave packets was propagating to the northwest. On the image, the waves are labeled with numbers. 1 – western front, 2 – merged front, 3 – eastern front, 4 – post-interaction western front, 5 – post-interaction eastern front. More details of the waves please refer to the text.

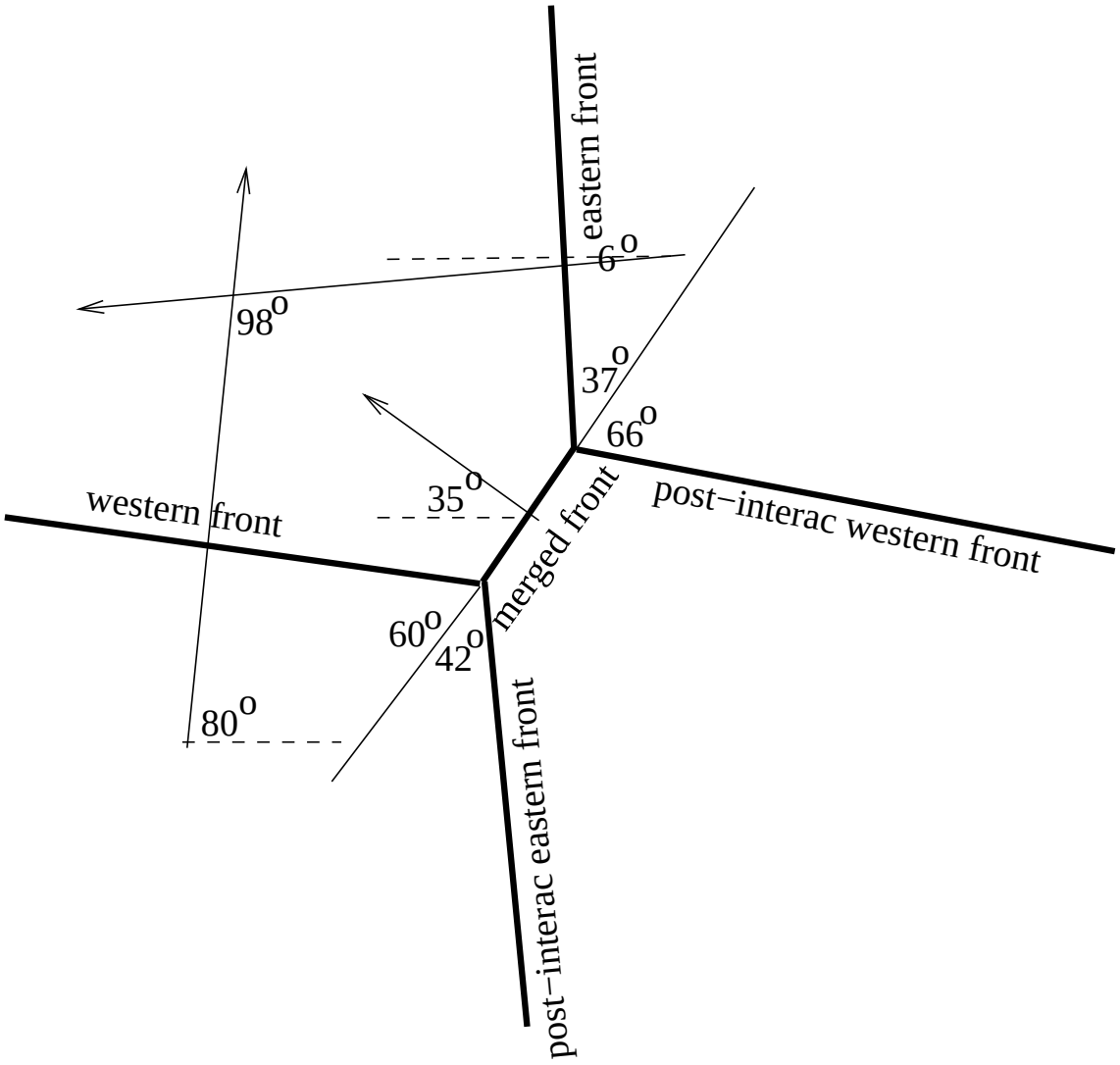

Figure 4.9: The diagram of wave-wave interaction of July 15, 2002 based on Figure 4.8. The western front and the eastern front interact and a third wave, the merged front, is generated between them. The merged front travels in between the propagation directions of the two interacting waves.

has larger amplitude than the western front and experienced smaller phase shift, while the western front with smaller amplitude suffered a larger phase shift, and thus resulted in the observed asymmetry. The Mach stem step angle is estimated to be $10° \pm 5°$. This Mach interaction began at 15:15 ([14:30 15:45]) about one hour before it was observed. Similar to June 26 case, this long interaction time (greater than wave time scale) and the spatial displacements between pre- and post-interaction waves (greater than wave length scale) again indicate the strong interaction nature of this case.

4.2.2 Interaction different from Known Small-Amplitude Interaction Patterns

On June 25, 2002 an interaction pattern that falls in the parameter domain of Mach interaction was observed, but a Mach stem was not seen. The interaction is between a western propagating packet and a northwestern propagating wave packet (Figure 4.10). The hovercraft sampled the second wave of the eastern wave packet instead of the leading front. Hence, this case study will be about the interaction between the western front and the second wave of the eastern packet, the "eastern wave". The observed wave amplitudes are especially large. The eastern wave has an amplitude of 4.6 ± 0.4 m (η_1) and the western wave front has an amplitude of 6 ± 0.3 m (η_2).

As shown in Figure 4.11, the interaction angle between the two wave normals is $\psi = 1.05$ (60°). The dimensionless amplitudes (non-dimensionalized by h_{eff}=[2 **4**]) are $\eta_1' = [\mathbf{1.1}$ 2.3] and $\eta_2' = [\mathbf{1.5}$ 3]. This implies $|\eta_1' - \eta_2'| < \psi^2$, i.e. the phase is not conserved. The satisfaction of this criteria also means that this case can be treated approximately as a reflection problem. It is a strong interaction since $\psi^2 = O(\eta')$. We also have $\frac{3}{4}(\sqrt{\eta_2'} - \sqrt{\eta_1'})^2 < \sin^2(\psi/2) < \frac{3}{4}(\sqrt{\eta_2'} + \sqrt{\eta_1'})^2$, so it is possible that this case is a Mach interaction

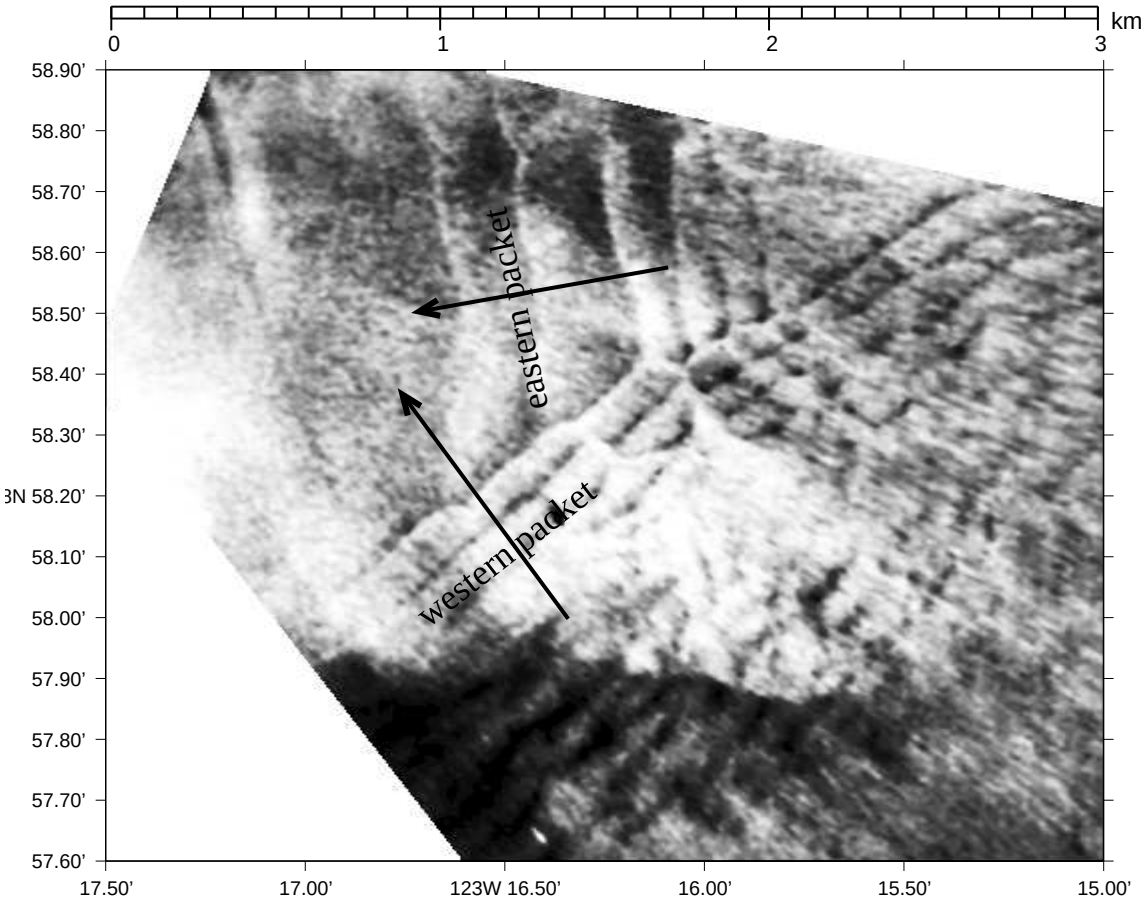

Figure 4.10: The interaction pattern on June 25, 2002.

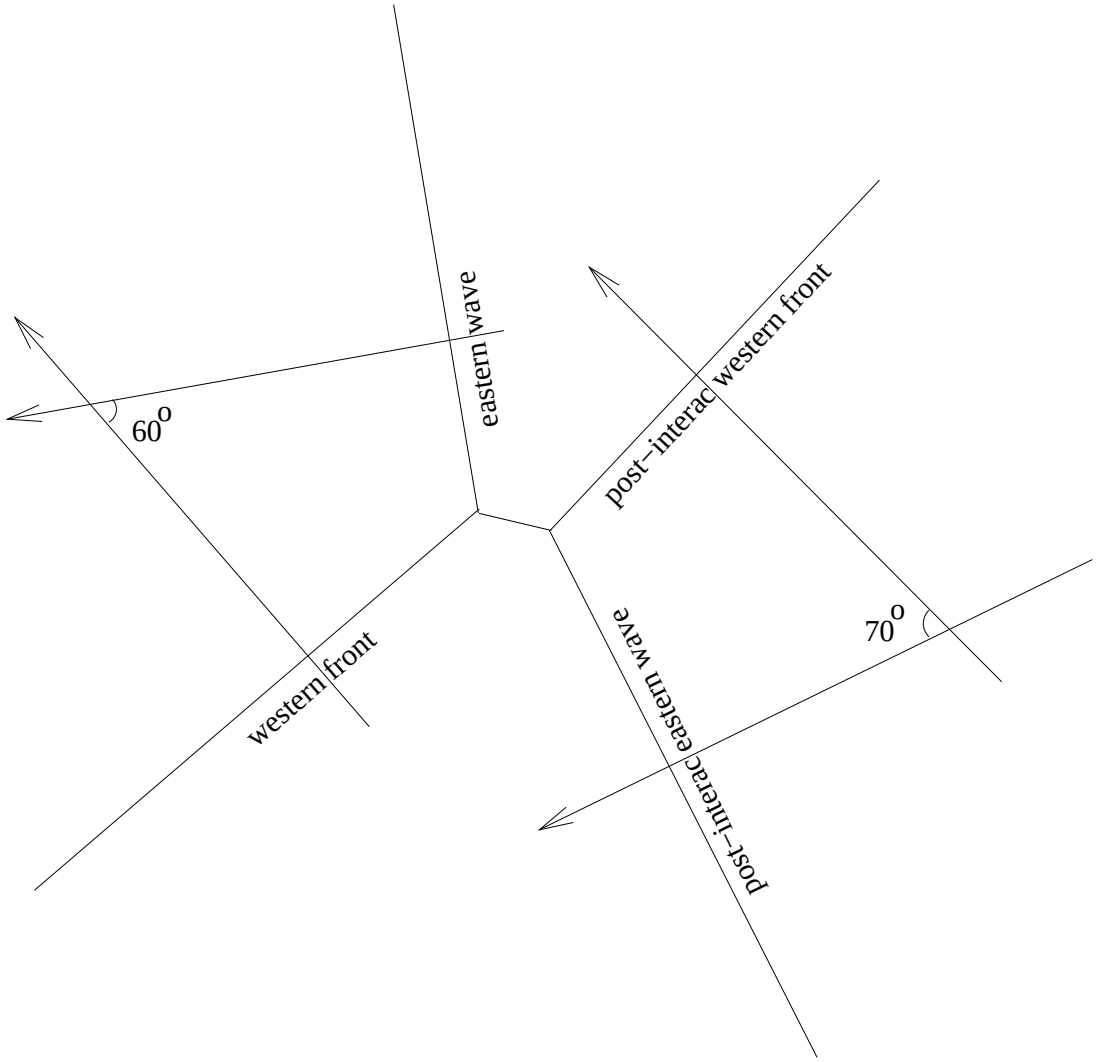

Figure 4.11: Interaction diagram generated based on Figure 4.10. The western front and the eastern wave interact with an interaction angle of 60°. Instead of a Mach stem between two interacting waves, there is a run-up generated behind the joining point of them.

problem. However, the interaction pattern as shown in Figure 4.10 does not resemble a Mach interaction.

4.2.3 Shallow Angle Interaction

Although the previous cases have shown interactions at relatively large angles, the interactions at shallow angles, especially when wave amplitudes differ (case 2 in Figure 4.1), are interesting because they are very similar to (well known) 1-D interactions. One aspect of 1-D interactions is that the two wave crests may seemingly never merge. Instead the surface height field has the appearance of one crest "pushing away" the other. On June 10, this kind of pattern (Figure 4.12) was observed.

Our water column data suggests the two waves have a length scale of about 150 m and the distance between two troughs of the same wave is about 260 m. The closest approach of the crests is about 160 m (Figure 4.14) which would suggest some interaction is occurring. This appears to be an oblique wave-wave interaction with a very small interaction angle (case 2 in Figure 4.1). A cartoon of this interaction is shown in Figure 4.13. The waves are named as the first wave, second wave, post-interaction first wave, and post-interaction second wave.

The water column data can only provide the amplitudes of the post-interaction second wave (3 ± 0.2 m) and the first wave (2.9 ± 0.3 m). Assuming that the second wave does not experience significant modifications to its wave properties, especially amplitude, during this interaction this value is used for the pre-interaction second wave as well.

As in the cartoon of this interaction (Figure 4.13), the interaction angle between the two wave normals is ψ=10° (0.18). The non-dimensional wave amplitudes are $\eta_1' = 2.9/h_{eff}$=[**0.73** 1.45] for the second wave and $\eta_2' = 3.0/h_{eff}$=[**0.75** 1.5] for the first wave

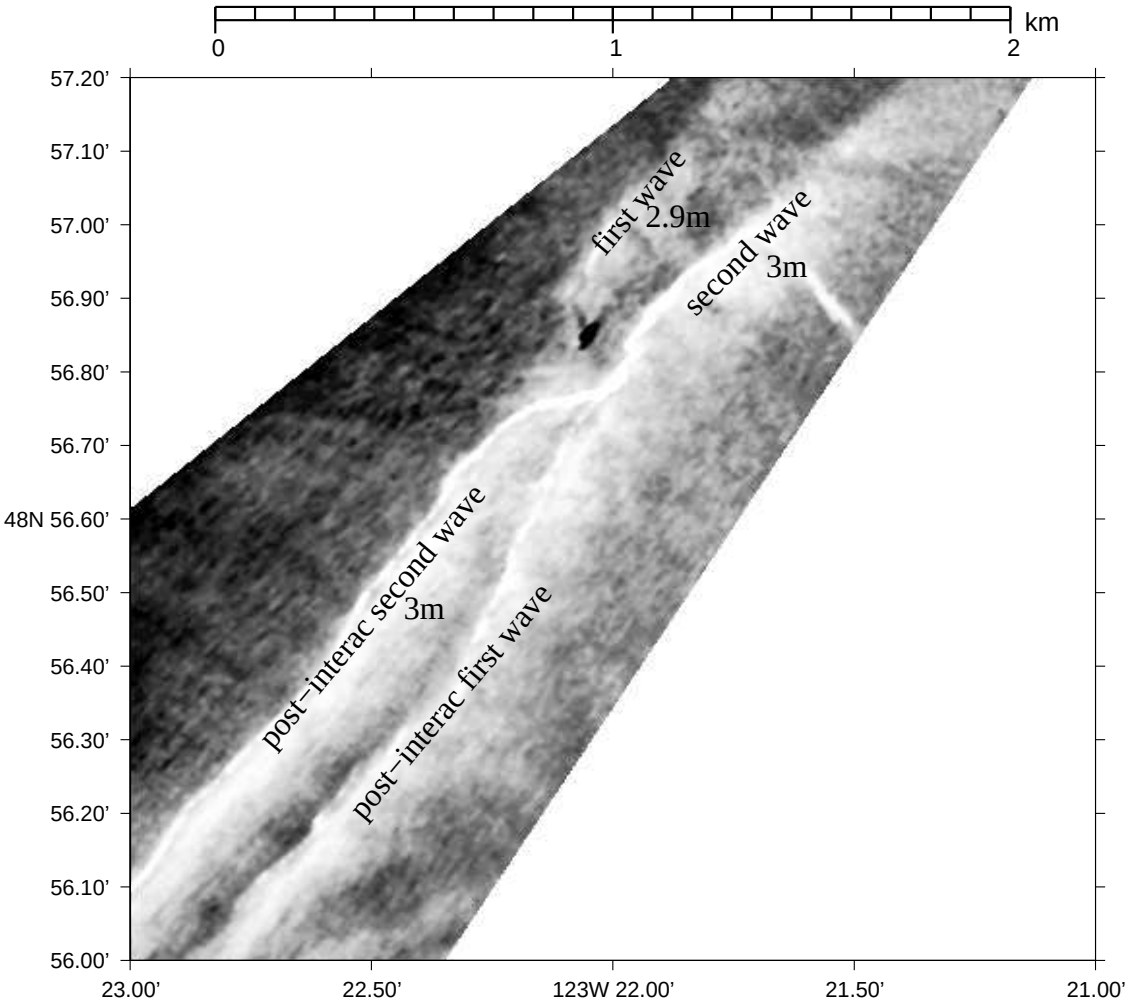

Figure 4.12: Image of wave-wave interaction on June 10, 2002. Second wave propagates faster than first wave. After interaction, second wave jumps forward, while first wave shifted backward.

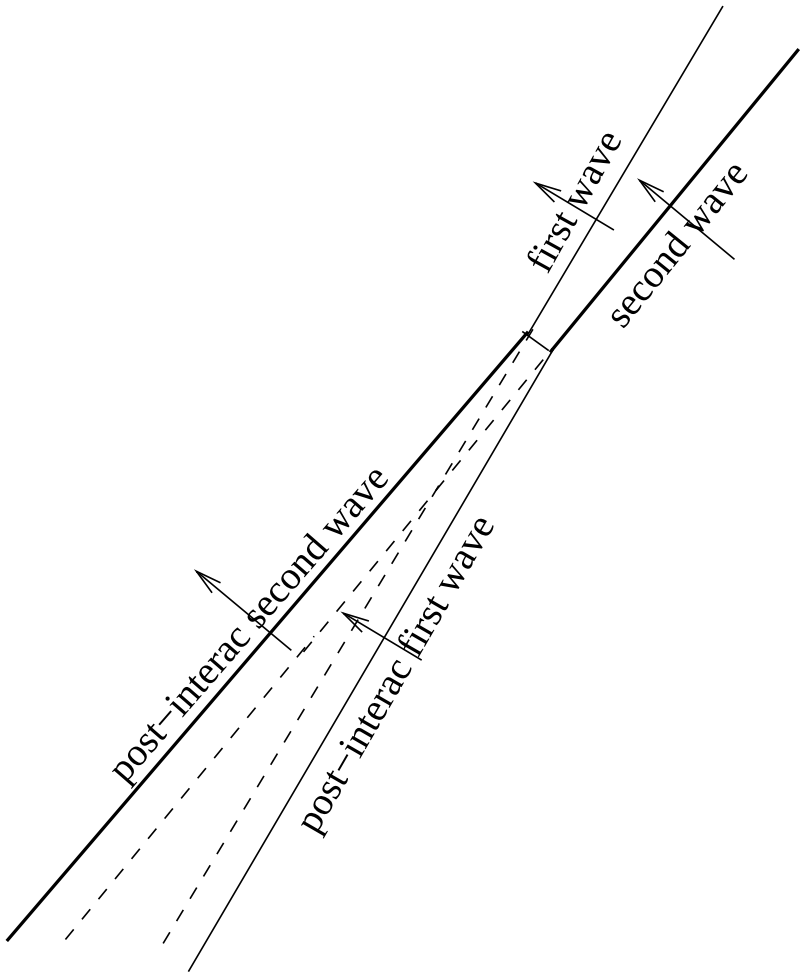

Figure 4.13: Diagram of wave-wave interaction on June 10, 2002.

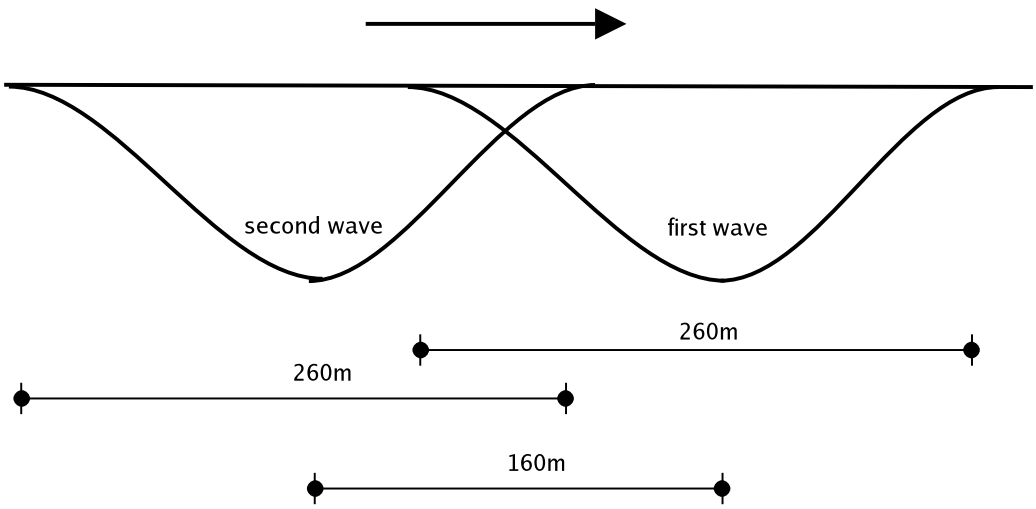

Figure 4.14: A cartoon of the two interacting waves on June 10, 2002.

with h_{eff}=[2 **4**] m. Since $\sin^2(\psi/2) \leq O(\eta'_{1,2})$, it is a strong interaction according to Miles (1977 a, b). Also, $|\eta'_1 - \eta'_2| > \psi^2$, i.e. the interaction angle is small compared to the amplitude difference. Therefore, this is the second case in Figure 4.1. The first wave shifted backward while the second wave shifted forward.

4.3 Theory Comparison and Discussion

I now re-examine some of the cases (interactions observed on June 26, July 15, and June 25) and compare with available theory of Miles (1976) more quantitatively because these wave cases fall in the parameter domain of Mach interaction while their appearances are somehow different from a Mach interaction.

The presumed Mach interaction observed on June 26 (Figure 4.4) is compared with the theory of Miles (1976) in more detail. If treated as a Mach reflection, the incident angle is $\psi_i = 0.7$ ($i.e. \frac{\psi}{2} = 42°$), and the incident amplitude, $\eta_i = \eta_e = 3.8$ m, is non-dimensionalized as $\eta_i^{'}$= [**0.9** 1.9]. The reflected angle is similarly taken as half of the angle between the

wave normals of the post-interaction western and eastern waves, which is approximately $\psi_r = 0.8 \pm 0.17$ ($i.e. \frac{(50\pm20)^\circ+40^\circ}{2} = (45 \pm 10)^\circ$). Due to the uncertainty of this angle, there is an error of the value of the reflected angle ψ_r as well. Using these values we compute various parameters for both regular and Mach reflection cases, and compare them with observations (see the first three columns of Table 4.1, end of this chapter). Observations of these parameters are in the last column of Table 4.1.

The comparison of the interaction as shown in Table 4.1 does not match either regular or Mach reflection predictions, but the differences are consistent with those described by Tanaka (1993) for larger amplitude waves and can be summarized as:

- The observed Mach stem step angle is significantly greater than zero and it is smaller than the theoretical value of a Mach reflection case.
- The observed Mach stem amplitude is smaller than the run-up in a regular reflection case and closer to the theoretical Mach stem amplitude.
- The observed reflected wave amplitude lies between the theoretical values of regular and Mach stem reflections.
- The observed "reflection" angle appears to be smaller than its value if treated as a theoretical Mach stem interaction and greater than the theoretical regular reflection although there is an uncertainty associated with estimating the reflection angle ψ_r.

Overall, the observed reflection characteristics for the observed large amplitude waves deviate from those of the theoretical small amplitude Mach stem reflection towards those of the theoretical regular reflection. The degree of agreement depends somewhat on the h_{eff} used in nondimensionalization. The weaker the nonlinearity i.e. the deeper the upper layer depth h_1 (highlighted as bold characters), the closer the results to the theoretical values

of weakly nonlinear Mach stem reflection. The stronger the nonlinearity (decreasing h_1), the closer the results are to those of a regular reflection. We hypothesize that the above deviations from the weakly nonlinear Mach reflection are caused by the strong nonlinearity i.e. the large non-dimensionalized amplitudes of the waves involved. Although this case has stronger nonlinearity ($\eta' \approx 1$) than Tanaka's (1993) numerical model, where $\eta^{'} = [0.1\ 0.3]$, our results agree with his numerical results stating that the effect of large amplitude tends to prevent the Mach reflection from occurring. Even when a Mach reflection occurs, it is "contaminated" by regular reflection (Tanaka, 1993).

We can also compare our observations with the numerical experiments of Tsuji and Oikawa (2001) who numerically studied some cases of deep-water internal wave interactions. Their main results are summarized as: with incident wave amplitude $\eta_i' = 2$ (non-dimensionalized by the thinner layer depth), the critical angle for Mach reflection is $\psi_c = 59°$, i.e. it is Mach reflection if the incident angle $\psi_i < 59°$ (for the weakly nonlinear theory this critical angle occurs when $\eta_i' = \psi_i^2/3 \approx 0.3$) and the maximum stem amplitude occurs when $\psi_i \approx \psi_c$, i.e. close to the critical angle. At our observed amplitude of $\eta_i' \approx 1$ the measured incident angle of 42° must be close to critical.

The observed asymmetry in angles between the stem and the two original waves (Figure 4.5) is likely caused by the differences in amplitude between the two interacting waves. According to the analytical results of Matsuno (1998) studying oblique interaction in a deep-fluid system, to leading order the phase shift does not depend on the amplitude, but in the second order it is proportional to the amplitude of the other wave. For our large wave amplitudes, the second order is important and can not be neglected. Therefore, it might be expected that the phase shift of the smaller wave (western front) is greater than the larger wave (eastern wave). Our observations showed that not only do the distances between the

post-interaction and the original waves depend on each other's wave amplitudes, the direction rotations due to a Mach interaction are also related to the other wave's amplitude. The larger wave (eastern wave) is rotated a smaller angle than the smaller wave (western front). Due to the combination of the asymmetric phase shifts and direction rotations, the Mach stem is inclined to the direction of the larger wave and causes the observed asymmetry.

The comparison of the second Mach interaction observed on July 15 (Figure 4.8) with Miles (1977 a, b) is very similar to the case on June 26 as we can see from Table 4.2. This Mach reflection is also contaminated by regular reflection because of the strong nonlinearity of the interacting waves. The observed Mach stem step angle, the reflected wave amplitude, and the reflection angle are all smaller than the theoretical values of a pure Mach reflection. The incident angle of this case is also smaller than the critical angle of 59° found by Tsuji and Oikawa (2001) for $\eta_i' = 2$, therefore, this suggests the observed interaction could still qualify to be a Mach interaction under the circumstance of strongly nonlinear and deep-water waves.

The interaction observed on June 25 (Figure 4.10) is also studied as a reflection problem and compared with Miles (1977 a, b). The western front with the greater amplitude is taken to be the incident wave. The post-interaction eastern wave is the reflected wave. The incident wave amplitude is η_2' and the reflected wave amplitude is η_1'. The incident angle is half the interaction angle, $\psi_i = 30°$, and the reflection angle is $\psi_r = 35°$. The asymmetry is again caused by the different wave amplitudes of the interacting waves. The comparison results are shown in Table 4.3. Surprisingly, the comparison is not dramatically different from comparisons we did on the interaction cases of June 26 and July 15 even though the interaction pattern seems much different. However, recall that the theoretical values for either regular or Mach reflection are meant to work only for waves with very small

wave amplitudes. The comparison with Miles' small amplitude theory can only tell us that our observations of not small waves lie somewhere in between regular reflection and Mach reflection despite its appearance of a regular reflection or Mach reflection. With $\psi_i < \psi_c$ $(= \sqrt{3\eta_i'})$ satisfied, this case is inside of the Mach reflection regime of Miles. However, recalling the definition of Mach stem, "the apex of the incident and the reflected waves moves away from the wall at a constant angle (stem angle) and is joined to the wall by a solitary wave called Mach stem" (Tanaka, 1993), there is no Mach stem observed in this case. We are not alone with this finding. In Tanaka (1993), a numerical experiment was carried out for $\eta_i = 0.3$ and $\psi_i = 40°$, and it was found that the stem length did not grow and $\eta_r = \eta_i$, which indicated that it was actually a regular reflection rather than a Mach reflection even though $\psi_i/\sqrt{3\eta_i'} = 0.736 < 1$. Therefore, even when the above condition of Miles is satisfied, when the wave amplitudes are large enough, a Mach stem interaction may not occur. Correct predictions in large amplitude cases clearly require a more sophisticated theory.

A second possibility is that the wave magnitudes and/or the difference in wave amplitudes may be large enough that the above Miles' criteria of phase conserving, reflection, and Mach stem interaction are not applicable any more. Therefore, we may be seeing case 2 of Figure 4.1. That is, it is fundamentally a shallow-angle interaction with one wave (western front) shifted forward and the other wave (eastern wave) shifted backward as illustrated in Figure 4.15.

We have examined a number of cases in which internal waves are interacting nonlinearly. Although our conclusions are far from comprehensive, they represent the first examinations of these effects in a geophysical situation. Overall, it is found that although the behavior described by the weakly nonlinear equation is qualitatively correct, a detailed comparison

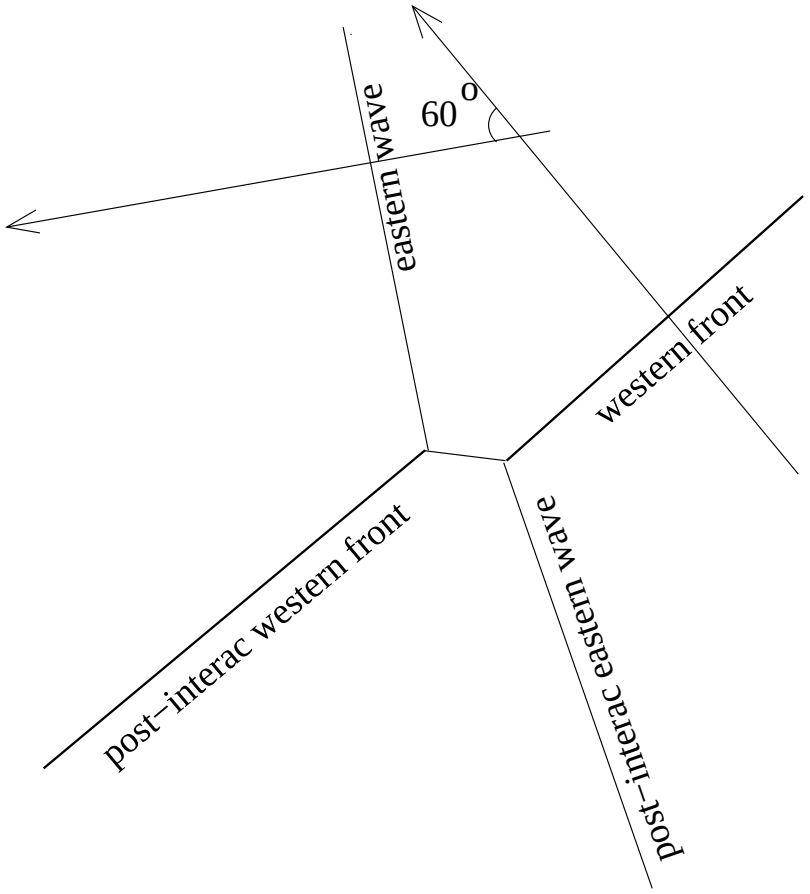

Figure 4.15: The interaction pattern on June 25, 2002 can also be viewed as Case 2) of Figure 4.1. The western front and the eastern wave interact. After interaction, the western front is shifted forward and the eastern wave is shifted backward.

shows significant deviations. In particular, when Mach interactions occur, it appears that the growth and amplitude of the Mach stem appear to be somewhat less than predicted. On the other hand, at this level of comparison it is not clear what (if any) difference may be expected between shallow and deep interactions. Our findings on the limitations of Miles' theories are at least consistent with those of Tanaka (1993). The discrepancies of the comparison between our observation and Miles theory can also be due to the fact Miles theory is for surface waves. It would be interesting to compare with interaction studies in a sheared continuously stratified system. Some of the discrepancies may be due to this.

In future research on Mach interaction, an effort should be made to track the Mach stem and the reflected wave for a longer time, at least several hours. A time series of Mach stem and reflected wave amplitude growth over their time scales may provide a better idea of the process of Mach interaction as it reaches its asymptotic state. Furthermore, the rate of the process or the growth of Mach stem may be measured in order to have an idea of how slow this process is and if this process is steady i.e. with constant growth rate. However, the spatial variations of density profile, current shear, and other effects of an actual ocean will all make this task even more complicated.

Parameter	Theory		Observation
$\varepsilon \equiv \frac{\psi}{2}/\sqrt{3\eta_i'}$	$\varepsilon \geq$ 1 Regular Reflection (small amplitude)	$\varepsilon < 1$ Mach Reflection (small amplitude)	ε=[0.3 **0.4**] (large amplitude)
Step angle ψ_*	0	$\sqrt{\frac{1}{3}\eta_i'}\,(1-\varepsilon)$ ([**19** 32]°)	$4° \pm 2.5°$
Interaction amp. η_M	non-grazing (maximum run-up) ([**13** 18] m)	$(1+\varepsilon)^2\eta_i$ (Mach stem)([6.4 **7.4**] m)	$>$ 3.8 m (based on wave speed observations)
Reflected wave amp. η_r	η_i (3.8 m)	$\varepsilon^2\eta_i$ ([0.33 **0.66**] m)	$\approx$ 3.3 m
Reflection angle ψ_r	ψ_i (42°)	$\sqrt{3\eta_i'}$ ([97 **137**]°)	$(45 \pm 10)°$

Table 4.1: Interaction on June 26, 2002.

Parameter	Theory		Observation
$\varepsilon \equiv \psi_i/\sqrt{3\eta_i'}$	$\varepsilon \geq$ 1 Regular Reflection (small amplitude)	$\varepsilon < 1$ Mach Reflection (small amplitude)	ε=[0.35 **0.5**] (large amplitude)
Step angle ψ_*	0	$\sqrt{\frac{1}{3}\eta_i'}\,(1-\varepsilon)$ ([**17** 30]°)	$10° \pm 5°$
Interaction amp. η_M	non-grazing (maximum run-up) ([**11** 14] m)	$(1+\varepsilon)^2\eta_i$ (Mach stem)([7 **9**] m)	$>$ 4 m (based on wave speed observations)
Reflected wave amp. η_r	η_i (4 m)	$\varepsilon^2\eta_i$ ([0.5 **1**] m)	3.2 m
Reflection angle ψ_r	ψ_i (49°)	$\sqrt{3\eta_i'}$ ([99 **140**]°))	54°

Table 4.2: Interaction on July 15, 2002.

Parameter	Theory		Observation
$\varepsilon \equiv \psi_i/\sqrt{3\eta_i'}$	$\varepsilon \geq$ 1 Regular Reflection (small amplitude)	$\varepsilon < 1$ Mach Reflection (small amplitude)	ε=[0.35 **0.5**] (large amplitude)
Step angle ψ_*	0	$\sqrt{\frac{1}{3}\eta_i'}\,(1-\varepsilon)$ ([**21** 37]°)	0
Interaction amp. η_M	non-grazing (maximum run-up) ([**43** 75]m)	$(1+\varepsilon)^2\eta_i$ (Mach stem)([11 **13**]**m**)	not available
Reflected wave amp. η_r	η_i (6m)	$\varepsilon^2\eta_i$ ([0.7 **1.5**]m)	not available
Reflection angle ψ_r	ψ_i (30°)	$\sqrt{3\eta_i'}$ ([122 **172**]°)	35°

Table 4.3: Interaction on June 25, 2002.

Chapter 5

Internal Wave Generation

Shand (1953) and Gargett (1976) both suggested that the large internal wave packets in the Strait of Georgia formed after an ebb tide and on the turn to flood tides at the southern passes. They also stated that weaker groups or no groups at all were formed after a flood tide, on the turn to ebb. However, neither of these works (nor any others) were particularly helpful in trying to identify the location and appearance of wave packets, and we spent some time in our field program performing large-scale searches to locate suitable wave packets. After making photo-mosaics of the images from our surveys, it is found that wave packets often have a large-scale curvature, which suggests "point" generation (Figure 5.1).

Although the previous chapters have concentrated on small-scale aspects of internal waves, the photographic technique can also be used to shed some light on internal wave generation mechanisms. The basic analysis task here will be to propagate a point source with observed speed (combination of wave phase speed and tidal currents) from a particular time and origin location to match the observed wave fronts. The obvious approach of propagating wave crests (smoothed) backwards in time to their source proved unworkable as the effects of small curvature irregularities were exponentially amplified. Very crudely we can guess that the center of the wave front curvature may be related to the point of origin. Advective effects will modify this apparent source location. The time frame in which waves were generated can also be roughly estimated. Intuitively, after the origin of a curved wave

front is found, by measuring the distance between the origin and the wave front, and then dividing the distance by the sum of the wave phase speed and (perhaps) barotropic tide, the time when the wave is generated can be estimated. For this purpose we need to identify the location of wave fronts over a wide spatial area, which we have done with high-altitude aerial surveys. The propagation speed of wave fronts are obtained in earlier chapters. The tidal speeds are estimated using a tidal currents model (Foreman et al., 1995). Once the origin time and location that predict the wave front that most closely match the observed front are found, by analyzing the tidal cycle and the local topography, we can infer whether the internal waves were generated downstream during the ebb tide or upstream during the flood tide, and draw some conclusions about generation mechanisms.

5.1 Case Studies

During wide-area aerial surveys the aircraft flew at an altitude of about 1000 m over the Strait. June 26 will be taken as an example to provide details of the analysis. Figure 5.1 is a mosaic of images from 13:50 to 14:05 on June 26, showing curved wave packet fronts. Curvature of the right-hand-side packet is almost 90° of arc, and the wave crests are about 20 km long. Wave crests in the left-hand-side packet are also about 20 km in extent but the curvature is much less pronounced. The curvature suggests point or near-point source generation to the south of the Strait of Georgia. The right-hand-side packet appears to radiate from a point northwest of Boundary Pass, consistent with the suggestion of Gargett (1976). The left-hand-side packet appears to radiate from a point somewhat southwest of Boundary Pass. This packet is most probably generated at some place other than the Boundary Pass. The reason for the lack of curvature is uncertain but may be due to the effect of tidal advection, or may be due to non-point source generation.

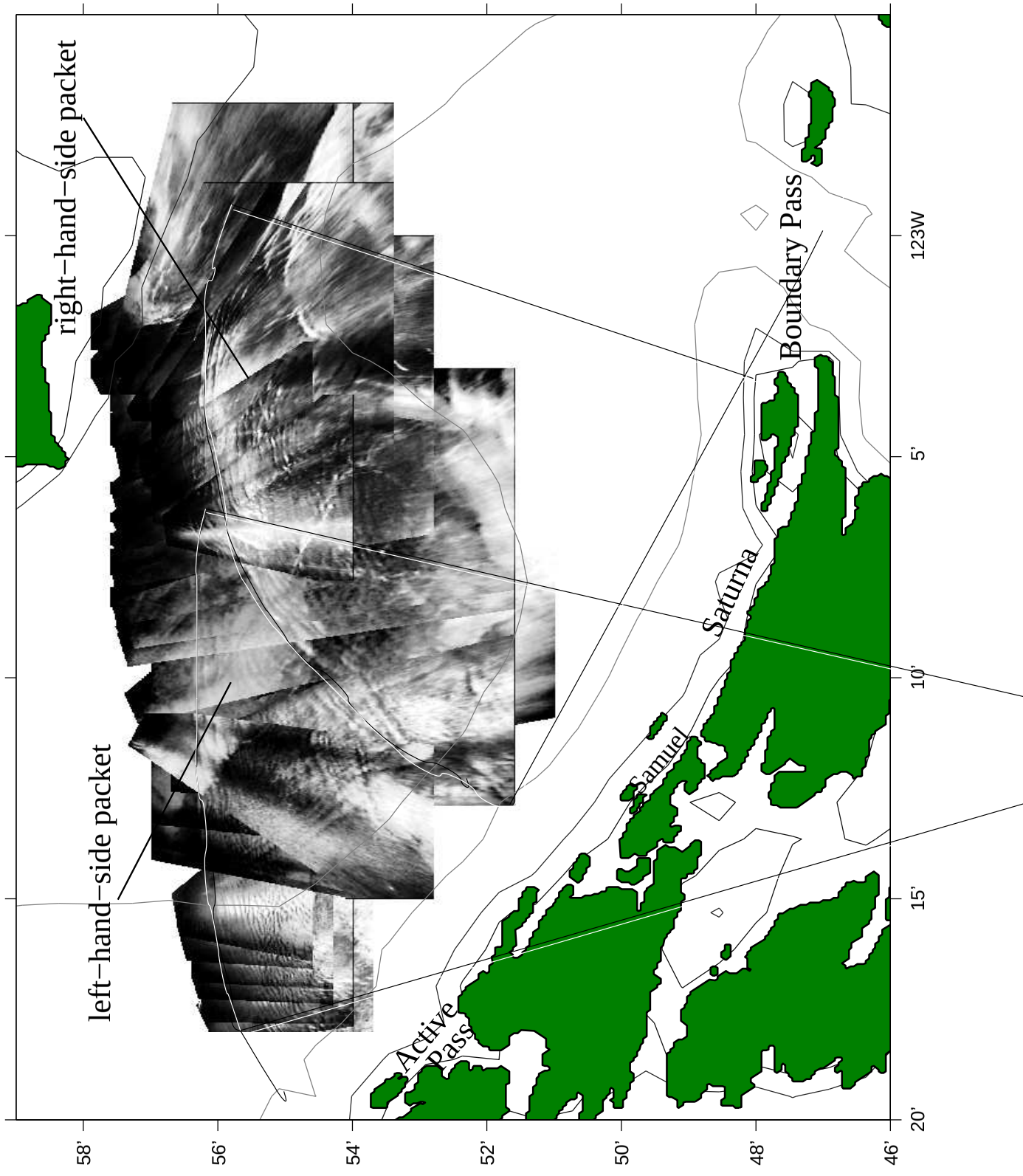

Figure 5.1: Photo mosaic showing internal wave packets across the Strait on June 26, 2002.

Knowing the time series of tidal currents $\overrightarrow{v}_{tide}$ in the Strait, the known time t_1 that the wave front appears at the position shown in the mosaic image (Figure 5.1), and the wave phase velocity $\overrightarrow{c}$ (from analysis in chapters 3 and 4), we can estimate the time t_0 when these internal waves started to propagate into the strait. Imagine a wave crest at location $\overrightarrow{x}$ moving with phase velocity $\overrightarrow{c}$ further advected by a tidal current $\overrightarrow{v}_{tide}(\overrightarrow{x})$. The wave phase velocity $\overrightarrow{c}$ can change magnitude if stratification and/or wave amplitude changes and can change direction by horizontal refraction caused by spatial variations in the stratification, but (lacking suitable observations) we ignore these effects and take it to be uniform.

Then

$$\frac{d\overrightarrow{x}}{dt} = \overrightarrow{c} + \overrightarrow{v}_{tide}(\overrightarrow{x}(t)), \tag{5.1}$$

or

$$|\overrightarrow{x}(t_1) - \overrightarrow{x}(t_0)| = R = |\int_{t_0}^{t_1} (\overrightarrow{v}_{tide}(\overrightarrow{x}(t)) + \overrightarrow{c})dt|, \tag{5.2}$$

and R would be the apparent radius of curvature for the wave front at $\overrightarrow{x}$ if t_0 is a generation time, and $\overrightarrow{v}$ depends only weakly on $\overrightarrow{x}$.

In this case, the center of the wave front is also moved by the tidal currents, and this distance D can be estimated as well:

$$D = |\int_{t_0}^{t_1} \overrightarrow{v}_{tide}(\overrightarrow{x}(t))dt|. \tag{5.3}$$

As the ambient velocity field is known approximately (through predictions of a constant-density model), a simple procedure based on ray propagation was used to study the propagation. Essentially a fan of rays at a particular place and time are generated, $\overrightarrow{x}(t_0)$,

and the rays are then propagated using equation 5.1 until our observation time t_1. The procedure is repeated over a grid of times at possible candidate generation locations and a "best match" to observations is chosen. There are clearly some limitations to this approach. First, although it was found in Chapter 3 that shear is important to the propagation of the observed waves in the Strait of Georgia, only predicted barotropic tide is considered here. There are no information about the large-scale field, nor about the variations of density stratification and wave dissipation and so these too are ignored. Therefore, the predicted wave front shape cannot be expected to match the observation in every detail.

Tidal current predictions for June 25 and 26 for several locations shown in Figure 5.3 are presented in Figure 5.2. Tides at Boundary Pass have large spatial gradients. The plotted values are the predictions at the mouth of Boundary Pass, close to the sill. Places away from the sill have much weaker tidal currents. The maximum predicted flood currents at Active Pass and Boundary Pass are both greater than 1.5 m s^{-1}, while at North Boundary Pass and Southern Strait locations, the tidal currents are much weaker, with maximums of around 0.5 m s^{-1}, still large enough to significantly affect propagation. In addition, the tide in the Southern Strait is delayed compared to that at Active Pass. The turning from ebb to flood in the Southern Strait is about 2 – 3 hours after that at Active Pass. Timing in previous chapters was referenced to the tidal cycles at Active Pass. When the western wave packet was observed around 14:00 between Active Pass and Point Roberts, as in Figure 5.3, tide at Active Pass was flooding, while in the strait, the tide was ebbing (Figure 5.3), and this fact was confirmed by our ADCP current measurements. Figure 5.3 also shows the complicated situation at Boundary Pass. At 14:00 on June 26, the tides close to the sill were flooding and the currents were as large as 2 m s^{-1}, while to the east, the tides were still ebbing and the currents were much weaker. Observations at Boundary

Pass in the summer of 2000 (Baschek, 2002) showed that the tidal currents at the sill were much stronger than those immediately next to the sill.

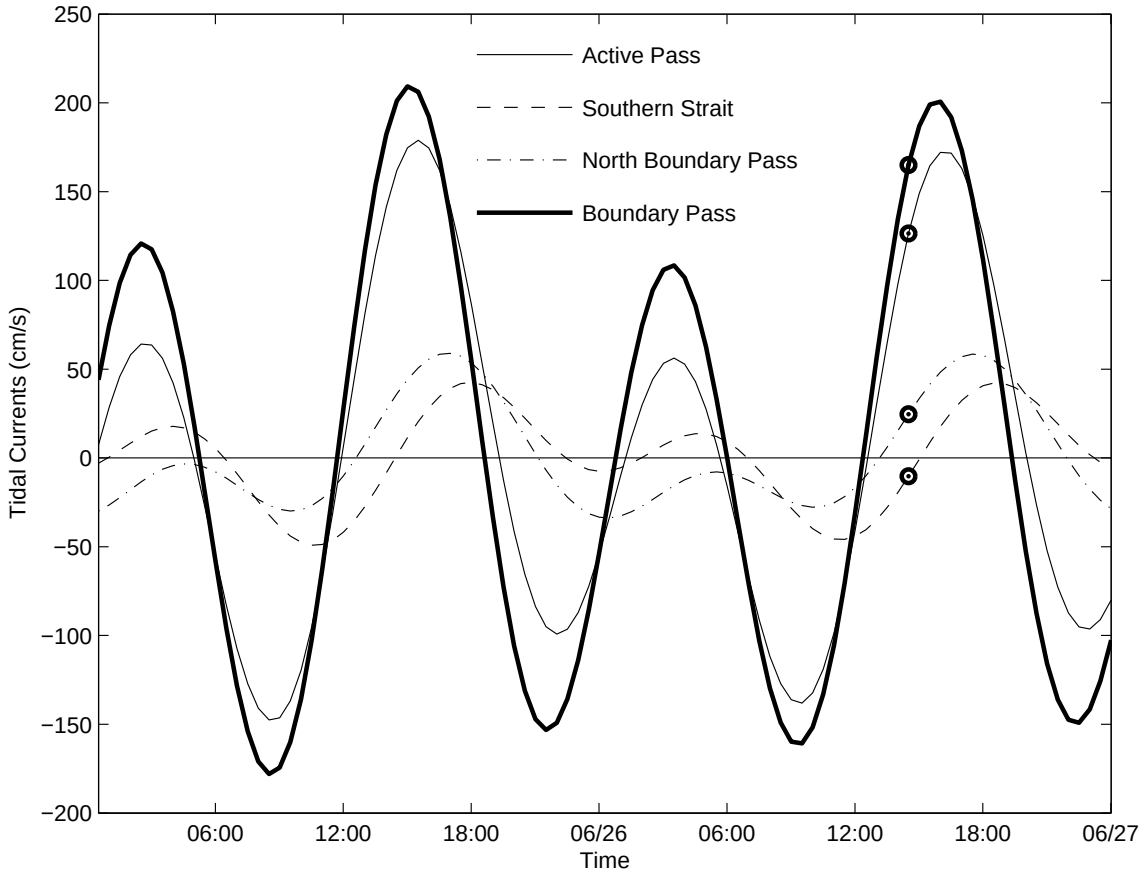

Figure 5.2: The predicted tidal currents with positive values for flood tides in the Strait of Georgia for June 26, 2002. 'o' marks the time when the wave fronts were observed around 14:00. Speeds are taken in the direction of maximum velocities, with positive roughly northwards.

Five possible "start locations" are investigated: Boundary Pass, the pass north of Samuel Island (North Samuel Island), the pass north of Saturna Island (North Saturna Island), the channel between the eastern end of Saturna Island and Tumbo Island (Tumbo Channel), and Active Pass (Figure 5.4). The predicted tidal currents at the five "start locations" are plotted in Figure 5.5. Start times are chosen to be between 6:00 on June 25 and 12:00 on June 26 for all of the five candidate start locations. During this day (Figure 5.1), the propagation speed of the right-hand-side wave packet is observed to be 0.7 ± 0.1 m s^{-1}.

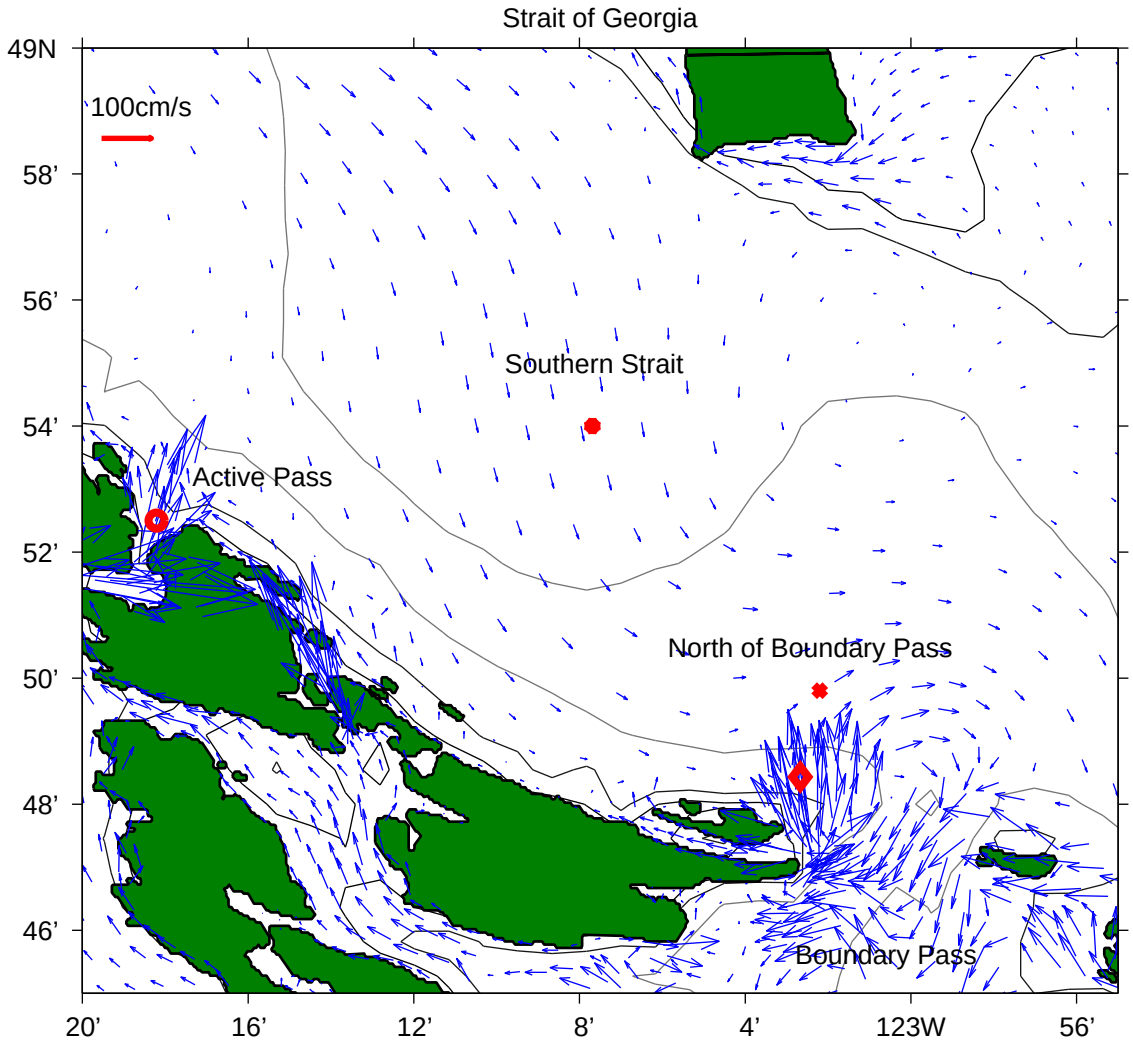

Figure 5.3: The predicted tidal velocity in the southern part of the Strait of Georgia at 14:00 on June 26, 2002. Ebb tides are generally southwards, and flood tides are northwards.

The left-hand-side wave packet has the wave speed of approximately 0.9 m s^{-1} with 10% uncertainty. We first look at the case of the right-hand-side wave packet.

First, Boundary Pass is taken as the start location for the right-hand-side wave packet. Between Boundary Pass and the Strait of Georgia, there is a steep sill blocking 80% of the passage and constraining the currents. The slope of the sill averages 30° and the depth of the sill top is about 60 m deep compared to the nearby 200 m deep bottom. As shown in Figure 5.5, at Boundary Pass, before the waves were observed around 14:00 on June 26, there are three ebb tides in total, which are denoted ebb-1, ebb-2, and ebb-3. None of the predictions match observations particularly well, but the best results (the predicted wave front matches closest with observation) are obtained for a start time between 2:00 and 4:00 on June 26 (Figure 5.6), with the range in time reflecting the uncertainty in measured wave speeds. The predicted tide in Figure 5.2 at Boundary Pass turned from ebb (ebb-2) to flood at about 1:00. Therefore, the optimized start time is after the ebb-2 tide turns to flood. Figure 5.6 shows that waves first traveled rapidly during the flood between 2:00 and 7:00 (Southern Strait, Figure 5.2), then slowed down during the ebb after 7:00, and finally reached the Active Pass - Point Roberts area around 14:00. At this time, the tide at Boundary Pass was at the transition from ebb-3 to the following flood. More waves generated at Boundary Pass would propagate into the Strait during the following flood and another generation-propagation cycle would be repeated.

Second, the pass north of Samuel Island (North Samuel Island) is taken as the start location. Although this passage is much smaller than Boundary Pass, it was thought at least plausible that its very shallow "sill" could act efficiently at generating near-surface internal waves. However, the best match of prediction to the observed wave front of the right-hand-side wave packet is not satisfying (Figure 5.7).

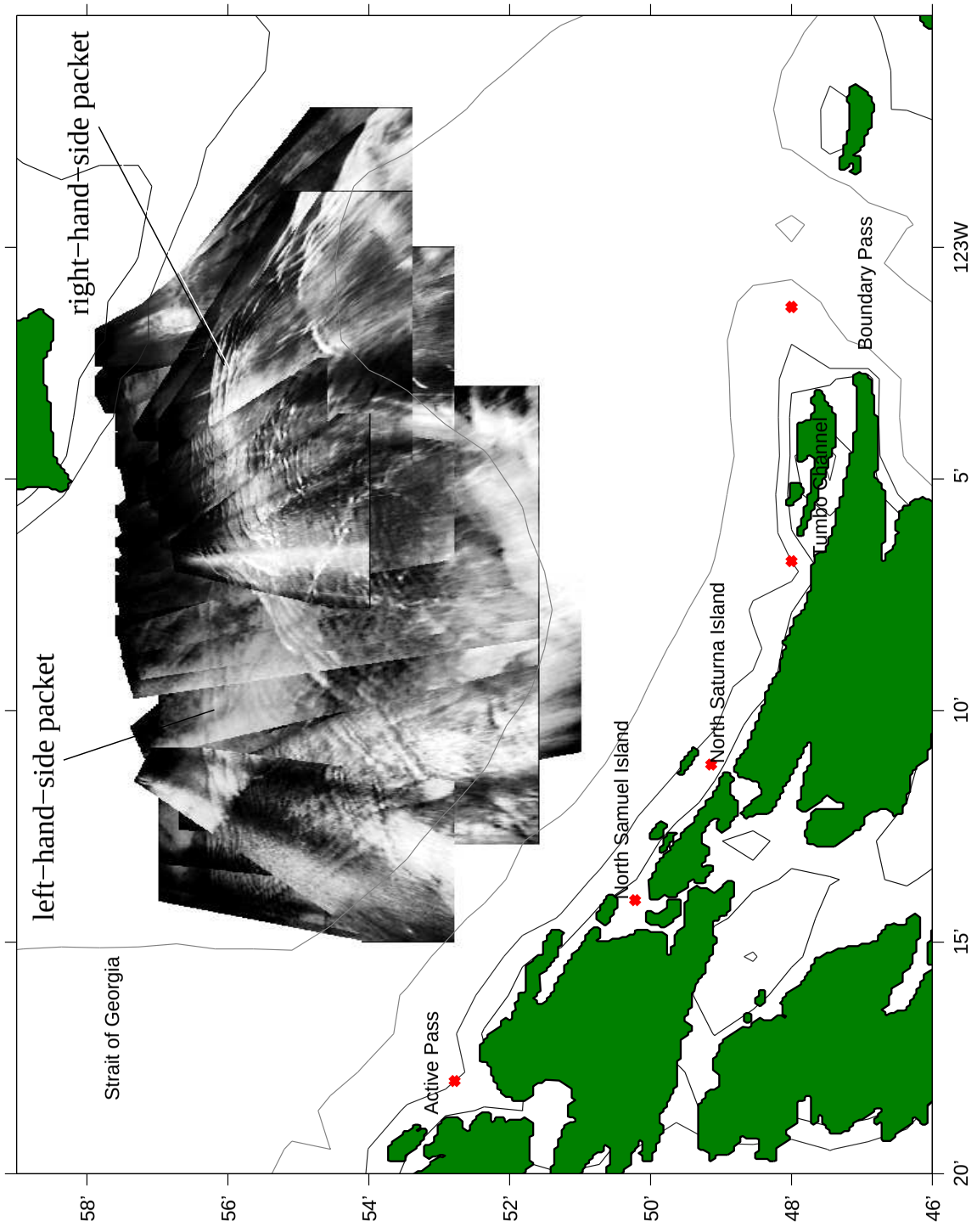

Figure 5.4: The five possible start locations for the observed waves (the photo mosaic) on June 26, 2002.

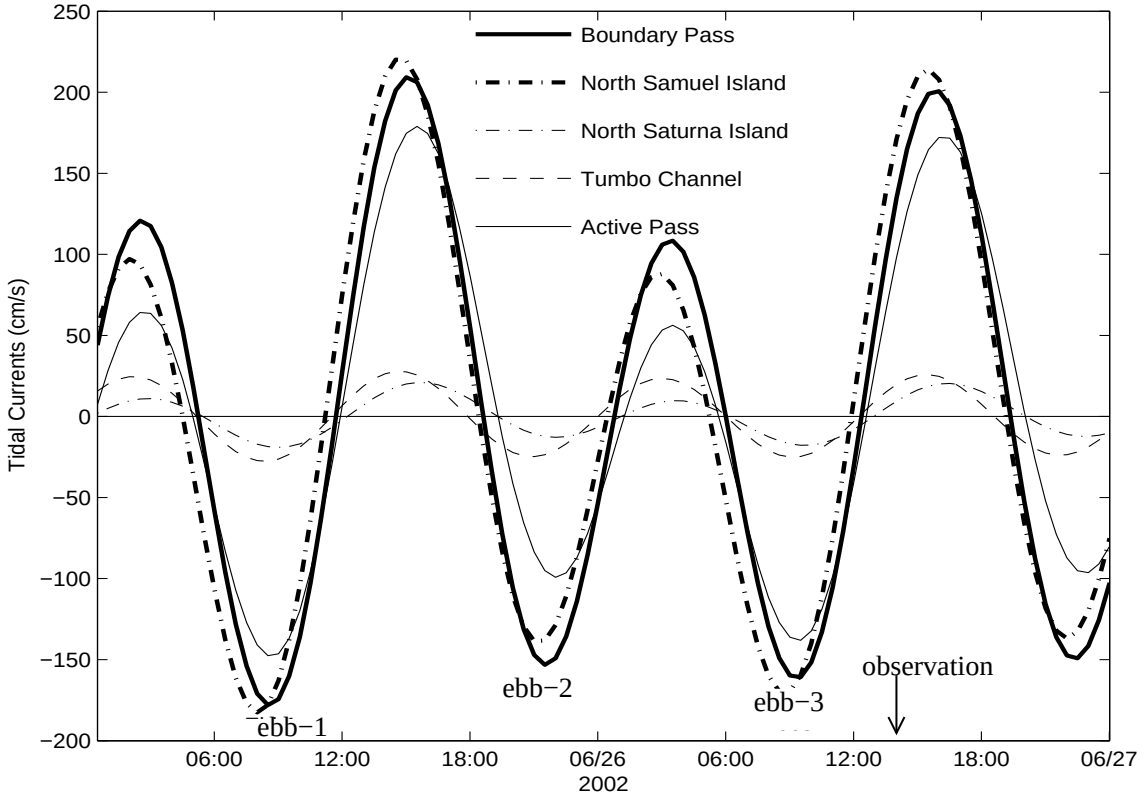

Figure 5.5: The predicted tidal currents at the five possible start locations on June 26 and the day before. Before the wave packets were observed around 14:00 on June 26, there were three ebb tides ebb-1, ebb-2, and ebb-3 during these two days.

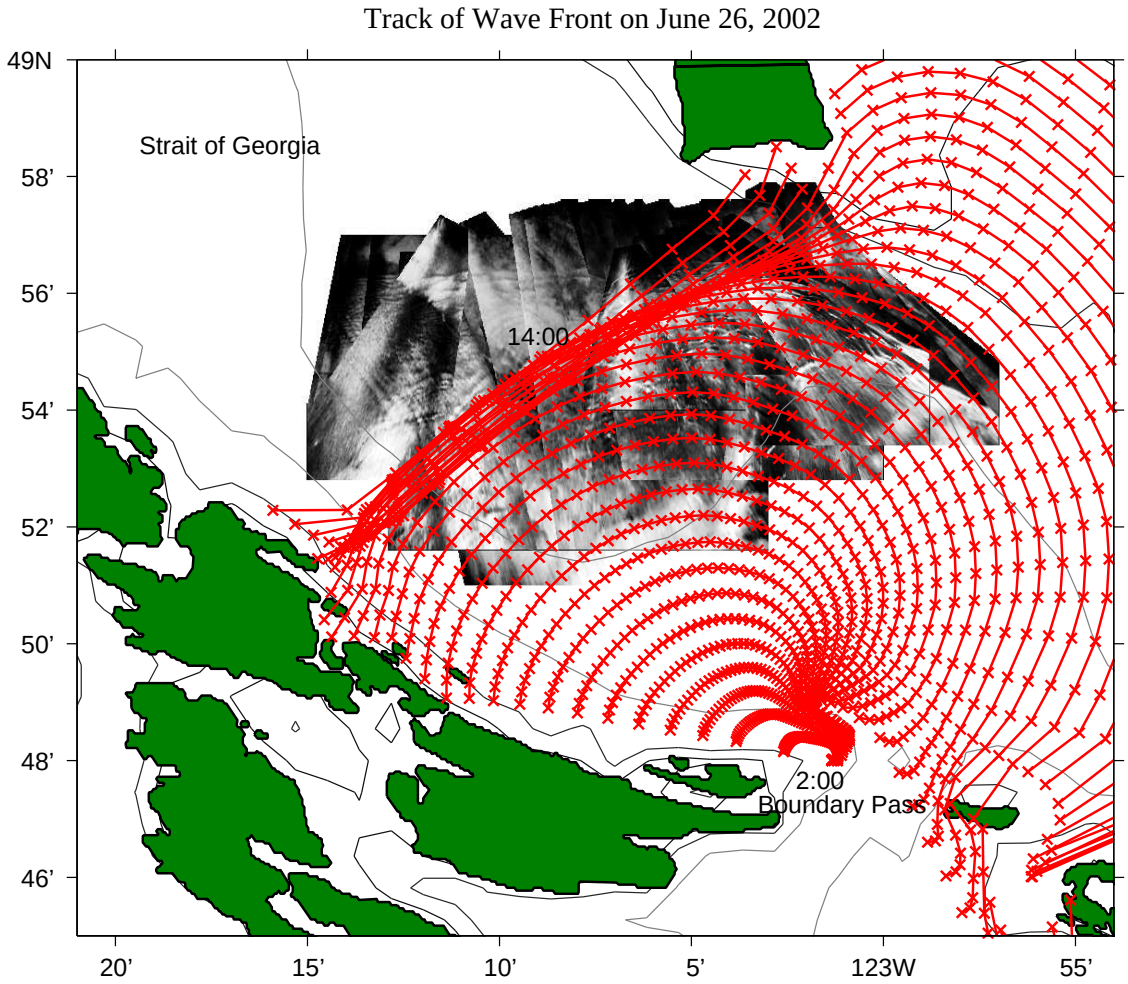

Figure 5.6: The optimized matching of the estimated wave packet front ('+-') with observation when Boundary Pass is taken as the start location. For these wave tracks, the start time is 2:00 and the wave speed is 0.6 m s^{-1}. The front tracks are plotted every 20 minutes.

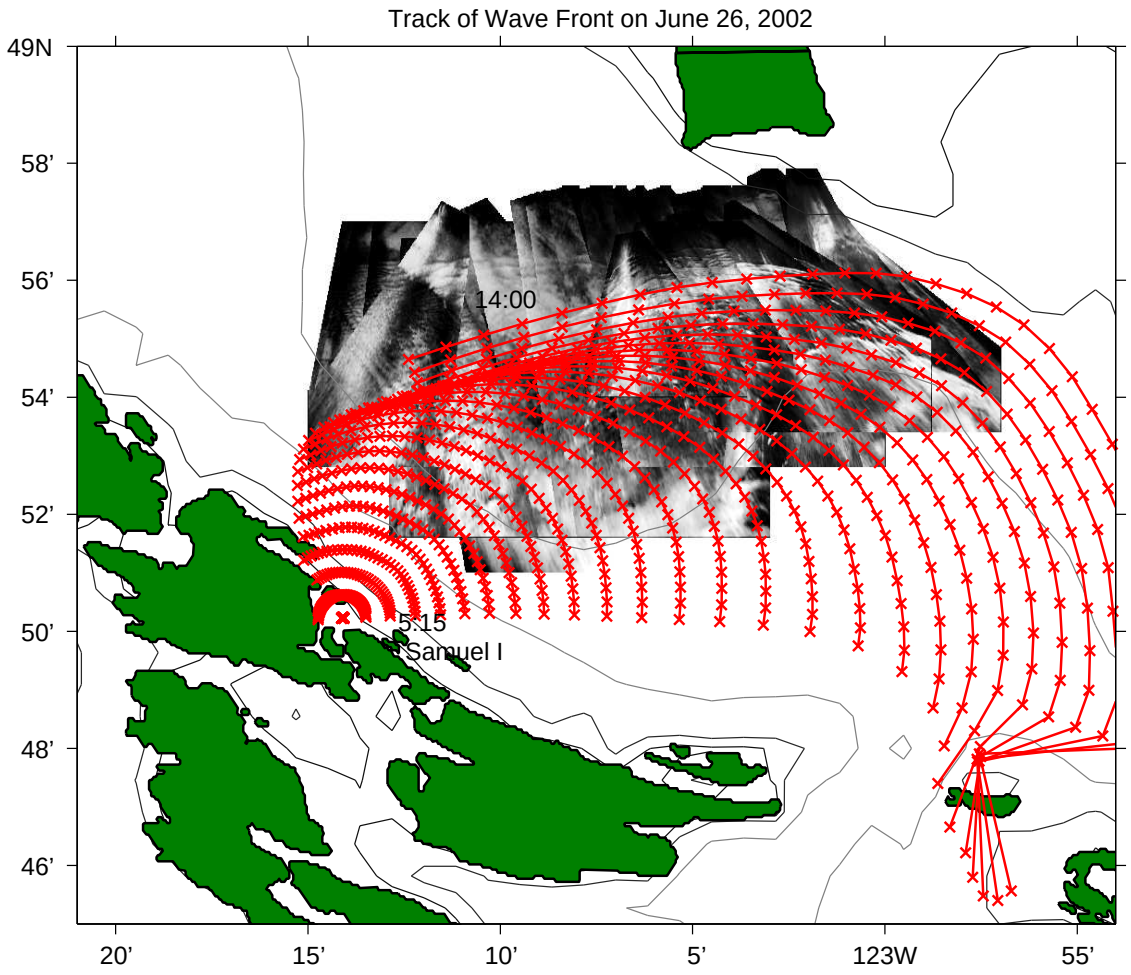

Figure 5.7: The wave front track plotted on top of the photo mosaic when North Samuel Island is taken to be the start location. For plotting the wave tracks on this figure, the start time is 5:15 and the wave speed is 0.6 m s^{-1}. The wave tracks are plotted every 20 minutes.

Third, the pass north of Saturna Island is taken as the start location. As shown in Figure 5.8, with a start time of 4:15 on June 26, the predicted wave front reached the location of the observed right-hand-side wave front at 14:00, but the curvature of the predicted wave front appears to be rather less than observed. Moreover, according to Figure 5.5, the tidal currents at North Saturna Island are likely too weak (< 0.5 m s^{-1}) to produce the observed waves which have phase speed over 0.6 m s^{-1}. The Saturna start location is therefore discarded.

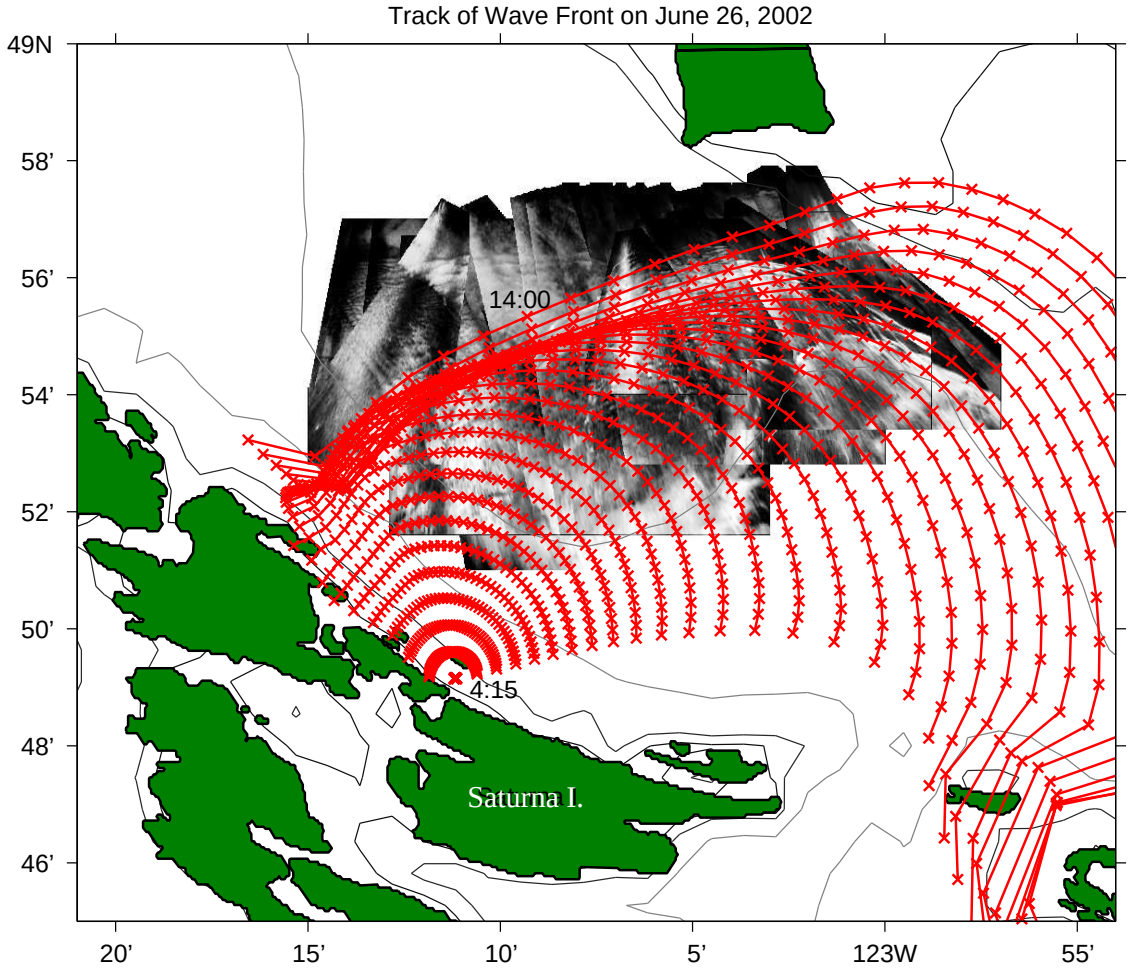

Figure 5.8: The wave front track plotted on top of the photo mosaic when North Saturna Island is taken to be the start location. The start time is 4:15 and wave speed is 0.6 m s^{-1}. The wave tracks are plotted every 20 minutes.

Fourth, Tumbo Channel is taken as the start location. If the right-hand-side wave

packet was formed at Tumbo Channel and then arrived at the area near Active Pass and Point Roberts at about 14:00, the start time has to be about 2:30 on June 26 (Figure 5.9). Like the situation at North Saturna Island, the predicted wave front is more straight than the observed curved wave front of the right-hand-side packet, and the tidal currents (< 0.5 m s^{-1}) are far from strong enough to generate the observed waves. Boundary Pass seems more plausible. Tumbo Island is excluded as well.

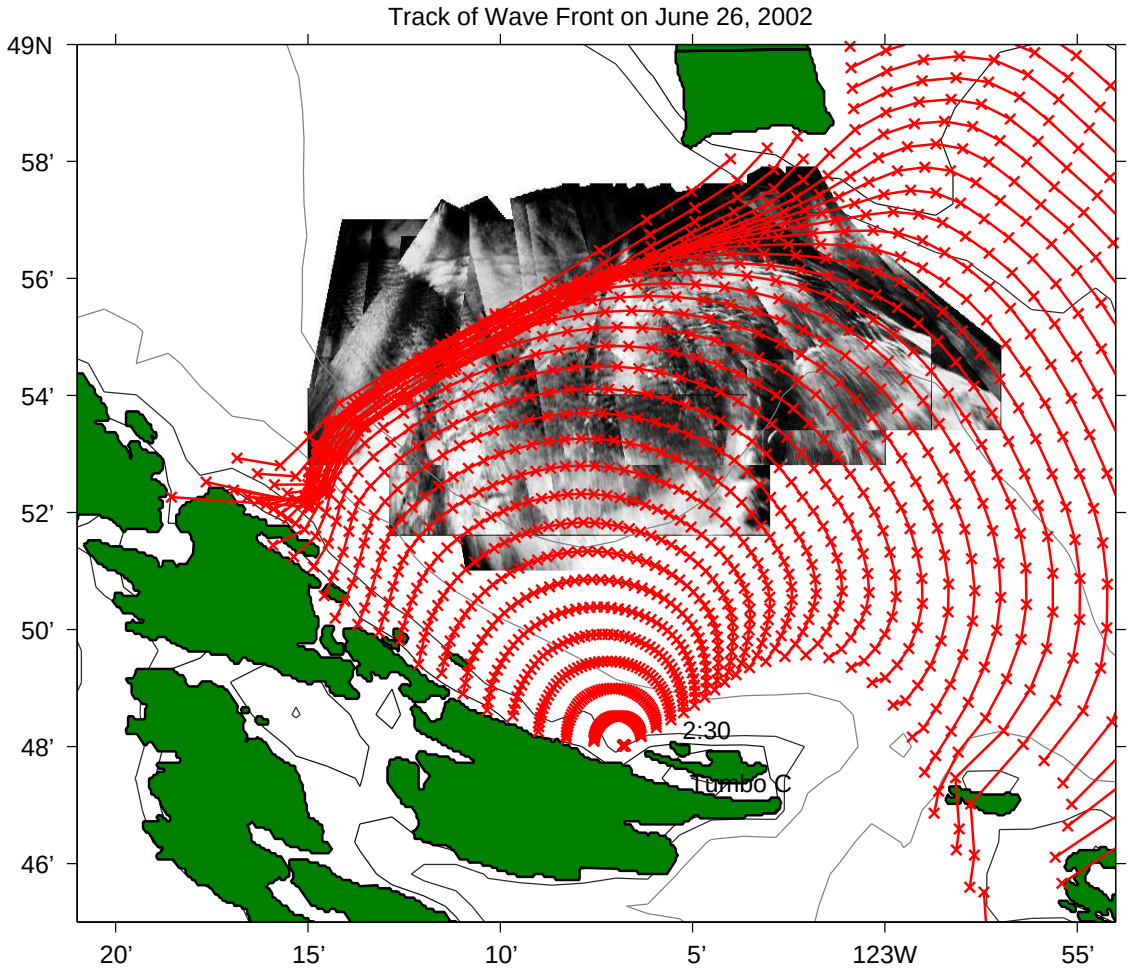

Figure 5.9: The wave front track plotted on top of the photo mosaic when Tumbo Channel is taken to be the start location. In order to match with observation, the start time is about 2:30 and the wave speed is 0.6 m s^{-1}. The wave tracks are plotted every 20 minutes.

Last, Active Pass is taken as the start location of the right-hand-side wave packet. If the waves in this packet were formed at Active Pass and then arrived at the area near

Active Pass and Point Roberts at about 14:00, the start time was estimated to be near 6:00 on June 26 (Figure 5.10). However, the predicted wave front does not match with the observed wave front of the right-hand-side wave packet. This start location can not be the right one.

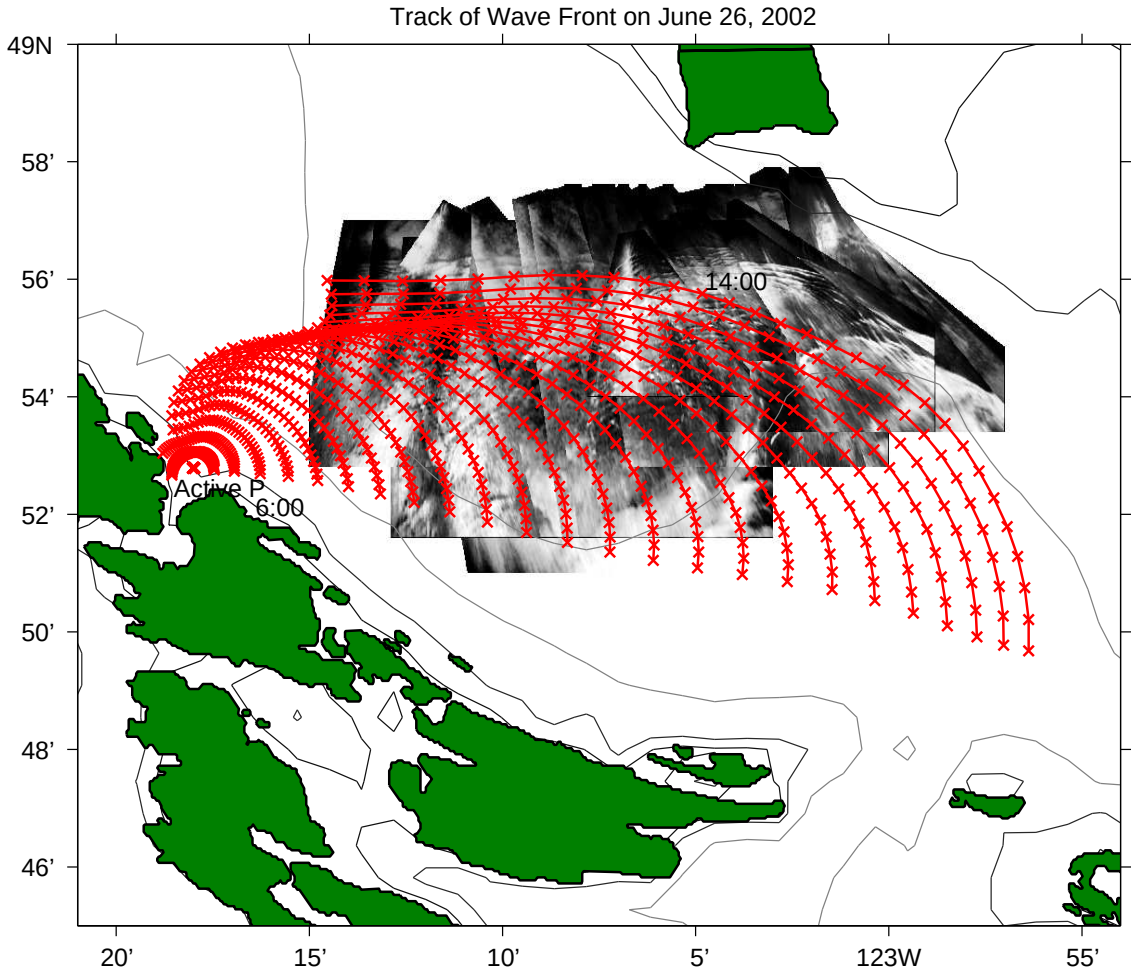

Figure 5.10: The wave front track plotted on top of the photo mosaic when Active Pass is taken to be the start location. The start time is about 6:00 and the wave speed is 0.6 m s^{-1}. The wave tracks are plotted every 20 minutes.

After trying with all the five candidate locations, it seems most likely that the observed right-hand-side wave packet in the area of Active Pass and Point Roberts is generated at Boundary Pass, propagating into the Strait of Georgia after ebb-2 turns to flood.

For the left-hand-side wave packet, we similarly propagate point generated wave rays

with the typical wave speed of the left-hand-side wave packet (0.9 ± 0.1 m s^{-1}) at the same five candidate start-locations trying to find the best match to the observed wave front. It is found that the best match of wave front is when North Samuel Island is the start location (Figure 5.11). However, the start time is estimated to be about 8:00, the peak ebb of ebb-3, therefore, even if waves were generated there, it is not likely that they were released during peak ebb. Hence, the best match of the left-hand-side wave packet was possibly, not definitely, generated at North Samuel Island.

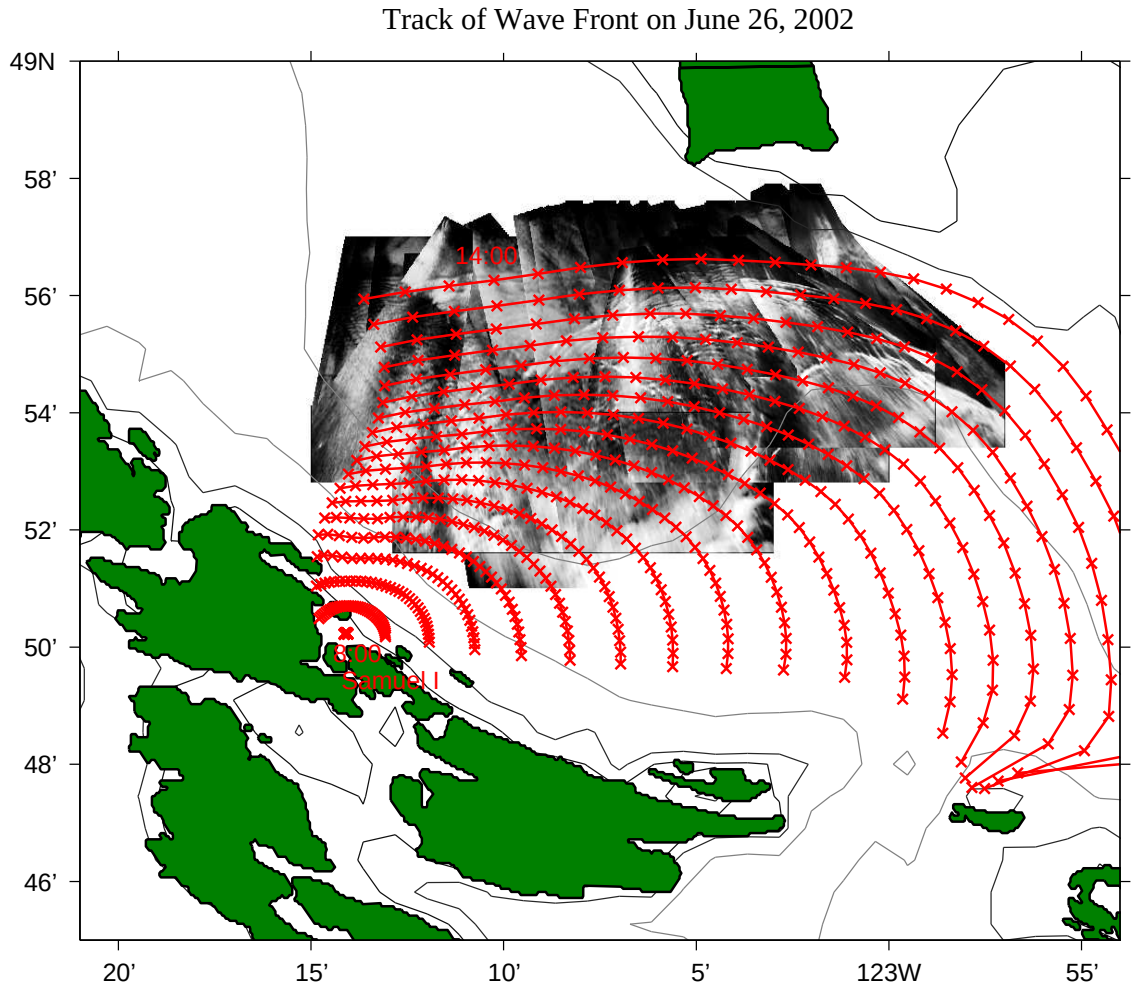

Figure 5.11: The wave front track plotted on top of the photo mosaic when North Samuel Island is taken to be the start location for the left-hand-side wave packet. For plotting the wave tracks on this figure, the start time is 8:00 on June 26. The wave tracks are plotted every 20 minutes.

Now we will try to understand why internal waves generated during the other ebb tides are not observed in our survey. Ebb-1 and ebb-3 (Figure 5.5) at Boundary Pass are taken as examples. If a wave was formed during ebb-1 at the downstream side of the sill, it most probably would make its way across the sill and into the Strait of Georgia after the flood current is strong enough. Without losing generality, assume this occurs near the following peak flood at 15:00 on June 25, approximately. The generated internal wave speed should not be lower than the observed speed (greater than 0.6 m s^{-1}) since ebb-1 is no weaker than ebb-2 as a source. Then if a wave of speed 0.6 m s^{-1} is propagated from 16:00 of June 25 to 14:00 of June 26, as shown in Figure 5.12, when we were present in the Strait of Georgia (around 14:00 on June 26), it would have travelled far to the north near Point Atkinson and be outside of our survey area (if it had not dissipated by then). The internal wave packet would appear around the region of Active Pass and Point Roberts around 19:00 on July 25. If the actual phase speed is higher than 0.6 m s^{-1}, the waves would be even further to the north. For the waves generated by ebb-3 on June 26, similar analysis is performed. The waves generated by ebb-3 most probably started propagating into the Strait around the peak flood near 16:00 on June 26, i.e. after our survey time. The waves generated would appear around our survey area in the evening of June 26 between 19:00 and 20:00 approximately (Figure 5.13). It is possible that waves do appear at these times, but we have no data from this late in the day.

The same analysis is carried out for five other days (May 24, June 7, June 10, June 25, and July 15). The right-hand-side wave packet consistently appears but the left-hand-side wave packet does not. The time period of images used and wave propagation speeds are summarized in Table 5.1. Generally speaking, for all of the studied days (refer to Figure 5.14) the right-hand-side wave packet was released into the Strait of Georgia sometime

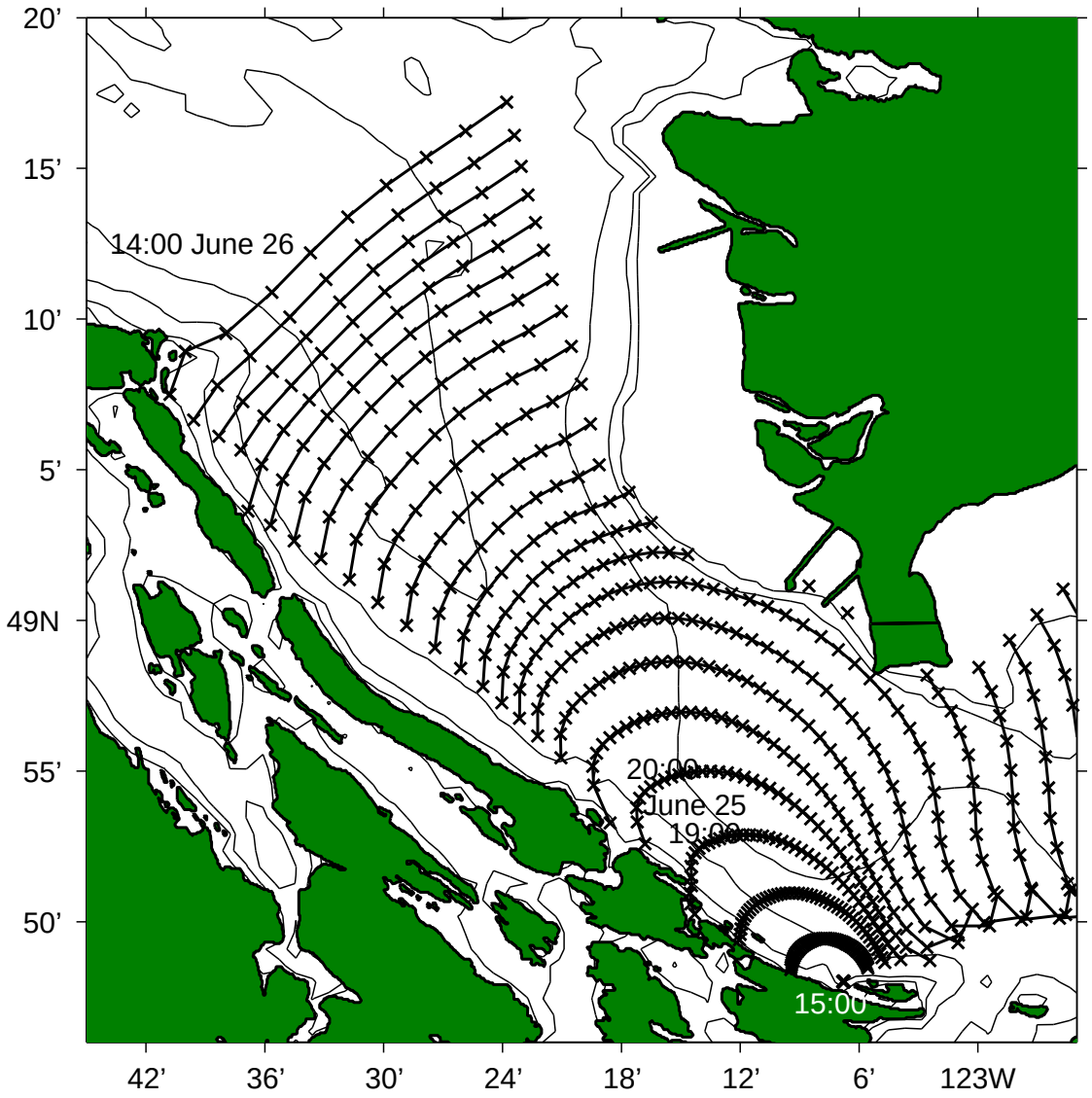

Figure 5.12: The front positions ('+-') of the wave formed during ebb-1 on June 25 at Boundary Pass. The front tracks are plotted every one hour. The wave started to propagate into the Strait of Georgia at 15:00 on June 25, arrived at the region around Active Pass and Point Roberts between 19:00 and 20:00 on June 25, and at 14:00 on June 26, it was around Point Atkinson.

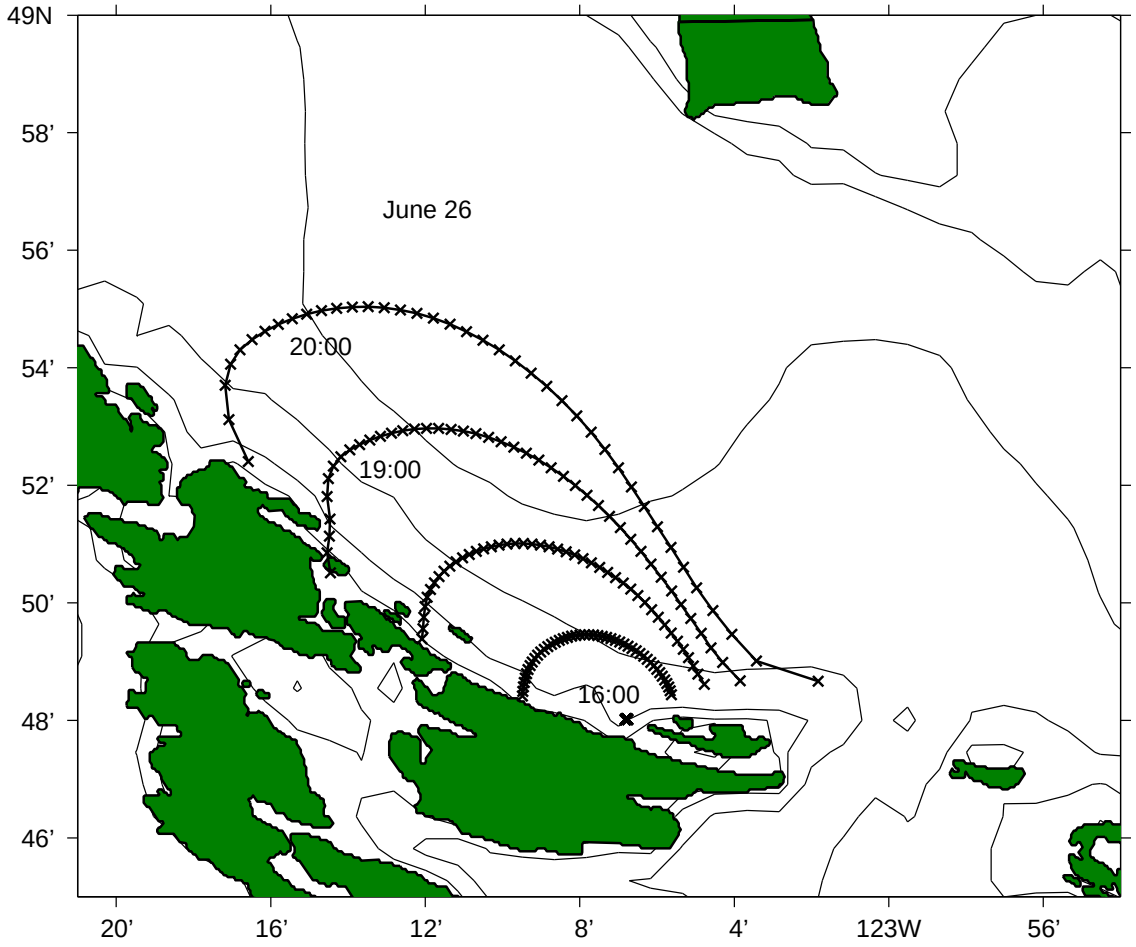

Figure 5.13: At 19:00 – 20:00 on June 26, the waves generated at Boundary Pass during ebb-3 on June 26 traveled to the Active Pass - Point Roberts Area. The "start time" is 16:00 on June 26. The front tracks are plotted every one hour.

Case study	Period of images used	Wave front speed (m s^{-1})
5/24/2002	11:30–12:03	1.05 ± 0.08
6/7/2002	10:58–12:20	0.75 ± 0.08
6/10/2002	14:06–14:33	1.05 ± 0.04
6/25/2002	13:30–14:35	0.87 ± 0.11
7/15/2002	14:23–14:38	0.6 ± 0.03

Table 5.1: Other generation case studies.

during the previous flood tide.

5.2 Summary and Discussion

After investigating all of the surveys, it appears that the observed right-hand-side wave packets are generated at Boundary Pass and released into the Strait during the following flood. Based on the tidal currents predicted by Foreman et al. (1995), it takes the waves generated during ebb-2 8 – 14 hours to come to the region of Active Pass and Point Roberts after the waves started to travel into the strait, due to the much lower tidal speed predictions of the following flood (Figure 5.5). The source of the left-hand-side wave front observed on June 26 is not clear.

The internal waves do not start to propagate into the Strait of Georgia right after the tide turned to flood. Instead, there is a time delay (Figure 5.14). From Baschek (2002), according to the ADCP measurements in September of 2000, within the first 1.5 – 2 hours after the ebb turned to flood, the flow in the Strait of Georgia next to the sill was mainly parallel to the sill and in the eastward direction. The flood flow increased and the currents were directed from Boundary Pass into the Strait of Georgia 2 – 4 hours after the ebb tide. The currents were then strong enough to flow over the sill and enter the strait. This agrees with our results that the internal waves we modeled did not start to travel into the Strait

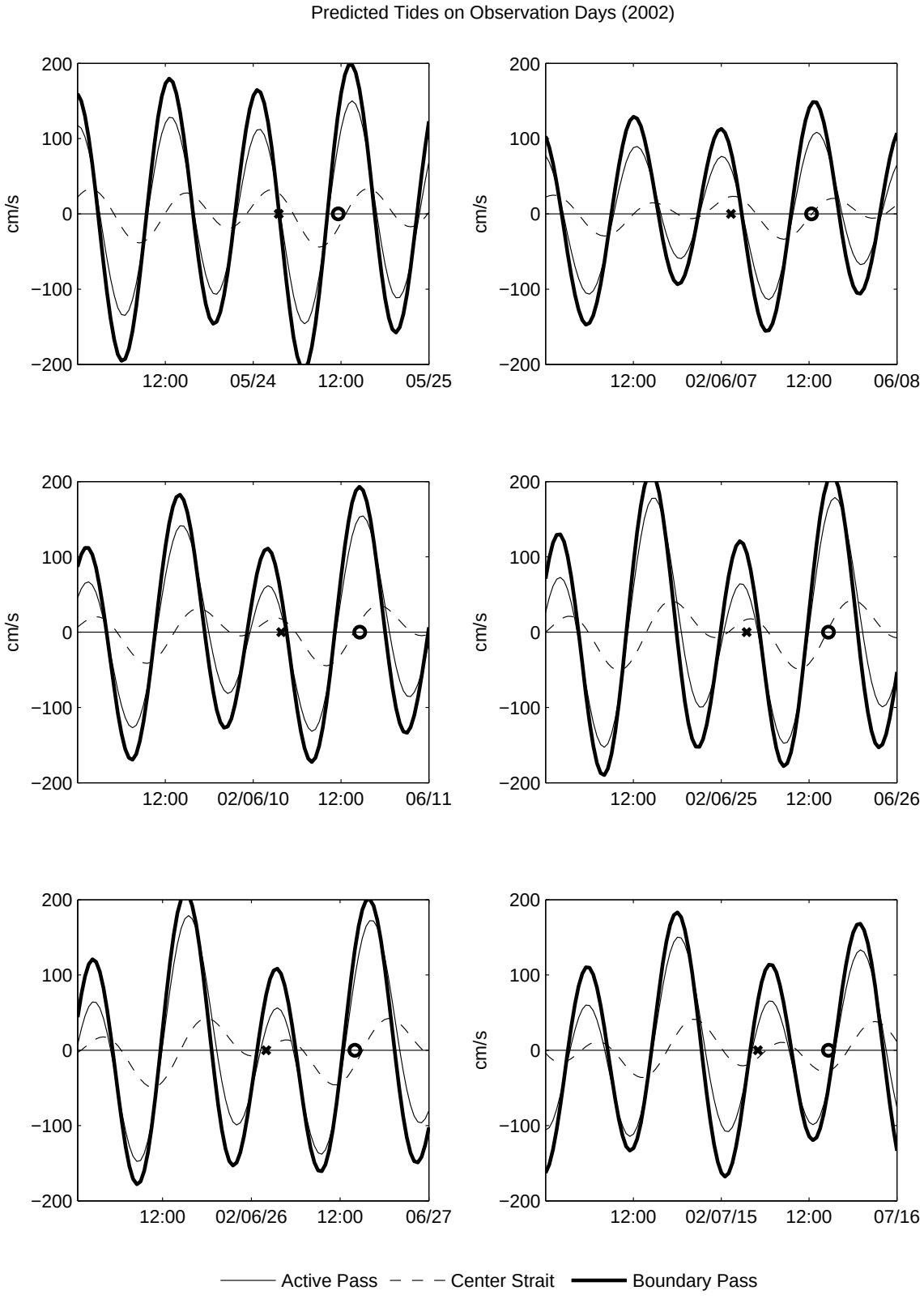

Figure 5.14: Tides on observation days with the times ("x") that the generated waves at Boundary Pass started to travel into the Strait of Georgia and the times ("o") that they are observed between Active Pass and Point Roberts marked out.

of Georgia right after the tide turned to flood, but with a time delay. Since the waves come out of Boundary Pass well into the flood they are not the "upstream waves" that are released into the Strait when the ebb tide relaxes. It is most possible that an internal lee wave or a hydraulic jump forms downstream of the sill during the ebb tide and is trapped there until the tidal flow reversed direction. A train of internal waves then evolved and propagated into the Strait of Georgia. This is similar to the findings of La Violette and Arnone (1980) in the Strait of Gibraltar.

A factor not considered, but potentially important, is the variation of wave phase speeds during propagation. For example, wave phase speeds could have decreased as dissipation reduced amplitudes. Variations in stratification and in shear could also cause changes in phase speeds. However, it seems unlikely that such variations would be large enough to change our basic conclusions.

The techniques used in this chapter are relatively crude. Although the generation time estimates are reasonably reliable, the actual shape of the predicted wave fronts does not match the observations very well. However, better predictions would require a more accurate representation of the near-surface velocity field. Creating such a model would be a significant endeavor, and without more observations would be difficult to validate.

Chapter 6

Discussion and Conclusion

Internal waves are common, important, but not completely-understood components of stratified systems, especially when wave amplitudes are large and nonlinearities are significant. Weakly nonlinear internal waves are often described by classic model equations. Most laboratory or field research survey in the literature matches observations against the shallow-water KdV equation, even when their waves are strictly out of the scope of the KdV equation because they are in deep water (Osborne and Burch 1980; Koop and Butler 1981; Michallet and Barthelemey 1998) or large-amplitude (Small et al., 1999). The deep-water BO equation has not found application in natural systems. More complex behaviors that occur when nonlinear waves cross at an angle are even less well-understood. Previous work is generally analytical or numerical. There is almost no quantitative analysis of oblique wave-wave interactions in field observations that can be compared with existing theories or numerical results.

To obtain geophysical data, a novel observational method was applied in the Strait of Georgia. This allowed us to study internal waves by comparing with classic model propagation equations and wave interaction theories. Our data also enabled us to investigate wave generation. To some extent the crudeness of previous comparisons has been due to the lack of high-quality data capable of separating effects that are relatively small, or indeed (in the case of wave-wave interactions) due to the lack of data of any kind. The photographic

time-lapse technique developed here has the potential to remedy this lack, but many issues arise in actually acquiring useful data. One major achievement of the work described here is to show that this combination of aerial and water column data can produce datasets of high enough quality that some quite subtle effects in wave propagation can be identified in a reasonably economic way. In the existing literature, the majority of internal wave observations are obtained with conventional techniques. Moum et al. (2003) is one of the few in which photo imaging was used, but their aerial data was not rectified, nor was phase propagation important in their analysis.

In the survey area, the upper layer is very thin, about $2 - 4$ m, while the lower layer is deep, over 100 m. The observed internal waves have wave amplitudes comparable to the upper thin layer. Therefore, we know a priori that the observed wave amplitudes are not small and that they are not shallow water waves. In a first step in describing the important physical processes we attempted to model propagation using a variety of analytical models. We fit our data (sixteen case studies) to classic model equations including linear, KdV, BO, eKdV (two-layer only), and strongly nonlinear (two-layer only) equations and found that the continuously stratified BO equation can describe the observed internal waves in the Strait of Georgia. In fact, it was the only model that did so satisfactorily. In addition, the effect of shear was found to be very important. Without shear, none of the above classic model equations could provide convincing predictions for the observed internal wave propagation. Not only is this the first time that waves in a geophysical context have been found to be described by the BO equation, but this occurs when nondimensional amplitudes are $O(1)$. In fact even at this order waves are far from being maximal and so the BO equation may have wider application than has been thought. In the case of two-layer stratification, it is found that a strongly nonlinear equation provides predictions very close

to those using BO equations. Therefore, although our data was not fitted to continuously stratified strongly nonlinear models, which can only be done numerically, it is not expected that such comparisons will provide much better results. However, it is important to note that a two-layer approximation is always unsatisfactory. Details of stratification and shear are thus more important than higher-order nonlinearities in the analysis.

The oblique wave-wave interactions we observed around Point Roberts were first noted in the Strait of Georgia by Tabata (1972), analyzing aerial photos from the 1950s. As in Figure 6.1, during the end of a large ebb on June 1, 1950, near Point Roberts, there were waves propagating to the northwest and to the west with angles close to what we observed in 2002. The end of a large ebb at Point Atkinson coincides with peak flood current at Active Pass (Shand, 1953). It is also during the peak flood at Active Pass that we observed the oblique interactions near Point Roberts in 2002. The coincidence suggests that, for at least fifty years, an oblique interaction phenomena has been repeatedly occurring near Point Roberts during large flood tide at Active Pass. If the hovercraft could (it did not for most of the studied cases) cross the pre- and post-interaction waves and the run-ups (stems), it will allow easier and more accurate study of the interaction and more complete and definite comparisons with previous work. Due to time and resource limitations, we were only able to analyze a few interactions in this thesis. A more complete and decisive picture of the interactions in the Strait would require more case studies. However, this is the first time that the previous analytical and numerical results on wave-wave interactions are tested by actual field data. Future work in wave-wave interaction can therefore profitably focus on this area.

The observed oblique internal wave-wave interactions were investigated. Our preliminary results suggest that the observed properties of interactions vary quantitatively al-

though not qualitatively from Miles' (1977 a, b) results especially for Mach interactions. The larger amplitudes tend to prevent Mach interaction from occurring.

A generation mechanism for internal waves in the Strait of Georgia was proposed based on the cross-strait surveys and the assumption of point or near-point generation. The observed waves were found to be formed at the passes to the south of the Strait (Boundary Pass and North Samuel Island). However, they only propagate into the strait during the following flood tide. They are not released when the ebb tide relaxes. Our observations occurred some 8 – 14 hours after generation. More decisive study of generation mechanism requires information near the passes where waves are thought to be formed, such as Boundary Pass and North Samuel Island. Measurements of currents, wave-structure and vertical density profile, and images of waves will be required at a slightly earlier stage of the tide. As was found out, it took a wave about 8 – 14 hours to propagate to the Active Pass area. The propagation speed of the wave was assumed to remain unchanged during this long propagation, which is not necessarily true. Using an actual time-dependent wave speed could affect the exact "start time", although it is likely that the results will not be qualitatively modified.

Finally, our work has left open an issue involving the background currents. As we have proved background shear currents have an important effect on wave propagation and such shear could affect the curvature of wave fronts as well. However, the effect of shear on wave front curvature was ignored in the wave generation study of Chapter 5. These effects may explain the mismatch between the predicted and the observed wave packet fronts, especially on the east side of the right-hand-side wave packets.

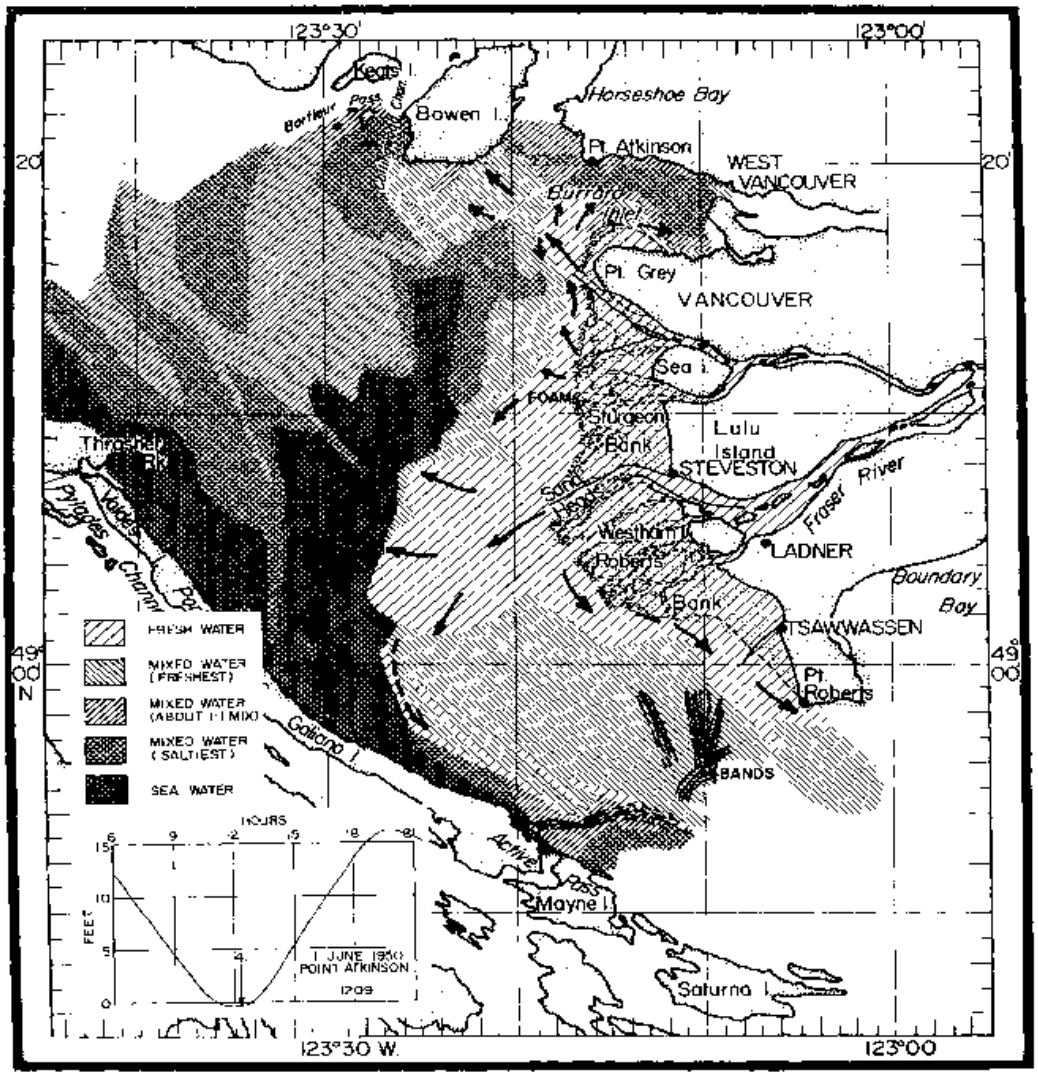

Figure 6.1: Observed internal wave oblique interaction in 1950 based on aerial photography (Tabata, 1972). Distribution of water types in the central Strait of Georgia during end of large ebb (Lower Low Water) on 1 June 1950 as deduced from a series of vertical and oblique aerial photographs. Solid arrows denote interpreted directions of surface currents also but in which there is less certainty with directions than indicated by solid arrows. Bands denote alternate bands of ruffled and smooth water surface indicating the presence of internal waves (lines represent crest of waves).

Bibliography

[1] Apel, J. R., H. M. Byrne, J. R. Proni, and R. L. Charnell, 1975: Observations of oceanic internal and surface waves from the Earth Resources Technology Satellite. J. Geophys. Res., 80, 865-881.

[2] Apel, J. R., Ostrovsky, L. A., and Stepanyants, Yu. A., 1995: Internal solitons in the ocean. Report MERCJRA0695, Applied Phys. Lab., The John Hopkins University.

[3] Artale, V., Levi, D., Salusti, E. and Zirilli, F., 1984: On the generation of internal solitary marine waves. Il Nuovo Cimento C, Volume 7, Number 3, 365-377.

[4] Baines, P. G., 1973: The generation of internal tides by flat-bump topography. Deep Sea Res. 20, 179-205.

[5] Baines, P. G., 1974: The generation of internal tides over steep continental slopes. Philos. Trans. R. Soc. London A 277, 27-58.

[6] Baines, P. G., 1982: On internal tide generation models. Deep Sea Res. 29, 307-338.

[7] Baines, P. G., 1995: Topographic effects in stratified flows. Cambridge Monographs on Mechanics, Cambridge University Press.

[8] Baines, P. G., 2007: Internal tide generation by seamounts. Deep Sea Research Part I: Oceanographic Research Papers. Vol. 54, Iss. 9, 1486-1508.

[9] Baschek, B., 2002: Air-Sea Gas Exchange in Tidal Fronts. Ph.D. Thesis. University of Victoria.

[10] Benjamin, T.B., 1966: Internal waves of finite amplitude and permanent form. J. Fluid Mech. 25, 241-270.

[11] Benney, D.J., 1966: Long non-linear waves in fluid flows. J. Math. Phys., 45, 52-63.

[12] Benney, D.J. and D. R. S. Ko, 1978: The propagation of long large amplitude internal waves. Study. Appl. Math., 59, 187-199.

[13] Boegman, L., Ivey, G., and Imberger, J., 2005: The degeneration of internal waves in lakes with sloping topography. Limnology and Oceanography, 50, 1620-1637.

[14] Bourgault, D., 2007: Shore-based photogrammetry of river ice. Can. J. Civ. Eng., 35(1): 80-86.

[15] Camassa, R., Choi, W., Michallet, H., Rusas, P.-O. and Sveen, J. K., 2006: On the realm of validity of strongly nonlinear asymptotic approximations for internal waves, J. Fluid Mech., 549, 1-23.

[16] Chereskin, T. K., 1983: Generation of internal waves in Massachusetts Bay. J. Geophys. Res., 88, C4, 2649-2661.

[17] Choi, W. and Camassa, R., 1999: Fully nonlinear internal waves in two-fluid system. J. Fluid Mech., 396, 1-36.

[18] Choi, W., 2006: The effect of a background shear current on large amplitude internal solitary waves. Phys. of Fluids, 18, 1-7.

[19] Colosi, J. A., Beardsley, R. C., Lynch, J. F., Gawarkiewicz, G., Chiu, C. S., and Scotti, A., 2001: Observations of nonlinear internal waves on the outer New England continental shelf during the summer Shelf break Primer study. J. Geophys. Res., Vol. 106, No. C5, 9587-9601.

[20] Cox, C. S. and Sandstrom, H., 1962: Coupling of internal and surface waves in water of variable depth. Journal of Oceanogr. Soc. Japan., 20th anniv. vol., 499-513.

[21] Christie, D. and White, R. 1995: The Morning Glory of the Gulf of Carpentaria. AOPA (Aircraft Owners and Pilots Association of Australia).

[22] Cummins, P., Vagle, S., Armi, L., and Farmer, D., 2003: Stratified flow over topography: upstream influence and generation of nonlinear internal waves. Proc. R. Soc. Lond. A, 459, 1467-1487.

[23] Davis, R. E., and A. Acrivos, 1967: Solitary internal waves in deep water. J. Fluid Mech., 29, 593-607.

[24] Davies, A. and Xing, J., 2006: Modeling tidal mixing in sill regions. Geophys. Res. Abstracts, Vol. 8, 01383, 2006.

[25] Dewey, R., Richmond, D., and Garrett, C., 2005: Stratified tidal flow over a bump. Journal of Physical Oceanography, 35, 1911-1927.

[26] Drazin, P. G. and R. S. Johnson, 1988: Solitons: an introduction. Cambridge, England: Cambridge University Press.

[27] Dushaw, B. D., B. D. Cornuelle, P. F. Worcester, B. M. Howe, and D. S. Luther, 1995: Barotropic and baroclinic tides in the central North Pacific Ocean determined from long-range reciprocal acoustic transmissions. J. Phys. Oceanogr., 25, 631-647.

[28] Ewing, G., 1950: Slicks, surface films, and internal waves, J. Mar. Res., 9, 161-187.

[29] Farmer, D. M. and Armi, L., 1999: The role of small-scale entrainment and mixing in flow establishment. Proceedings of the Royal Society of London, A, 455, 3221-3258.

[30] Farmer, D. M. and Smith, J. D., 1980: Tidal interaction of stratified flow over the sill in Knight Inlet. Deep Sea Res. I, 27, 239-254.

[31] Foreman, M. G. G., Walters, R. A., Henry, R. F., Keller, C. P., and Dolling, A. G. 1995: A tidal model for eastern Juan de Fuca Strait and the southern Strait of Georgia, J. Geophys. Res. Vol. 100 , No. C1 , p. 721-740.

[32] Funakoshi, M., 1980: Reflection of obliquely incident solitary waves. J. Phys. Soc. Japan 49, 2371-2379.

[33] Funakoshi, M., 1981: On the time evolution of a solitary wave reflected by an oblique wall. Rep. Res. Inst. Appl. Mech. Kyushu Univ. 29, 79-93.

[34] Gan, J., and Ingram, R. G., 1992: Internal hydraulics, solitons and associated mixing in a stratified Sound. J. Geophys. Res. 97, 9669-9688.

[35] Gargett, A. E., and B. A. Hughes, 1972: On the interaction of surface waves and internal waves, J. Fluid Mech., 52, 170-191.

[36] Gargett, A. E., 1976: Generation of internal waves in the Strait of Georgia, British Columbia. Deep Sea Res., 23, 17-32.

[37] Green, A. E. and Naghdi, P. M., 1977: Water waves in a nonhomogeneous incompressible fluid, J. Applied Mech., December, 523-528.

[38] Grimshaw, R., 1997, Internal solitary waves. Advances in coastal and Ocean Engineering, ed. P.L.-F. Liu, World Scientific Publishing Company, Singapore, 3, 1-30.

[39] Grimshaw, R., E. Pelinovsky, and T. Talipova, 1997: The modified Korteweg-de Vries equation in the theory of large-amplitude internal waves. Nonlin. Proc. Geophys., 4, 237-250.

[40] Grimshaw, R., 1998: Internal Solitary Waves in Shallow Seas and Lakes, Phys. Proces. in Lakes and Oceans, Coastal and Estuar. Stud., 54, 227-240.

[41] Grimshaw, R. (2002). Internal solitary waves. Proceedings of the International Conference dedicated to the 100th anniversary of A.A. Andronov; Progress in Nonlinear Science, Volume II, Frontiers of Nonlinear Physics, ed. A.G. Litvak, Inst. Applied Physics, Nizhny Novgorod, 139-153.

[42] Grimshaw, R. and Zhu, Y., 1994: Oblique interactions between internal solitary waves. Stud. Appl. Math. 92, 249-270.

[43] Grue, J., Jensen, A, Rusas, P., Sveen J., 1999: Properties of large-amplitude internal waves. J. Fluid Mech., 380, 257-278.

[44] Halpern, D., 1971: Observation on short period internal waves in Massachusetts Bay, J. Mar. Res., 29, 116-132.

[45] Haury, L. R., Briscoe, M. G., and Orr, M. H., 1979: Tidally generated internal wave packets in Massachusetts Bay, Nature, 278, 312-317.

[46] Helfrich, K. and Melville, W., 2006: Long nonlinear internal waves. Ann. Rev. Fluid Mech., 38, 395-425.

[47] Hibiya, T., 1986: Generation mechanism of internal waves by tidal flow over a sill. J. Geophys. Res., 91, C6, 7697-7708.

[48] Hibiya, T., 1990: Generation mechanism of internal waves by a vertically sheared tidal flow over a sill. J. Geophys. Res., 95, C2, 1757-1764.

[49] Hibiya, T., 2004: Internal wave generation by tidal flow over a continental shelf slope, J. Oceano., 60, 2, 637-643.

[50] Holland, K., Holman, R., Lippmann, T., Stanley, J. and Plant, N., 1997: Practical use of video imagery in nearshore oceanographic field studies. IEEE J. Oceanic. Eng., 22(1), 81-92.

[51] Holloway, P., Pelinovsky, E., Talipova, T.,and Barnes, B., 1997: A Nonlinear Model of Internal Tide Transformation on the Australian North West Shelf, Journal of Physical Oceanography, Vol. 27.

[52] Hughes, B. A. and T. W. Dawson, 1988: Joint Canada-U. S. ocean wave investigation project: an overview of the Georgia Strait Experiment. J. Geophys. Res., 93, 12219-12380.

[53] Hughes, B. A. and R. F. Gasparovic (Eds.), 1988: Georgia Strait and SAR internal wave signature experiments. J. Geophys. Res., 93, 12217-12380.

[54] Hughes, B. A. and J. F. R. Gower, 1983: SAR imagery and surface truth comparisons of internal waves in Georgia Strait, British Columbia. J. Geophys. Res., 88 (C3), 1809-1824.

[55] Johnson, R. S., 1982: On the oblique interaction of a large and a small solitary wave. J. Fluid Mech. 120, 49-70.

[56] Joseph, R. J., 1977: Solitary waves in finite depth fluid. J. Phys. A: Math. Gen. 10 (No. 12), L225-L227.

[57] Kao, T. W., Pan, F. S., and Renourd, D., 1985: Internal solitons on the pycnocline: generation, propagation, and shoaling on breaking over a slope. J. Fluid Mech. 159, 19-53.

[58] King, D.B, Cheng-Bin, S.A., and McGirr, R.W., 1994: Effect of shallow water internal waves on broadband acoustic wave propagation," in Environmental Acoustics: International Conference on Theoretical & Computational Acoustics Vol. II, edited by D. Lee and M. Shultz (World Scientific Press, Singapore) 793-808.

[59] Klymak, J. M. and Gregg, M. C., 2001: Three-dimensional nature of flow near a sill. J. Geophys. Res., 106, 22295-22311.

[60] Klymak, J. M. and Gregg, M. C., 2004: Tidally generated turbulence over the Knight Inlet Sill. Journal of Physical Oceanography, 34, 1135-1151.

[61] Koop, C. G., and G. Butler, 1981: An investigation of internal solitary waves in a two-fluid system. J. Fluid Mech., 112, 225-251.

[62] Kubota, T., Ko, D.R.S., Dobbs, L.D., 1978: Weakly-nonlinear, long internal gravity waves in stratified fluids of finite depth. J. Hydronautics 12, 157.

[63] Lacomb, H. and Richez, C., 1982: The regime of the Strait of Gibraltar. Hydrodynamics of Semi-enclosed Seas, 13-73, Elsvier.

[64] Lamb, K. G., and L. Yan, 1996: The evolution of internal wave undular bores: Comparison of a fully nonlinear numerical model with weakly nonlinear theory. J. Phys. Oceanogr., 26, 2712-2734.

[65] La Violette, P. E., and R. A. Arnone, 1988: A tide-generated internal waveform in the western approaches to the Strait of Gibraltar, J. Geophys. Res., 93, 15653-15667.

[66] LeBlond, P. H. and Mysak, L. A., 1978: Waves in the ocean. Elsevier. 602pp.

[67] Lee C. and Beardsley R., 1974: The generation of long nonlinear internal waves in a weakly stratified shear flow. J. Geophys. Res., 79, 453-62.

[68] Leichter, J. J, G. Shellengarger, S.J. Genovese et al. 1998: Breaking internal waves on a Florida (USA) coral reef: a plankton pump at work? Mar. Ecol. Prog. Ser. 166, 83-97.

[69] Liu, A. K. and Chang, Y. S., Hsu, M-K, Liang, N. K. 1998: Evolution of nonlinear internal waves in the East and South China Seas. J. Geophys. Res., Vol. 103, No. C4, 7995-8008.

[70] Liu, A. K. and Hsu, M-K, 1998: Nonlinear internal wave interaction in the China seas. The 1998 WHOI/IOS/ONR internal solitary wave workshop: contributed papers. Technical report.

[71] Long, R. R., 1953: Some aspects of the flow of stratified fluids. I. A theoretical investigation. Tellus, 5, 42-58.

[72] Lynett, P. and P. L.-F. Liu, 1998: Numerical modeling of internal wave-wave interactions. The 1998 WHOI/IOS/ONR internal solitary wave workshop: contributed papers. Technical report.

[73] Marmorino, G. O., 1987: Observations of small-scale mixing processes in the seasonal thermocline, Part II: wave breaking. J. Phys. Oceanog., Vol. 17, No. 9, 1348-1355.

[74] Maslowe, S. and Redekopp, L., 1980: Long nonlinear waves in stratified shear flows. J. Fluid Mech., 101, part 2, 321-348.

[75] Matsuno, Y., 1998: Oblique interaction of interfacial solitary waves in a two-layer deep fluid. Proc. R. Soc. Lond. A. 454, 835-856.

[76] Maxworthy, T., 1979: A note on the internal solitary waves produced by tidal flow over a three-dimensional ridge. J. Geophys. res., 84, 338-346.

[77] McPhee-Shaw, E., 2006: Boundary-interior exchange: Reviewing the idea that internal wave mixing enhances lateral dispersal near continental margins. Deep-Sea Research II, 53, 42-59.

[78] Melville, W. K., 1980: On the Mach reflexion of a solitary wave. J. Fluid Mech. 98, 285-297.

[79] Michallet, H. and Barthelemy, E., 1998: Experimental study of interfacial solitary waves, J. Fluid Mech. 366, 159-177.

[80] Miles, J. W., 1977a: Obliquely interacting solitary waves, J. Fluid Mech. 79, 157-169.

[81] Miles, J. W., 1977b: Resonantly interacting solitary waves, J. Fluid Mech. 79, 171-179.

[82] Miles, J. W., 1979: On internal solitary waves. Tellus, 31, 456-462.

[83] Miles, J. W., 1981: On internal solitary waves II. Tellus, 33, 397-401.

[84] Moum, J. N., Farmer, D. M., Smyth, W. D., Armi, K., and Vagle, S., 2003: Structure and generation of turbulence at interfaces by internal solitary waves propagating shoreward over the continental shelf. Journal of Physical Oceanography, 33, 2093-2112.

[85] Munk, W., and C. Wunsch, 1998: Abyssal recipes II: Energetics of tidal and wind mixing. Deep-Sea Res., 45, 1977-2010.

[86] Oikawa, M., 1984: On the weak interactions of the Benjamin-Ono solitons. Bull. Res. Inst. Appl. Mech. Kyushu Univ. 60, 467-472.

[87] Ono, H., 1975: Algebraic solitary waves in stratified fluids, J. Phys. Soc. Japan. 39, 1082-1091.

[88] Osborne, A. R., and T. L. Burch, 1980: Internal solitons in the Andaman Sea. Science, 208, 451-460.

[89] Ostrovsky, L. A. and Stepanyants, A., 1989: Do internal solitons exist in the ocean? Reviews of Geophysics, 27, 293-310.

[90] Ostrovsky, L. A. and Stepanyants, A., 2005: Internal solitons in laboratary experiments: comparison with theoretical models. Chaos, 15, 037111, 1-28.

[91] Pawlowicz, R., 2003: Quantitative Visualization of Geophysical Flows using Low-Cost Oblique Digital Time-Lapse Imaging. IEEE J. Oceanic Eng. 28 (4), 699-710.

[92] Pawlowicz, R., O. Riche, and M. Halverson, 2007: The circulation and residence time of the Strait of Georgia using a simple mixing-box approach, Atmosphere-Ocean 45 (2), 173-193.

[93] Pineda, J. 1991. Predictable upwelling and the shoreward transport of planktonic larvae by internal tidal bores. Science. 253, 548-551.

[94] Pinkel, R., 1983: Doppler sonar observations of internal waves, wave-field structure. J. Phys. Oceano., Vol. 13, Iss. 5, 804-815.

[95] Pinkel, R., J. T. Sherman, J. A. Smith, and S. Anderson, 1991: Strain: Observations of the vertical gradient of isopycnal vertical displacement. J. Phys. Oceanogr., 21, 527-540.

[96] Prinsenberg, S. J., and Rattray Jr., M. R., 1975: Effects of continental slope and variable Brunt-Vaisala frequency on the coastal generation of internal tides, Deep Sea Res., 22, 251-263, 1975.

[97] Prinsenberg, S. J., W. L. Wilmot and M. Rattray, Jr., 1974: Generation and dissipation of coastal internal tides. Deep-Sea Res., 21, 263-281.

[98] Rattray, M. Jr., 1960: On the coastal generation of internal tides, Tellus, 12, 54-62.

[99] Rattray, M. Jr., Dworski, J. G., and Kovala, P. E., 1969: Generation of long internal waves at a continental slope, Deep Sea Res., 16, suppl., 179-195.

[100] Sandstrom, H., J.A. Elliott, 1984: Internal tide and solitons on the Scotian Shelf: A nutrient pump at work, J. Geophys. Res., 89, 6415-6426.

[101] Sandstrom, H., J.A. Elliott and N.A. Cochrane, 1989: Observing groups of solitary internal waves and turbulence with BATFISH and echo-sounder, J. Phys. Oceanogr., 19, 987-997.

[102] Segur, H. and Hammack, J. L., 1982: Soliton models of long internal waves. J. Fluid Mech., 118, 285-304.

[103] Shand, J. A., 1953: Internal waves in Georgia Strait, Trans. AGU, V. 34(6).

[104] Small, J., Hornby, B., and Scott, J., 1998: Internal solitons in the ocean: predictions from SAR, http://www.whoi.edu/science/AOPE/people/tduda/isww/text/small/jsmall.htm.

[105] Small, J., Hallock, Z., Pavey, G., and Scott, J., 1999: Observations of large amplitude internal waves at the Malin shelf-edge during SESAME 1995, Cont. Shelf Res. 19, 1389-1436.

[106] Soomere, T. and Engelbrecht, J., 2006: Weakly two-dimensional interaction of solitons in shallow water. Euro. J. Mech. B/Fluids, 25, 636-648.

[107] Soomere, T., 2007: Nonlinear components of ship wake waves. Appl. Mech. Rev., 60(3), 120-138.

[108] Stastna, M. and Lamb, K., 2002: Large fully nonlinear internal solitary waves: The effect of background currents, Physics of Fluids. 14(9), 2987-2999.

[109] Staschuk, N. and Vlasenko V., 2007: Numerical modeling of stratified tidal flow over a fjord sill. Ocean Dynamics, Vol. 57, Numbers 4-5.

[110] Stigebrandt, A., 1980: Some aspects of tidal interaction with fjord constrictions. Estuarine Coastal Mar. Sci., 11, 151-166.

[111] Tabata, S., 1972: The movement of Fraser river-influenced surface water in the Strait of Georgia as deduced from a series of aerial photographs, Pacific Marine Sci. Report NO. 72-6. Victoria, B. C.: the Branch.

[112] Tanaka, M., 1993: Mach reflection of a large-amplitude solitary wave, J. Fluid Mech., 248, 637-661.

[113] The SWARM Group, 1997: An overview of the 1995 SWARM shallow water internal wave acoustic scattering experiment, IEEE J. Oceanic ENG., 22(3), 465-500 .

[114] Tsuji, H. and Oikawa, M., 2001: Oblique interaction of internal solitary waves in a two-layer fluid of infinite depth. Fluid Dyn. Res. 29, 251-267.

[115] Tung, K., Ko, D., and Chang, J., 1981: Weakly nonlinear internal waves in shear, Stud. in Appl. Math., 65, 189-221.

[116] Turner, J. S., 1973: Buoyancy effects in fluids. Cambridge University Press.

[117] Umlauf, L. and Lemmin, U., 2005: Interbasin exchange and mixing in the hypolimnion of a large lake: the role of long internal waves. Limnology and Oceanography, 50, 1601-1611.

[118] Van Haren, H., 2005: Details of stratification in a sloping bottom boundary layr of Great Meteor Seamount. Geophys. Res. Lett., 32, doi:10.1029/2004GL022298.

[119] Vlasenko, V., Brandt, P., and Rubino, A., 2000: Structure of large-amplitude internal solitary waves. J. Phys. Oceanog., 30, 2171-2185.

[120] Whitham, G. B., 1974: Linear and nonlinear waves. John Wiley & Sons, New York.

[121] Wijffels, S. and Meyers, G., 2004: An intersection of oceanic waveguides:variability in the Indonesian throughflow region. J. Phys. Oceanog., 34, 1232-1253.

[122] Xing, J. and Davies, A., 2006: Processes influencing tidal mixing in the region of sills. Geophys. Res. Lett., 33, L04603.

[123] Ziegenbein, J. 1969: Short internal waves in the Strait of Gibraltar. Deep Sea Res., 16, 479-487.